Clemson University
TigerPrints

All Dissertations | Dissertations

12-2015

INTEGRATED COHERENT COMBINING OF ANGLED-GRATING BROAD-AREA LASERS: DESIGN, FABRICATION AND CHARACTERIZATION

Yunsong Zhao
Clemson University, yunsonz@g.clemson.edu

Follow this and additional works at: https://tigerprints.clemson.edu/all_dissertations

Part of the Electrical and Computer Engineering Commons

Recommended Citation
Zhao, Yunsong, "INTEGRATED COHERENT COMBINING OF ANGLED-GRATING BROAD-AREA LASERS: DESIGN, FABRICATION AND CHARACTERIZATION" (2015). *All Dissertations*. 1586.
https://tigerprints.clemson.edu/all_dissertations/1586

This Dissertation is brought to you for free and open access by the Dissertations at TigerPrints. It has been accepted for inclusion in All Dissertations by an authorized administrator of TigerPrints. For more information, please contact kokeefe@clemson.edu.

INTEGRATED COHERENT COMBINING OF ANGLED-GRATING BROAD-AREA LASERS: DESIGN, FABRICATION AND CHARACTERIZATION

A Dissertation
Presented to
the Graduate School of
Clemson University

In Partial Fulfillment
of the Requirements for the Degree
Doctor of Philosophy
Electrical and Computer Engineering

---

by
Yunsong Zhao
December 2015

Accepted by:
Dr. Lin Zhu, Committee Chair
Dr. John Ballato
Dr. Liang Dong
Dr. Pingshan Wang

ABSTRACT

In this thesis, we proposed, fabricated and demonstrated the coherent beam combining of angled-grating broad-area lasers. We have obtained the simultaneous coherent beam combining and single transverse mode operation completely on chip without any external phase control/components. Since the single transverse mode is the key to obtain diffraction-limit beam quality and high brightness, the proposed design is a good candidate for high power and high brightness applications. In the proposed coherently combined laser array, we use the angled-grating broad-area laser as the building block and overlap the adjacent emitters at one facet. The overlapped region becomes a 2D coupling region. And the coherent beam combining is obtained through the Bragg diffraction in these coupling regions.

The scalability of the proposed structure is also studied through a simplified zigzag array with the same topographic structure. The random phase difference among emitters in the array is assumed to be Gaussian distribution. And the brightness of the laser array is calculated at different random phase strength in two extreme situations: one is that only adjacent emitters are correlated and the other one is that all the emitters in the array are correlated. In the real zigzag laser array, the power of one emitter can be coupled into multiple neighbouring emitters. The scalability of the proposed structure should be between the two extreme situations. It should be similar to the performance of common cavity laser arrays.

The fabricated two coherently combined angled-grating broad-area lasers shows an in-

terference pattern in the far field measurement indicating the two emitters are indeed coherently combined. However, the overall envelope shows double lobes. A further investigation reveals that the double lobes come from the uneven distribution of the injected current due to the lateral current leakage. The uneven current distribution excites the second order Bragg modes resulting in the double lobes in the far field. Therefore, we use ion implantation to increase the resistance outside the metal contact area to obtain a more uniform current distribution. And the laser diodes after ion implantation show a single lobe in the far field envelope with interference patterns within the envelope. The output power of the fabricated lasers is limited by the bad thermal management. There are obvious thermal rollover in the LI curves at high current level. By p-side-down bonding, we bring the active region closer to the heat sink to help with the heat dissipation. Both the single and two combined angled-grating broad-area lasers can deliver over $1W$ output power without obvious thermal rollover at $180K$. They can also lase in room temperature pumped with quasi-CW current source. However the slope efficiency is still low and the threshold is relatively high, which may be due to the high optical and electrical loss induced by the deep III-V dry etching.

In order to reduce the etched area for lower optical and electrical loss, we decide to substitute the TBR grating with 2D triangle lattice photonic crystal cavity. There are two advantageous of 2D PC cavity, one is to reduce the surface defect states for less total loss, the other one is to control the longitudinal mode to obtain single wavelength as well as single transverse mode, since structure along the propagation direction is also periodic. The reason for choosing triangle lattice is to easily combine the 2D PC Bragg cavity in the same way we did in the coherent combining of angled-grating broad-area lasers. We solve for the first several photonic bands using MPB and determine the periods along the transverse and propagation directions for design purpose. Since these two periods are geometrically related too, we find discrete tilted angles to satisfied both resonant and geometric

requirements. And usually the wavevector along the propagation direction is resonant with a high order grating vector. We fabricated both single and two combined PC Bragg lasers. As expected, the single 2D PC Bragg laser diode presents stable single wavelength optical spectrum without mode hopping during the measurement period. The far field also indicates near diffraction-limited beam quality. However, the combined laser diode shows multiple peaks in the far field profile due to the shallow etching depth.

Regrowth wafer is another way to reduce the total loss. In this project, since the grating is wet etched in the cladding layer which is much closer to the quantum well, the grating depth can be pretty shallow. Since we don't have any epitaxy layer growth facilities and experience, the epitaxy layer growth and regrowth process is done by a foundry service. After the quantum well is grown, the wafer is shipped to us and after the grating is etched, we ship them back to the service for regrowth process. Unfortunately, due to the surface cleanness, the wafer after regrowth has a lot of defects in it. All the devices including the broad-area lasers do not lase. Therefore, we couldn't evaluate the performance of the coherently combined lasers using regrowth epitaxy wafer.

We also investigate another interesting laser cavity design based on the angled-grating broad-area laser, which is the folded angled-grating broad-area laser. By using the symmetry of the snake-like lasing mode in the angled-grating broad-area laser, the angled-grating broad-area laser can be folded at the center to the other direction without disturbing the lasing mode. The experiment results confirm that with a well design cavity length, the folded cavity has a similar performance to that of the angled-grating broad-area laser. The immediate benefit of this design is to reduce the laser area and increase the yield. More promising is to combine two folded cavity laser to increase the filling factor. It is obvious that in the previous combined laser design, the longer the cavity is, the smaller the filling factor is. By combining two folded cavity lasers, it is possible to increase the filling factor to nearly 1. The fabricated two combined folded cavity lasers show an increased angular

distance between two interference fringes in the far field. However, due to the relative low output power, the aperture distance is still larger than designed distance.

DEDICATION

To:

My parents and wife!

ACKNOWLEDGMENTS

First and foremost, I am greatly indebted to Dr. Lin Zhu, my advisor for taking me on as a graduate student and for providing such a tremendous amount of support, advice and encouragement during my study in this group.

I would like to thank Professor John Ballato, Professor Liang Dong and Professor Ping-shan Wang for being my committee member and for providing advices on my dissertation proposal.

I also would like to thank all my colleagues for all their effort to help me through this entire project. Dr. Chenguang Huang is very skillful in device fabrication. His suggestions saved me a lot of time when I developed my own process at early stage. Mr. Jiahua Fan helps a lot on the semiconductor laser simulation and provides expertise for the epitaxy wafer design in this dissertation. Mr. Ruoyu Zhang contributes much to the measurement system development. Mr. Yeyu Zhu helps a lot with device fabrication and characterization. Without their help, the whole thing would become much tougher.

Thank you also to the staff members in Gatech Institute for Electronics and Nanotechnology for their help on the facilities training and for their invaluable experience on device fabrication. Special thanks to Dr. Devin Brown for his tremendous help and vast knowledge on Ebeam lithography system, to Dr. Mikkel Thomas for his advice on the whole fabrication process.

At last, I am very grateful to my parents and my wife for their endless and unconditional

love and support. Thank you for always believing in me.

TABLE OF CONTENTS

Page

TITLE PAGE . . . . **i**

ABSTRACT . . . . **ii**

DEDICATION . . . . **vi**

ACKNOWLEDGMENTS . . . . **vii**

1 INTRODUCTION **1**
1.1 Angled-grating Broad-area Lasers 3
1.1.1 TBR grating 4
1.1.2 Tilted cavity design 10
1.2 Coherent Beam Combining 13

2 DESIGN OF COHERENTLY COMBINED ANGLED-GRATING BORAD-AREA LASERS **17**
2.1 Simultaneous single mode control and coherent beam combining through Bragg diffraction 18
2.2 Modal and Scalability Analysis of a Zigzag Structure for Passive Coherent Beam Combining 21
2.2.1 Modal analysis 23
2.2.2 Scalability analysis 27
2.3 Grating design 32
2.3.1 Surface ethced gratings 32
2.3.2 Regrowth gratings 34

3 FABRICATION OF COHERENTLY COMBINED ANGLED-GRATING BROAD-AREA LASERS **37**
3.1 Surface Etched Gratings 38
3.1.1 Deposition of SiO_2 hard mask layer 38
3.1.2 Ebeam Lithography 39
3.1.3 SiO_2 Dry Etch 42
3.1.4 III-V Dry Etch 43

Table of Contents (Continued) **Page**

3.1.5 BCB Etch Back 44
3.1.6 P-Contact Deposition 46
3.1.7 Ion Implantation 47
3.1.8 Lapping 48
3.1.9 N-Contact Deposition 49
3.1.10 Packaging 49
3.2 Regrowth Gratings 50
3.2.1 Deposition of SiO_2 mask layer 51
3.2.2 Ebeam lithography 51
3.2.3 SiO_2 dry etch 53
3.2.4 GaAs wet etch 53
3.2.5 P-contact deposition 54
3.2.6 Ion Implantation 54
3.2.7 N-Contact Deposition 55

4 CHARACTERIZATION OF COHERENTLY COMBINED ANGLED-GRATING BROAD-AREA LASERS 56
4.1 Measurement setup 57
4.1.1 L-I curve 58
4.1.2 Near Field 59
4.1.3 Far Field 59
4.1.4 Optical Spectrum 61
4.2 Results of two coherently combined angled-grating broad-area lasers 61
4.2.1 L-I curve and optical spectrum 61
4.2.2 Near field and far field 62
4.2.3 Improve Beam Quality by Ion Implantation 65
4.2.4 P-side down bonding 71
4.3 Results of six coherently combined angled-grating broad-area lasers 72
4.3.1 Small modal angle modes in the combined mini bar 76
4.4 Results of regrowth angled-grating broad-area lasers 80

5 PHOTONIC CRYSTAL BRAGG LASER WITH TRIANGULAR LATTICE 81
5.1 Introduction 81
5.2 Design 82
5.2.1 Coupled mode theory in 2D photonic grating 85
5.3 Measurement Results 90

6 FOLDED STRUCTURE OF ANGLED-GRATING BROAD-AREA LASERS 93
6.1 Introduction 93
6.2 Laser design 95
6.3 Measurement results and discussion 97

Table of Contents (Continued) Page

6.4 Coherent beam combining of two folded angled-grating broad-area lasers . 100

7 CONCLUSION 103

BIBLIOGRAPHY 104

LIST OF TABLES

Table **Page**

2.1 $In_{1-x}Ga_xAs_yP_{1-y}$/InP epitaxy wafer design 33
2.2 InGaAs/GaAs epitaxy wafer design 35

3.1 PECVD oxide recipe in STS PECVD 2 39
3.2 Ebeam resist spinning recipe 39
3.3 ZEP 520A developing recipe 41
3.4 SiO_2 dry etch recipe in Plasma Thermal ICP 42
3.5 III-V(InP/GaAs) dry etch recipe in STS SOE 43
3.6 BCB spin coating recipe 44
3.7 BCB temperature profile for cure 45
3.8 BCB etch back recipe in Plasma Thermal ICP 46
3.9 Ion implantation recipe for InP wafer 48
3.10 GaAs wet etching recipe 54
3.11 Ion implantation recipe for GaAs wafer 55

LIST OF FIGURES

Figure **Page**

1.1 Schematic plot of a conventional broad-area laser and the beam profile at near and far field. Slow axis(x axis) has a small divergence angle and fast axis(y axis) has a large divergence angle. 2
1.2 Schematic plot of the angled-grating broad-area laser. The laser cavity consists of a tilting broad-area TBR grating. 4
1.3 (a) Refractive index profile of a TBR grating; (b) Plot of modal loss with respective to different modal angles; (c) and (d) Electric field profiles of first and second order Bragg modes; (e) FDTD simulation result of the beating pattern of the two first order Bragg modes. 5
1.4 Schematic plot of a TBR cavity. 5
1.5 The coupling relationship between the grating vectors and a_r, a_l, b_r and b_l. . 7
1.6 Schematic plot of the multi layer structure using TMM. 9
1.7 Schematic plot and FDTD simulation results of the Bragg modes in a tilted cavity. 11
1.8 Calulation model (a) and result (b) of the reflection of a tilted facet. 11
1.9 Plot of r_f of different modes with several different grating coupling coefficients. 13
1.10 Schematic plot of the wavelength beam combining with a diffraction grating. 14
1.11 Schematic plot of (a) MOPA array, (b) Talbot array and (c) Self-Fourier array 16

2.1 Schematic of a coherently combined angled-grating laser. (a) L and W are the length and width of a single emitter, respectively. θ is the tilt angle of the grating. (b) The cross-section structure of a single emitter. (c) Planar geometry of the combined angled-grating laser. Two coherently combined emitters (the output from two legs in the coupled structure) constructively interfere in the far field. 18

Figure **Page**

2.2 Wave coupling and cavity modes in the single emitter and coupled emitter. (a) A single angled-grating emitter. R_1 and R_2 are two planewave-like components resonate with the grating. The phase matching condition between k-vectors is shown in the inset. (b) FDTD simulation result of a single angled-grating resonator. The solid arrows represent the R_1 component and the dashed arrows represent the R_2 component. (c) An on-chip combined angled-grating laser. Arrows in blue represent wave components in the left grating, while arrows in red represent wave components in the right grating. The inset shows the coupling between different wavevectors through the grating. (d) FDTD simulation result of a combined angled-grating resonator. 19
2.3 Planar geometry of a zig-zag coherently combined laser array. Coupling regions are marked by red triangles. Coherently combined outputs (marked in black circle) constructively interfere in the far field. 21
2.4 Topographic structures of different passive beam combining systems. Adjacent laser beams are connected by 2X2 coupler.(a) The proposed zigzag-like structure. Each laser beam is directly coupled with adjacent neighbors. The system has N/2 output ports; (b)The tree-like structure. The system has only one output port. schematic.eps 22
2.5 Dependence of eigenvalues on phase variation $\Delta\Phi$ and total beam number N in the zigzag array structure. phase_noise.eps 24
2.6 Normalized I_G vs. $\frac{\theta d}{\lambda}$. The solid line shows the ideal case. The dash line shows the fully correlated case. The dot-dash line shows the adjacent correlated case. In the simulation, σ_ϕ is set to be $\pi/5$ [1]. IG.eps 30
2.7 (a) Brightness with respect to the standard variation of phase noise σ_ϕ. N is set to be 30 in the calculation;(b) Brightness with respect to the number of emitters N. σ_ϕ is set to be $\pi/8$ in the calculation. The solid line shows the ideal case. The dash line shows the fully correlated case and the dot-dash line shows the adjacent correlated case. Brightness.eps 31
2.8 The fundamental slab waveguide mode profile and refractive index profile of the InGaAsP/InP wafer design 33
2.9 The coupling coefficient at different etching depth of the surface etched gratings in InGaAsP/InP epitaxy wafer. 35
2.10 The fundamental slab waveguide mode profile and refractive index profile of the InGaAs/GaAs wafer design 36

3.1 Overview of the fabrication procedures of two coherently combined angled-grating broad-area lases with surface etched gratings 40
3.2 SEM picture of the resist after the reflow process. 41
3.3 Top view (a) and cross section view (b) of the ebeam resist after development. 42
3.4 Cross section view of devices after SiO_2 layer dry etched. 43

Figure **Page**

3.5 Cross section view of the device after III-V dry etch. 44
3.6 Cross section view of BCB planarization after BCB layer is completely cured. 45
3.7 SEM pictures of devices after the step of BCB etch back. (a) the 1D grating area; (b) 2D overlapped area. 46
3.8 Cross section view of the device after depositing P metal contact. 47
3.9 Schematic plot of the cleavage process: from die to separate laser diode. . . 49
3.10 The image of the packaged device. 51
3.11 Overview of the fabrication procedures of two coherently combined angled-grating broad-area lases with regrowth gratings 52
3.12 Cross section view of the wet etched gratings (a) with SiO2etch mask (b) after removing the etch mask. 54

4.1 Schematic plot of the measurement setup for L-I curve, near field, far field and optical spectrum. 57
4.2 The optical power head response of the laser output in one period of QCW measurement. 58
4.3 Schematic plot of the far field profile scanning setup. 60
4.4 Measurements of the light-current curve and optical spectrum. (a) L-I curves of the combined angled-grating laser (solid line) and the single emitter (dashed line). (b) Spectrum of the combined laser diode when the injection current is 1200mA. The inset is a zoomed-in spectrum in the black circle. 61
4.5 Measurements of the near field and far field of the coupled emitter and single emitter. (a, b) The near field image and profile of the coupled emitter; (c, d) The far field image and profile of the coupled emitter; (e, f) The far field image and profile of a single emitter. 63
4.6 Far-field profiles of the coherently combined laser and simulation result. Solid line presents the measurement result of the coherently combined laser and the dashed line is the simulation result. 64
4.7 Simulation geometry in COMSOL®. The inset is a zoom-in view around the metal contact. The isolated interfaces are marked in red. 65
4.8 Simulation results of the injected current distribution. (a) Nonuniform current distribution without ion-implantation. (b) The distribution becomes more uniform after increasing the resistance outside the grating area.(c) and (d) Electric fields of the first and second order Bragg modes, respectively. (e) Normalized line current density corresponding to (a) in dashed red line and (b) in solid blue line. 66
4.9 Near field images after proton implantation at different energies with the dose of $5\times10^{14}/cm^2$. (a) Not implanted. (b) Ion energy is $180KeV$. (c) Ion energy is $220KeV$. (d) Ion energy is $260KeV$. Between the dashed lines is the emitting aperture. 68

Figure Page

4.10 (a) Near field of the coupled laser. The inset is the camera image. (b) Far field profiles: the blue solid line is the measured far field of the coupled laser, the green dashed line is the calculated far field and the red dash-dot line represents the measured far field of a single angled-grating broad-area laser. We obtain a good agreement between the measured and calculated far field. The inset is the camera image. 69
4.11 (a) L-I curve. (b) Spectra at two different pump currents. 70
4.12 Camera image of the broken insulation layer and exposed semiconductor after scribing. 72
4.13 (a) LI curves of the p-side-up bonded(in red) and p-side-down bonded(in blue) single angled-grating broad-area lasers.(b) LI curves of the p-side-down bonded single angled-grating broad-area laser(in solid blue line) and two coherently combined lasers(in red line). The dashed line is the twice of the single emitter output power at doubled pump current to be compared to the combined output. 73
4.14 LI curve of the two combined laser with quasi-CW pumping on a TEC heat sink setted as $16°C$. The pumping pulses are $1ms$ width with 20% duty cycle. 73
4.15 (a) Top view of a completed laser mini bar. The inset is the zoom-in view of the coupling region. (b) Cross-section of the gratings. From left to right, the insets are the zoom-in view of one tooth of the gratings and zoom-in view of the stretched-out BCB filling, respectively. (c) Top view of gratings at the facet. The stretched-out BCB fillings are shown in the red circle. 73
4.16 (a) Light power vs. current curve of the mini laser bar. (b) Light spectrum of three apertures at 2000mA; the inset is the zoom-in view between 1524.5nm and 1526nm. 74
4.17 Diagram of the optical setup used to measure the optical spectrum of each aperture. 75
4.18 Near field and far field profiles of the three coherent output apertures of a mini-bar at 2000mA. (a) Near field profile. (b) Measured far field profile(blue solid line); calculated far field profile(red dashed line); far field profile of a single angled-grating broad-area laser(green dash-dotted line). . 75
4.19 Near field and far field profiles of the four coherent output apertures of a mini-bar at 2000mA. (a) Near field profile. (b) Measured far field profile. . . 76
4.20 Coarse far field profile of the six combined laser mini bar in a large range of divergent angle. Two side peaks present at around 35°. 77
4.21 Schematic plot of the reflection of Bragg modes and small modal angle modes in the combined laser mini bar. P1, P2 and P3 are the labels of the output ports. 78
4.22 (a) Facet coating design; (b) Plot of the reflectivity of the coating in(a) at different incident angles. 79

Figure		Page

4.23 (a)SEM picture of the designed facet coating;(b) Near field of the laser mini bar with the facet coating. 79
4.24 SEM pictures of the defects in the regrowth wafer. 80

5.1 Schematic plot of rectangle and triangle 2D photonic crystal cavities substituting the 1D TBR grating. 82
5.2 (a)Geometries and relationship with k vector in a triangle lattic with $\vec{a}_1$ and $\vec{a}_2$ as the base vectors;(b) Reciprocal lattice of (a) with $\vec{b}_1$ and $\vec{b}_2$ as the base vectors. 83
5.3 Band structures of triangle lattice with first four bands along both $\vec{k}_x$ and $\vec{k}_y$ direction,k_x is normalized by $\frac{2\pi}{d\cos\theta}$ and k_y is normalized by $\frac{2\pi}{l}$. 83
5.4 Relation between m and θ in the 2D photonic crystal cavity design 86
5.5 Schematic plot of 2D photoic crystal cavity with triangle lattice. 86
5.6 The plot of κ_x with respect to the etch depth 90
5.7 SEM picture of the cross section of a 2D photonic crystal Bragg laser. . . . 91
5.8 (a) LI curves of the single triangle lattice and rectangle lattice 2D photonic crystal Bragg lasers with the same parameters. (b) Optical spectrum of single triangle lattice 2D photonic crystal Bragg laser. 91
5.9 (a) Near field profile of single 2D PC Bragg laser. The camera image is shown in the inset. (b) Far field profile of single 2D PC Bragg laser. The inset is the camera image. 92
5.10 (a) LI curves of the single and two combined 2D PC Bragg lasers; (b) Far field profile of the two combined 2D PC Bragg lasers. 92

6.1 Schematic plot of a folded angled-grating broad-area laser. 94
6.2 (a) and (b) Simulation result and mode profile of an unfolded angled-grating broad-area laser; (c) Mode coupling in a folded cavity angled-grating broad-area laser. The inset is the zoom-in view at the interface; (d) Simulation result of the preferred mode when $L = 4NL_c$; (e) Simulation result of high diffraction loss when $L = (4N + 2)L_c$. 97
6.3 (a) Top view of the packaged folded cavity angled-grating broad-area laser. The inset is the zoom-in view at the interface; (b) Cross-section of the folded cavity laser. The inset is the zoom in view of one etched trench. . . . 97
6.4 (a) Near field profiles of the folded cavity(blue solid line) and unfolded cavity(red dashed line). (b) Far field profiles and camera images of the folded cavity(blued solid line) and unfolded cavity(red dashed line). The calculated far field is shown in green dash-dotted line. (c) Light-current curves of the folded cavity(blue solid line) and unfolded cavity(red dashed line). (d) Optical spectrum of the folded cavity(blue solid line) and unfolded cavity(red dashed line). 99

Figure **Page**

6.5 Schematic plot of the combined folded angled-grating broad-area laser.Two folded angled-grating broad-area lasers are coherently combined in the same way as in the combined angled-grating broad-area laser. The distance between the two emitters is reduced, resulting in an increased angular distance in the far field. 100

6.6 (a) Near field profile and (b) Far field profile of the coherently combined folded angled-grating broad-area laser. 101

Chapter 1

INTRODUCTION

The semiconductor laser [2–6] has already been widely used in the applications of telecommunication [7–10], sensing [11–13], illumination [14–17] and optical pumping [18–21], ever since invented. Compared to other types of lasers, the semiconductor laser has the advantages in high power conversion efficiency, compactness, ability to be electrically pumped and to be integrated with other semiconductor devices. High output power is one of the features in the semiconductor laser design that are most desired by most applications. Higher laser output power can benefit those applications, for example, higher SNR(signal to noise ratio), higher sensitivity, higher illuminance and higher optical pumping efficiency. High brightness is another parameter for optimization in the semiconductor laser design which describes the power density per emiting area per emiting angle. Besides high output power, high brightness alos requires diffraction-limited beam quality which is only limited by the diffraction theory. The brightness becomes a critical parameter when coming to the coupling from a laser beam to a optical fiber or crystal. A very good example in practice is the diode pumped solid-state laser(DPSSL) [22]. For very high output power of DPSSL, diode laser bar or stack is used as the pumping source. However, the poor beam quality of the pumping source limits the energy that can be focused on the bulk crystal and

diminishes the improvement of pumping efficiency induced by the high output power of the pumping diodes. Therefore, novel laser diode design with high output power as well as high brightness is highly desired and has been a hot research topic for decades.

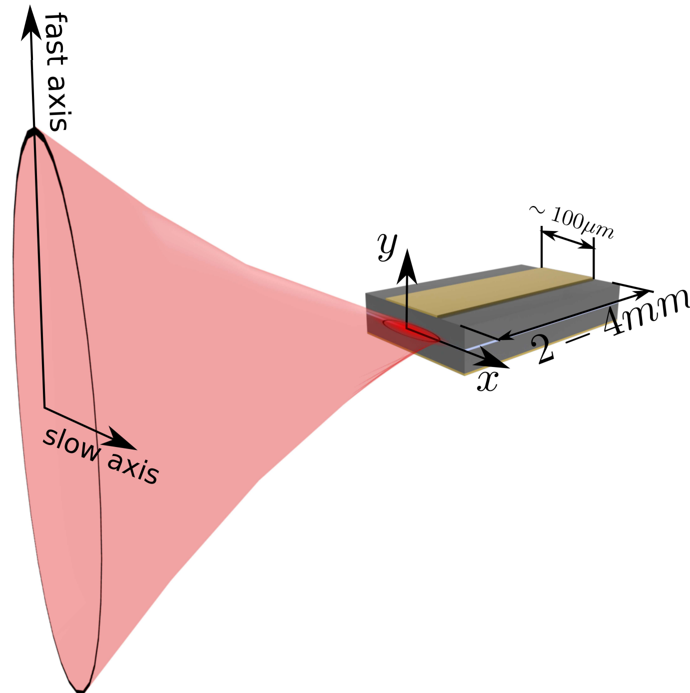

Figure 1.1: Schematic plot of a conventional broad-area laser and the beam profile at near and far field. Slow axis(x axis) has a small divergence angle and fast axis(y axis) has a large divergence angle.

It is quite challenging to simultaneously obtain high power and good beam quality with conventional index-guided laser cavity design in the edge emitting laser diodes as shown in Fig. 1.1. For high power operation, a broad-area, large emitting aperture is usually needed. The reason for that is not as simple as providing higher optical gain. A large emitting aperture also reduces the power density on the facet to postpone the happening of catastrophe optical damage (COD) [23, 24] on the laser facets, which is another factor limiting the maximum output power. Besides, broad-area design helps with the heat dissipation and therefore, diminishes the thermal rollover at high output power. Therefore, a commercial available high power broad-area laser diode is usually around 100*um* wide and 2 to 4*mm*

long. For high brightness, single transverse mode is required for diffraction-limited beam quality. As in the edge emitting laser diodes, there is large asymmetry of the emitting aperture which has much larger size in the x axis(tens to one hundred microns) than in the y axis(only several microns) as shown in Fig. 1.1. Usually, the multi epi-layers structure is designed to support single mode. And the beam quality in the y axis is usually considered to be diffraction-limited beam quality. Therefore, only the beam quality in the x axis should be optimized to obtain diffraction-limited beam quality in the edge emitting laser diodes. When we combine both requirements for high power and diffraction-limited beam quality in the index-guided laser cavity design, it results in a broad-area waveguide with very weak refractive index contrast to obtain single transverse mode. However, the refractive index contrast is so weak that it is not robust enough against the index perturbation due to the strong nonlinear effects in the semiconductor materials with large pumping current [25–27]. Therefore, the broad-area weak-index-guiding waveguide laser cavity design usually results in multimode operation at high output power.

1.1 Angled-grating Broad-area Lasers

The key to maintain single transverse mode at high output power is to find a lasing mode with both low threshold modal gain and large modal discrimination. The low threshold modal gain ensures that it can be selected as the lasing mode and the large modal discrimination can prevent the high order modes from lasing even at high output power and maintain the single transverse mode operation. The angled-grating broad-area laser [28–32] design is one of such novel single emitter designs for both high power and high brightness operation [33–41]. Figure 1.2 shows the schematic plot of the angled-grating broad-area laser. The laser cavity consists of a broad-area transverse Bragg resonance(TBR) grating with a tilting angle. The tilting cavity design and TBR grating are two key points to obtain single

transerve mode at high output power in this design.

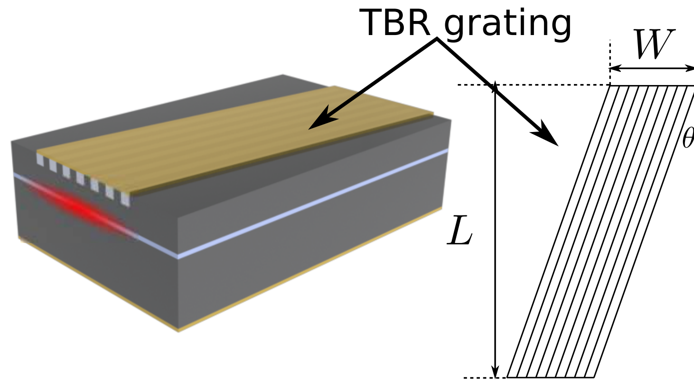

Figure 1.2: Schematic plot of the angled-grating broad-area laser. The laser cavity consists of a tilting broad-area TBR grating.

1.1.1 TBR grating

The TBR grating is used to confine the transverse mode and provide a large modal discrimination. Figure 1.3(a) shows the refractive index profile of a TBR grating. In this figure, β is the propagation constant and k_x is the transverse wavevector. The modal angle is the angle between β and the k vector. Either couple mode theory [42–44] or transfer matrix method(TMM) [45] can be used to solve for β. In the coupled mode theory, starting from the coupled wave equation:

$$\frac{\partial^2 E(x,z)}{\partial x^2} + \frac{\partial^2 E(x,z)}{\partial z^2} = -k_0^2(\varepsilon_0 + \Delta\varepsilon(x,z))E(x,z) \tag{1.1}$$

where ε_0 is the effective permittivity, $\Delta\varepsilon(x,z)$ is the permittivity difference and $E(x,z)$ is the electrical field distribution which can be written as

$$\begin{aligned} E(x,z) &= a_r(x,z)e^{-jk_x x}e^{-j\beta z} + a_l(x,z)e^{jk_x x}e^{-j\beta z} \\ &\quad + b_r(x,z)e^{-jk_x x}e^{j\beta z} + b_l(x,z)e^{jk_x x}e^{j\beta z} \end{aligned} \tag{1.2}$$

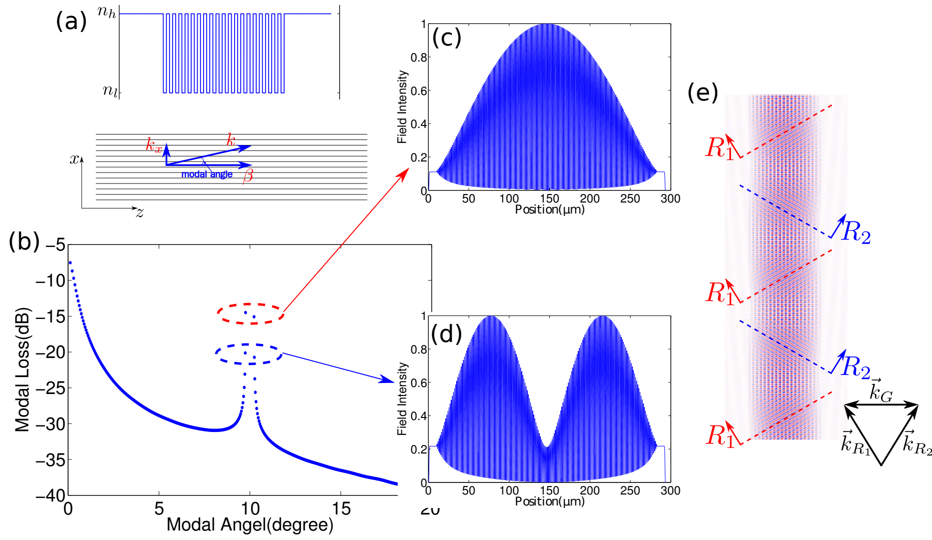

Figure 1.3: (a) Refractive index profile of a TBR grating; (b) Plot of modal loss with respective to different modal angles; (c) and (d) Electric field profiles of first and second order Bragg modes; (e) FDTD simulation result of the beating pattern of the two first order Bragg modes.

where a_r, a_l, b_l and b_r are shown in Fig. 1.4.

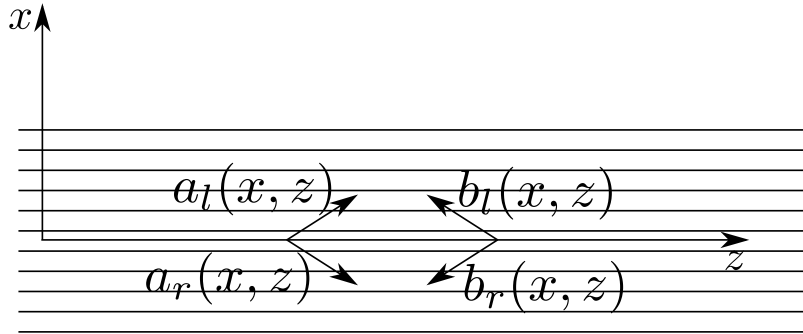

Figure 1.4: Schematic plot of a TBR cavity.

We can substitute Equ. 1.1 with Equ. 1.2 and obtain

$$
\begin{aligned}
&\frac{\partial^2 a_r(x,z)}{\partial x^2}e^{-jk_x x}e^{-j\beta z} - 2jk_x\frac{\partial a_r(x,z)}{\partial x}e^{-jk_x x}e^{-j\beta z} - a_r(x,z)k_x^2 e^{-jk_x x}e^{-j\beta z}\\
&+\frac{\partial^2 a_l(x,z)}{\partial x^2}e^{jk_x x}e^{-j\beta z} + 2jk_x\frac{\partial a_l(x,z)}{\partial x}e^{jk_x x}e^{-j\beta z} - a_l(x,z)k_x^2 e^{jk_x x}e^{-j\beta z}\\
&+\frac{\partial^2 b_r(x,z)}{\partial x^2}e^{-jk_x x}e^{j\beta z} - 2jk_x\frac{\partial b_r(x,z)}{\partial x}e^{-jk_x x}e^{j\beta z} - b_r(x,z)k_x^2 e^{-jk_x x}e^{j\beta z}\\
&+\frac{\partial^2 b_l(x,z)}{\partial x^2}e^{jk_x x}e^{j\beta z} + 2jk_x\frac{\partial b_l(x,z)}{\partial x}e^{jk_x x}e^{j\beta z} - b_l(x,z)k_x^2 e^{jk_x x}e^{j\beta z}\\
&+\frac{\partial^2 a_r(x,z)}{\partial z^2}e^{-jk_x x}e^{-j\beta z} - 2j\beta\frac{\partial a_r(x,z)}{\partial z}e^{-jk_x x}e^{-j\beta z} - a_r(x,z)\beta^2 e^{-jk_x x}e^{-j\beta z}\\
&+\frac{\partial^2 a_l(x,z)}{\partial z^2}e^{jk_x x}e^{-j\beta z} - 2j\beta\frac{\partial a_l(x,z)}{\partial z}e^{jk_x x}e^{-j\beta z} - a_l(x,z)\beta^2 e^{jk_x x}e^{-j\beta z}\\
&+\frac{\partial^2 b_r(x,z)}{\partial z^2}e^{-jk_x x}e^{j\beta z} + 2j\beta\frac{\partial b_r(x,z)}{\partial z}e^{-jk_x x}e^{j\beta z} - b_r(x,z)\beta^2 e^{-jk_x x}e^{j\beta z}\\
&+\frac{\partial^2 b_l(x,z)}{\partial z^2}e^{jk_x x}e^{j\beta z} + 2j\beta\frac{\partial b_l(x,z)}{\partial z}e^{jk_x x}e^{j\beta z} - b_l(x,z)\beta^2 e^{jk_x x}e^{j\beta z}\\
&= - k_0^2(\varepsilon_0 + \Delta\varepsilon(x,z))\left(a_r(x,z)e^{-jk_x x}e^{-j\beta z} + a_l(x,z)e^{jk_x x}e^{-j\beta z}\right.\\
&\quad \left.+b_r(x,z)e^{-jk_x x}e^{j\beta z} + b_l(x,z)e^{jk_x x}e^{j\beta z}\right)
\end{aligned}
\tag{1.3}
$$

We can use slow variation assumption and ignore the second derivative terms. Thus, we can obtain

$$
\begin{aligned}
&\left(-2jk_x\frac{\partial a_r(x,z)}{\partial x} - 2j\beta\frac{\partial a_r(x,z)}{\partial z}\right)e^{-jk_x x}e^{-j\beta z} - a_r(x,z)(k_x^2+\beta^2)e^{-jk_x x}e^{-j\beta z}\\
&+\left(2jk_x\frac{\partial a_l(x,z)}{\partial x} - 2j\beta\frac{\partial a_l(x,z)}{\partial z}\right)e^{jk_x x}e^{-j\beta z} - a_l(x,z)(k_x^2+\beta^2)e^{jk_x x}e^{-j\beta z}\\
&+\left(-2jk_x\frac{\partial b_r(x,z)}{\partial x} + 2j\beta\frac{\partial b_r(x,z)}{\partial z}\right)e^{-jk_x x}e^{j\beta z} - b_r(x,z)(k_x^2+\beta^2)e^{-jk_x x}e^{j\beta z}\\
&+\left(2jk_x\frac{\partial b_l(x,z)}{\partial x} + 2j\beta\frac{\partial b_l(x,z)}{\partial z}\right)e^{jk_x x}e^{j\beta z} - b_l(x,z)(k_x^2+\beta^2)e^{jk_x x}e^{j\beta z}\\
&= - k_0^2(\varepsilon_0 + \Delta\varepsilon(x,z))\left(a_r(x,z)e^{-jk_x x}e^{-j\beta z} + a_l(x,z)e^{jk_x x}e^{-j\beta z}\right.\\
&\quad \left.+b_r(x,z)e^{-jk_x x}e^{j\beta z} + b_l(x,z)e^{jk_x x}e^{j\beta z}\right)
\end{aligned}
\tag{1.4}
$$

Since $k_x^2 + \beta^2 = k_0^2\varepsilon_0$, the above equation can be simplified as

$$\left(-2jk_x\frac{\partial a_r(x,z)}{\partial x} - 2j\beta\frac{\partial a_r(x,z)}{\partial z}\right)e^{-jk_xx}e^{-j\beta z} + \left(2jk_x\frac{\partial a_l(x,z)}{\partial x} - 2j\beta\frac{\partial a_l(x,z)}{\partial z}\right)e^{jk_xx}e^{-j\beta z}$$
$$+\left(-2jk_x\frac{\partial b_r(x,z)}{\partial x} + 2j\beta\frac{\partial b_r(x,z)}{\partial z}\right)e^{-jk_xx}e^{j\beta z} + \left(2jk_x\frac{\partial b_l(x,z)}{\partial x} + 2j\beta\frac{\partial b_l(x,z)}{\partial z}\right)e^{jk_xx}e^{j\beta z}$$
$$= -k_0^2\Delta\varepsilon(x,z)\left(a_r(x,z)e^{-jk_xx}e^{-j\beta z} + a_l(x,z)e^{jk_xx}e^{-j\beta z} + b_r(x,z)e^{-jk_xx}e^{j\beta z} + b_l(x,z)e^{jk_xx}e^{j\beta z}\right) \tag{1.5}$$

where $\Delta\varepsilon(x,z)$ can be expressed as

$$\Delta\varepsilon(x,z) = \sum_m \Delta\varepsilon_m e^{-iK_mx} \tag{1.6}$$

where

$$K_m = m\frac{2\pi}{\Lambda}$$

and

$$\Delta\varepsilon_m = \frac{1}{\Lambda}\int_0^\Lambda \Delta\varepsilon(x)e^{iK_mx}dx$$

If we only consider the first order grating, the coupling between a_r, a_l, b_l and b_r is shown

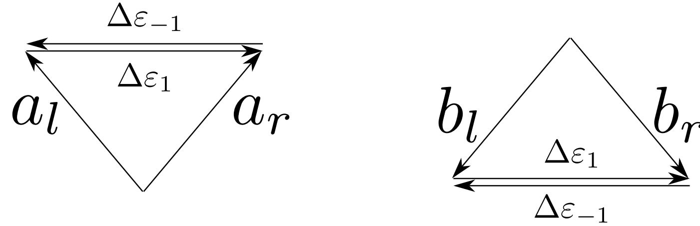

Figure 1.5: The coupling relationship between the grating vectors and a_r, a_l, b_r and b_l.

in Fig. 1.5 and Equ. 1.5 can be written as

$$\begin{aligned}
&\left(-2jk_x\frac{\partial a_r(x,z)}{\partial x}-2j\beta\frac{\partial a_r(x,z)}{\partial z}\right)e^{-jk_xx}e^{-j\beta z}=-k_0^2\Delta\varepsilon_1 e^{-iK_1x}a_l(x,z)e^{jk_xx}e^{-j\beta z}\\
&\left(2jk_x\frac{\partial a_l(x,z)}{\partial x}-2j\beta\frac{\partial a_l(x,z)}{\partial z}\right)e^{jk_xx}e^{-j\beta z}=-k_0^2\Delta\varepsilon_{-1} e^{-iK_{-1}x}a_r(x,z)e^{-jk_xx}e^{-j\beta z}\\
&\left(-2jk_x\frac{\partial b_r(x,z)}{\partial x}+2j\beta\frac{\partial b_r(x,z)}{\partial z}\right)e^{-jk_xx}e^{j\beta z}=-k_0^2\Delta\varepsilon_1 e^{-iK_1x}b_l(x,z)e^{jk_xx}e^{j\beta z}\\
&\left(2jk_x\frac{\partial b_l(x,z)}{\partial x}+2j\beta\frac{\partial b_l(x,z)}{\partial z}\right)e^{jk_xx}e^{j\beta z}=-k_0^2\Delta\varepsilon_{-1} e^{-iK_{-1}x}b_r(x,z)e^{-jk_xx}e^{j\beta z}
\end{aligned} \tag{1.7}$$

Since $k_x-K_1=-k_x$ and $-k_x-K_{-1}=k_x$, Equ. 1.7 can be simplified as

$$\begin{aligned}
k_x\frac{\partial a_r(x,z)}{\partial x}+\beta\frac{\partial a_r(x,z)}{\partial z}&=-j\frac{k_0^2}{2}\Delta\varepsilon_1 a_l(x,z)\\
k_x\frac{\partial a_l(x,z)}{\partial x}-\beta\frac{\partial a_l(x,z)}{\partial z}&=j\frac{k_0^2}{2}\Delta\varepsilon_{-1} a_r(x,z)\\
k_x\frac{\partial b_r(x,z)}{\partial x}-\beta\frac{\partial b_r(x,z)}{\partial z}&=-j\frac{k_0^2}{2}\Delta\varepsilon_1 b_l(x,z)\\
k_x\frac{\partial b_l(x,z)}{\partial x}+\beta\frac{\partial b_l(x,z)}{\partial z}&=j\frac{k_0^2}{2}\Delta\varepsilon_{-1} b_r(x,z)
\end{aligned} \tag{1.8}$$

And the TBR mode can be obtained by solving the couple mode equations Equ. 1.8 through separation of variables method.

When using TMM, the TBR grating can be considered as a multi layer structure as shown in Fig. 1.6 and the transmission and reflection electric fields of each layer can be described by a transfer matrix as follows:

$$\begin{bmatrix}E_3\\E_4\end{bmatrix}=\begin{bmatrix}\frac{1}{t_{12}}e^{-jn_ik_0d_i} & \frac{r_{21}}{t_{12}}e^{-jn_ik_0d_i}\\ -\frac{r_{12}}{t_{12}}e^{jn_ik_0d_i} & \frac{1}{t_{12}}e^{jn_ik_0d_i}\end{bmatrix}\begin{bmatrix}E_1\\E_2\end{bmatrix} \tag{1.9}$$

Therefore, the transfer matrix of the TBR grating can be obtained by multiplying all the

transfer matrices of each single layer and can be expressed as

$$\begin{bmatrix} E_o \\ E_b \end{bmatrix} = \begin{bmatrix} A & B \\ C & D \end{bmatrix} \begin{bmatrix} E_i \\ E_r \end{bmatrix} \tag{1.10}$$

Applying the boundary conditions, $E_i = 0$ and $E_b = 0$ result in $D = 0$. And β can be obtained by solving this equation.

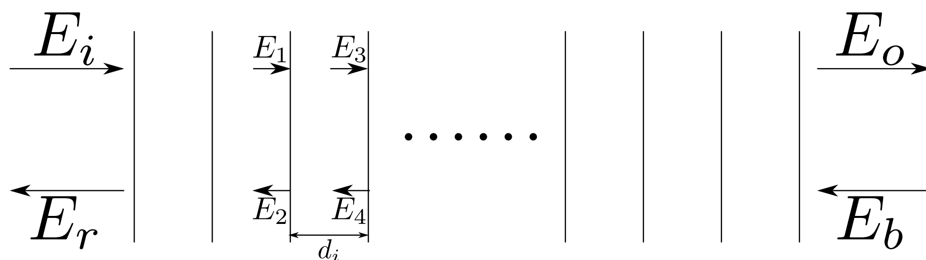

Figure 1.6: Schematic plot of the multi layer structure using TMM.

The modal loss which is the imaginary part of β with respective to modal angle is shown in Fig. 1.3(b). At small modal angles, the modal loss is low because of small diffraction loss. These modes are referred as small angle modes. When modal angle increases, the diffraction loss increases as well as the modal loss, just like in a plain waveguide. However, at a certain angle, there are some Bragg modes with low modal loss since the transverse wavevector of these modes are resonate with the gratings. The relationship between the grating period and the resonate modal angle can be obtained through the Bragg condition as follows:

$$\Lambda = \frac{\lambda}{2n_{eff} \sin\theta} \tag{1.11}$$

Compared to the small angle modes, the Bragg modes have a large modal discrimination which is defined as the modal loss difference between the first order (in the red circle) and the second order (in the blue circle) Bragg modes. The electric fields of the first and second order Bragg modes are shown in Fig. 1.3 (d) and (e), respectively. It is also shown that

the modal loss difference between the two first order Bragg modes are so small that these two first order Bragg modes can be considered as degenerated modes. And both of them can lase when electrically pumped. Therefore, the lasing mode is the sum of the two first Bragg modes. Figure 1.3(e) shows the beating pattern of the two first order Bragg modes calculated by FDTD simulation. In this figure, the snake-like mode profile consists of two planewave-like components, R_1 and R_2. And from the point view of couple mode theory, along propagation, the two components can be coupled with each other through the grating vector. The relationship between the k vectors of these two components and the grating vector is shown in the inset. The angle between $\vec{k}_{R_1}$ and $\vec{k}_{R_2}$ is twice of θ and the difference vector between $\vec{k}_{R_1}$ and $\vec{k}_{R_2}$ is equal to the grating vector which is the same as described by the coupled mode equations.

1.1.2 Tilted cavity design

We have analyzed the modes in the TBR grating and found the Bragg modes with large modal discrimination which is promising to obtain single transverse mode operation even at high power output. However, in a straight TBR grating cavity, instead of Bragg modes, the small angle modes are more likely to be selected as the lasing mode, since they have less modal loss than the Bragg modes according to Fig. 1.3(b). Therefore, a cavity feedback mechanism is needed to favor the Bragg modes against the small modal angle modes. And the titled cavity design is proposed for this purpose. Considering the two planwave-like components in the snake-like Bragg mode propagation pattern, if we set the facets along either R_1 components or R_2 components, we can obtain a tilted cavity with the tilting angle the same as the resonance modal angle, as shown in Fig. 1.7. In such a tilted cavity design, the Bragg modes are reflected perpendicularly at the facets. And there is a 2θ angle mismatch when small angle modes are reflected at the facets, resulting in a large reflection

loss. Therefore, the tilted cavity design can suppress the small angle modes by introducing a large reflection loss. Figure. 1.7 shows the FDTD simulation results of the Bragg modes in a titled cavity.

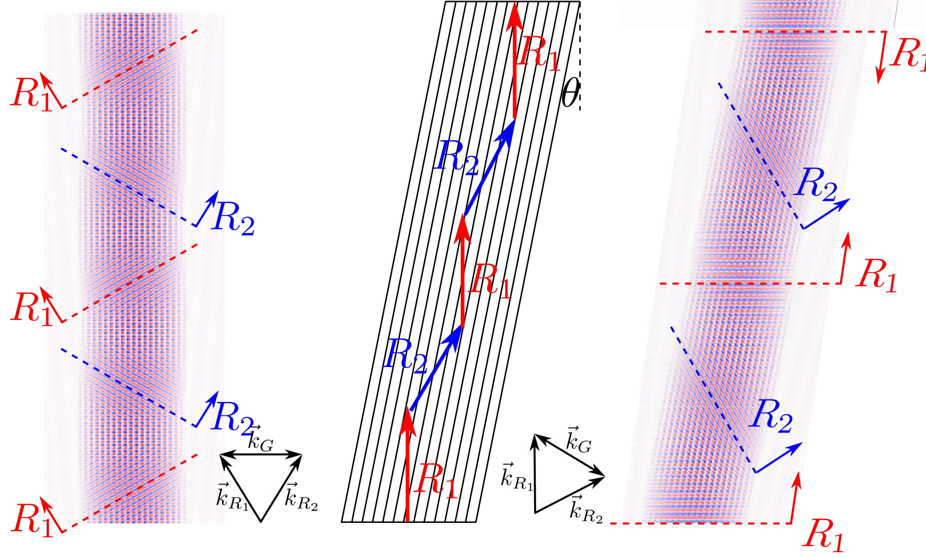

Figure 1.7: Schematic plot and FDTD simulation results of the Bragg modes in a tilted cavity.

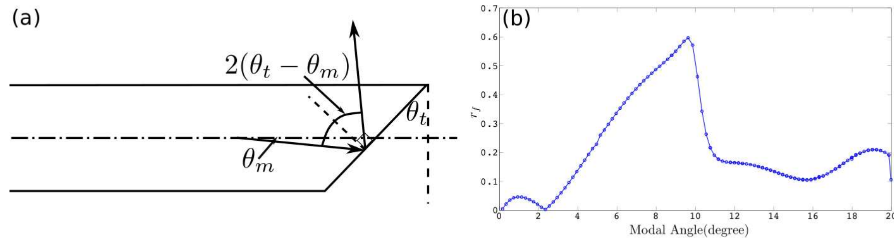

Figure 1.8: Calulation model (a) and result (b) of the reflection of a tilted facet.

The reflectivity of a tilted facet is examined in Ref. [46]. The schematic plot of this model is shown in Fig. 1.8(a). The cavity has a titled facet with the angle of θ_t. When a guided mode with the modal angle of θ_m is reflected at the titled facet, there is a angle mismatch of $2(\theta_t - \theta_m)$ between the guided and reflected mode profiles. The reflectivity should only consider the reflected energy of the same guided mode excited by the reflected

electrical field and the angled mismatch is taken into consideration by multiplying an extra phaser as follows to the reflected field:

$$e^{j\beta \sin(2(\theta_t - \theta_m))x} \tag{1.12}$$

The reflectivity in this model can be expressed as

$$R_f = R(\theta_m, \theta_t) r_f \text{ and } r_f = \beta \int_{-\infty}^{\infty} |E|^2 e^{j\beta \sin(2(\theta_t - \theta_m))x} dx \tag{1.13}$$

where $R(\theta_m, \theta_t)$ is the Fresnel reflection coefficient of the guided mode with modal angle of θ_m, β is the propagation constant and x is the coordinate along the tilted facet. Figure 1.8(b) shows the r_f of different modes with various modal angles. The tilted angle in this simulation is set to be 10°. And it is shown that the maximum r_f happens around 10° which is the same as the tilted angle of the cavity. Therefore, the tilted cavity design is the key point to eliminate the small modal angle modes and make the Bragg modes as the lasing mode by introducing an extra reflection loss to the small modal angle modes.

To briefly sum up, we have shown the importance of the TBR grating and tilted cavity design in the angled-grating broad-area laser and how it obtains the simultaneous high power and single mode operation. The lasing mode consists of two degenerated band edge modes as shown in Fig. 1.3(b). However, there is a slight difference in the modal loss between these two Bragg modes. And this results in different intensities of these two modes when excited. The problem is that only part of the energy of the two modes can beat with each other if there is too much intensity difference. One way to reduce the difference in modal loss is to make weak gratings. However, a weaker grating increases the modal loss as well. Therefore, there should be a design balance on the coupling strength of the TBR grating. There is a relationship between the modal reflectivity and the grating coupling

coefficient. A weak TBR grating design can help increase the reflectivity of the Bragg modes as shown in Fig. 1.9. The reason is that weaker TBR grating results in less deviation of the modal angel from the designed tilted angle of cavity and less phase mismatch at the facet when reflected.

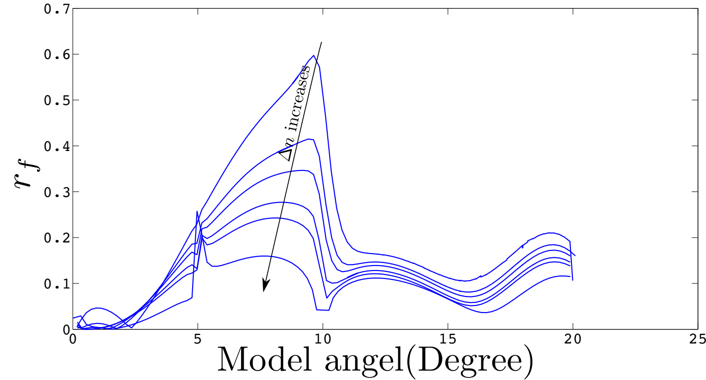

Figure 1.9: Plot of r_f of different modes with several different grating coupling coefficients.

1.2 Coherent Beam Combining

The angled-grating broad-area lasers have already been proved to deliver about $1W$ output power with near-diffraction-limited beam quality in a single emitter. In order to obtain even higher output power, beam combining techniques can be used. There are two methods of beam combining: one is coherent beam combining and the other one is incoherent(wavelength) beam combining [25, 47, 48]. The main difference between these two approaches is that there is constant phase difference between emitters in a coherently combined laser array while in an incoherently combined laser array, the phase difference is random and usually each emitter has a different wavelength and such incoherently combined laser arrays are also referred as wavelength combined arrays. The wavelength beam combining can be realized through a diffraction grating as shown in Fig. 1.10. The combined output power should be N times of a single emitter and the divergence angle of the

combined beam is more or less similar to that of a single emitter. Therefore, the brightness can be improved by N times in a wavelength combined laser array [25, 49, 50].

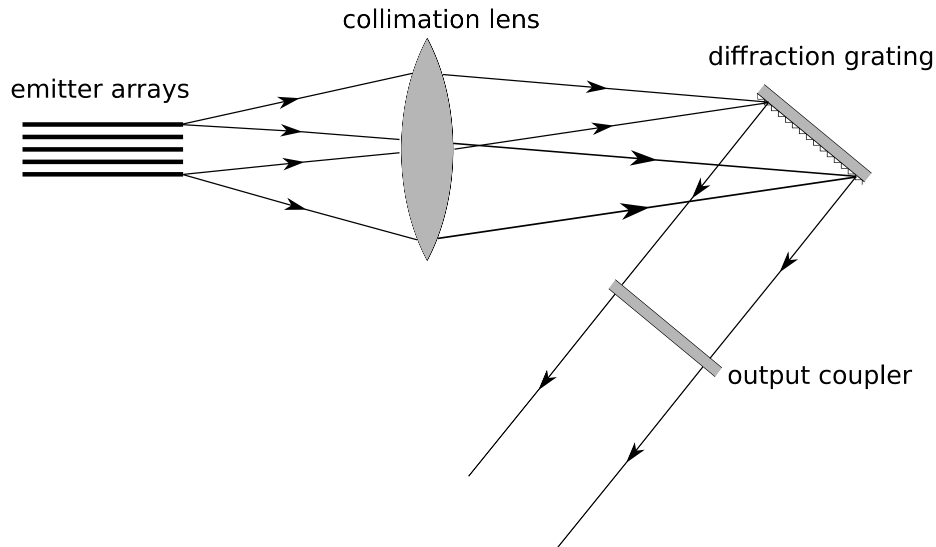

Figure 1.10: Schematic plot of the wavelength beam combining with a diffraction grating.

In an ideal coherently combined laser array with the filling factor around 1, since the emitting aperture is enlarged by N times, the divergence angle of the combined beam becomes $1/N$ of that of a single emitter. Therefore, in an ideal coherently combined laser array, the brightness should be improved by N times of a single emitter. However, since the filling factor is always less than one, in practice, the improvement on brightness of a coherently combined laser array is actually less than N times. Depending on whether external components are needed, coherently combined laser arrays can be divided into two categories. The first category can be monolithically implemented. Several examples are evanescently coupled laser arrays [51, 52], chirped and Y-coupled laser arrays [53–55] and leaky wave coupled (anti-guided) laser arrays [56, 57]. These structures are only compatible with narrow stripe index-guided single-mode lasers or gain-guided lasers. Thus, the total width of conventional coherent diode laser arrays is limited less than a few hundred microns.

The second category requires external cavities or phase control, including externally injection-locked laser arrays [58,59], Talbot cavity laser arrays [60–62], Self-Fourier cavity laser arrays [63, 64] and master oscillator power amplifier (MOPA) arrays [65–72]. The MOPA array is an example of active coherently beam combined laser arrays as shown in Fig. 1.11(a). The phase of each emitter output is measured and used to tune the phase controller array and maintain all the emitters in-phase. The other beam combining methods mentioned above are passive beam combining. The Talbot and Self-Fourier cavity laser arrays are also referred as common cavity laser arrays. In a common cavity laser array, an output coupler is usually used to form an external cavity with the laser array and an in-phase supermode is selected by the external cavity to keep all the emitters in-phase. The Talbot cavity uses the Talbot effect which is a self-imaging effect of a periodic near-field patterns along propagation. The inset of Fig. 1.11(b) shows the one dimensional Talbot effect and the self-repeating length is called Talbot length which is $2a^2/\lambda$ where a is the period of the near-field pattern. Figure 1.11(b) shows the schematic plot of a Talbot cavity laser array. The distance between the output coupler and the laser array is half of the Talbot length. Thus the reflected wave is delayed by a Talbot length, which according to the Talbot effect, is the self-image of the laser array output. Theoretically, the Talbot effect is derived based on infinity number cells in an array. However, when the array is truncated to finite number of elements as in the Talbot laser array, the self-image at the array edges is distorted due to the diffraction loss which will diminish the scalability and coupling efficiency of the Talbot cavity laser arrays. The self-Fourier cavity consists of a Fourier lens along with the output coupler as shown in Fig. 1.11(c). In the self-Fourier external cavity, the distance between the laser facets and the Fourier lens is the focus length of the Fourier lens and the feedback wave is the far field pattern through the Fourier transform by the Fourier lens. Thus, the supermode should have the same near field (emitted wave at laser facets) and far field (feedback wave at laser facets). Instead of the same intensity among all the emitters

in the Talbot cavity, the supermode in the self-Fourier cavity has a Gaussian-like envelope as shown in Fig. 1.11(c). It is obvious that both Talbot and self-Fourier cavities have a high requirement on alignment and positioning of the emitters and the output coupler. Both of them have their own requirement on the distance among the emitters and the distance between the laser facets and the output coupler for high coupling efficiency. Since external cavities and/or accurate phase control are needed, these systems in the second category are usually complex, bulky and not robust [25, 73].

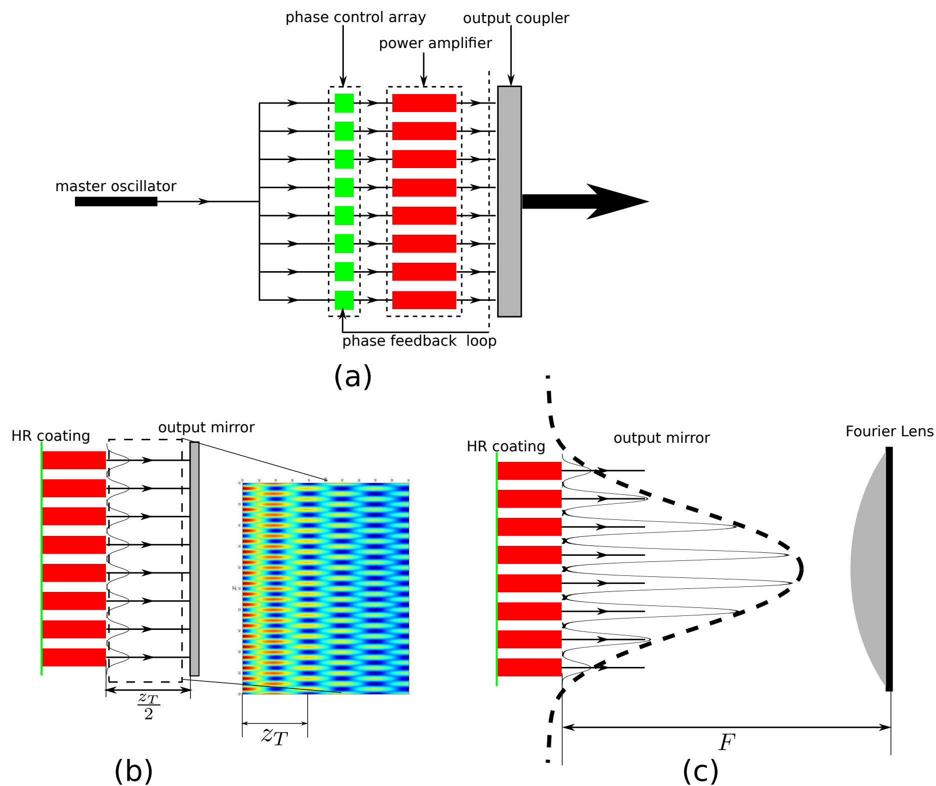

Figure 1.11: Schematic plot of (a) MOPA array, (b) Talbot array and (c) Self-Fourier array

Chapter 2

DESIGN OF COHERENTLY COMBINED ANGLED-GRATING BORAD-AREA LASERS

In the first chapter, we have shown that the angled-grating broad-area laser is a good candidate for the high-power and high-brightness single emitter. The transverse mode is defined by the TBR structure. The beating of the two band-edge modes results in a snake-like zigzag cavity mode which is the preferred lasing mode in the titling cavity design. In this chapter, we propose a simple passive coherent combining structure by using the symmetry of the snake-like mode and the tilting cavity design. Modal analysis of the two coherently combined angled-garting broad-area laser is presented and we show that the proposed structures can be easily expanded to a mini laser lar. We also performed the modal and scalability analysis of a simplified fiber laser combining system with the same topographic structure as the proposed zigzag structure. Comparing to other common cavity passive coherent beam combining methods, the proposed monolithical zigzag beam combining structure should have similar combining efficiency with the same noise intensity.

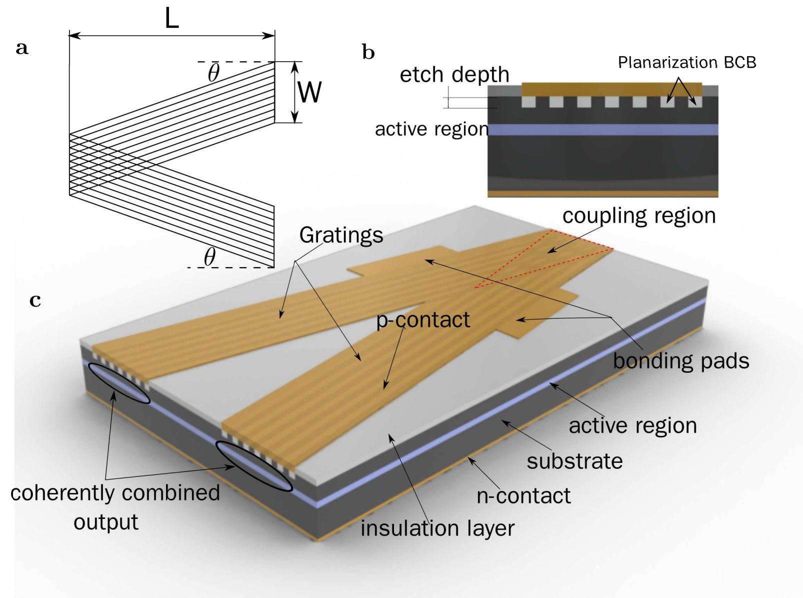

Figure 2.1: Schematic of a coherently combined angled-grating laser. (a) L and W are the length and width of a single emitter, respectively. θ is the tilt angle of the grating. (b) The cross-section structure of a single emitter. (c) Planar geometry of the combined angled-grating laser. Two coherently combined emitters (the output from two legs in the coupled structure) constructively interfere in the far field.

The last part of this chapter contains the epitaxy wafer design as well as parameters of the grating.

2.1 Simultaneous single mode control and coherent beam combining through Bragg diffraction

Figure 6.1 shows a schematic of the two coherently combined angled-grating laser. The combined laser cavity consists of two sets of angled-gratings that tilt to the opposite directions with the same angle. The overlap area of the two gratings defines a two dimensional coupling region. The phase locking of two emitters is obtained by the wave coupling through Bragg diffraction in this overlap region.

The calculated mode of the single angled-grating broad-area laser is a snake-like zigzag

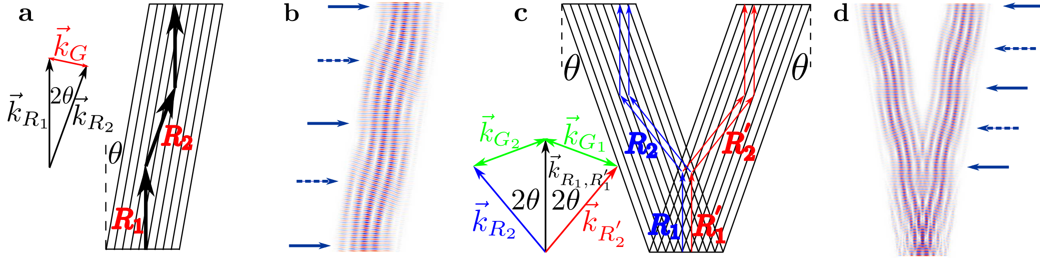

Figure 2.2: Wave coupling and cavity modes in the single emitter and coupled emitter. (a) A single angled-grating emitter. R_1 and R_2 are two planewave-like components resonate with the grating. The phase matching condition between k-vectors is shown in the inset. (b) FDTD simulation result of a single angled-grating resonator. The solid arrows represent the R_1 component and the dashed arrows represent the R_2 component. (c) An on-chip combined angled-grating laser. Arrows in blue represent wave components in the left grating, while arrows in red represent wave components in the right grating. The inset shows the coupling between different wavevectors through the grating. (d) FDTD simulation result of a combined angled-grating resonator.

mode which consists of two planewave-like components in resonance with the grating, R_1 and R_2, as shown in Fig. 2.2(a). The angles between R_1/R_2 and the grating direction are both equal to θ, the grating tilt angle. The wavevectors of R_1, R_2 and the grating satisfy the resonance condition: $\vec{k}_{R_1} + \vec{k}_G = \vec{k}_{R_2}$, as shown in the inset of Fig. 2.2(a). The propagation direction of the R_1 component is perpendicular to the facet and that of R_2 is tilted. When R_1 is reflected by the facet, it will be fed back to the cavity; but for R_2, it will be lost. Therefore, once used as the laser cavity, the angled-grating resonator will self-adaptively select the cavity mode with the maximum R_1 and the minimum R_2 component at the facets. This mode profile is shown in Fig. 2.2(b) which is simulated by FDTD method. Through the large modal discrimination provided by the grating and strong spatial filtering provided by the angle geometry, angled-grating broad-area ($> 100\mu m$) diode lasers can obtain stable single mode operation [28, 29, 43].

Coherent combining of two symmetrical angled-grating emitters that tilt to the opposite directions is obtained by overlapping them with each other at one facet, as shown in Fig. 2.2(c). The overlapped region forms a triangular 2D periodic structure (photonic

crystal), which enables the cross coupling of two single emitters through Bragg diffraction. Outside the coupling region, the cavity modes are the same as that in a single angled-grating emitter. For simplicity, we only take into consideration of the first order Bragg diffraction in the coupling region. Denoted in Fig. 2.2(c), both components R_1 and $R_1^{'}$ can be coupled into R_2 and $R_2^{'}$, respectively, which means that part of energy in one emitter can be injected into the other one in the coupling region. The wavevectors of these four components should satisfy the following phase matching conditions:$\vec{k}_{R_1} + \vec{k}_{G_1} = \vec{k}_{R_2'}$, $\vec{k}_{R_1} + \vec{k}_{G_2} = \vec{k}_{R_2}$, $\vec{k}_{R_1'} + \vec{k}_{G_1} = \vec{k}_{R_2'}$, $\vec{k}_{R_1'} + \vec{k}_{G_2} = \vec{k}_{R_2}$, as shown in the inset of Fig. 2.2(c). Furthermore, R_1 and $R_1^{'}$ should be in phase due to the optical gain provided in the coupling region which would suppress the out-phase interference. Because of the same wavevector selection mechanism in the single emitter, the wave components with the normal incident angle at two facets will be favored. FDTD simulations were carried out to show the preferred mode of a coherently combined laser cavity in Fig. 2.2(d). In this figure, the mode outside the coupling region is still snake-like just as same as that in a single angled-grating laser. In the coupling region, the wave components from two individual lasers constructively interfere, which means that they are efficiently coupled. Thus, mode control and coherent beam combining are simultaneously obtained through Bragg diffraction in this new laser cavity design.

The proposed approach can be expanded to a 1D coherently coupled broad-area laser array. Figure 2.3 shows the schematic of such a coherent array on a laser bar. Strong optical coupling of the cavity modes in the overlap region between any two adjacent lasers leads to phase locking. For each individual laser, the phase accumulated in a round-trip has to be integer multiples of 2π. Therefore, all the emitting apertures along one side of the bar are in phase. Compared to conventional coherent laser arrays, the width of each individual emitter in our design is almost two orders of magnitude larger. In addition, the Bragg diffraction based combining mechanism is much more robust against nonlinear and thermal effects. It should be pointed out that light of one emitter can be directly injected not

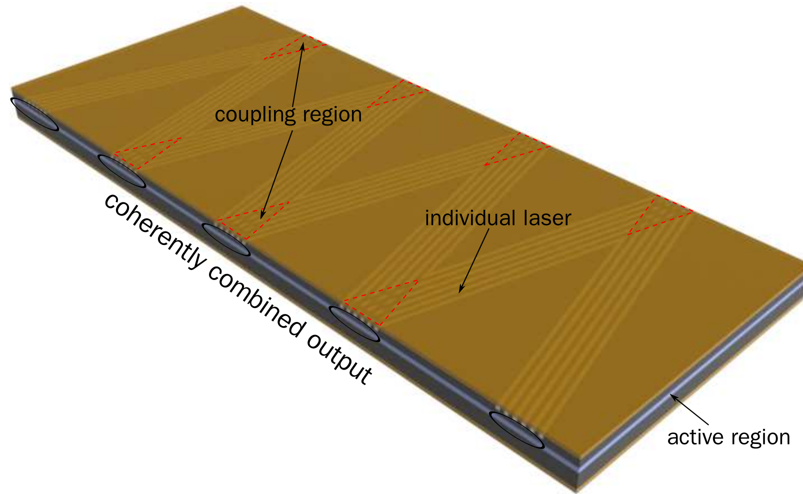

Figure 2.3: Planar geometry of a zig-zag coherently combined laser array. Coupling regions are marked by red triangles. Coherently combined outputs (marked in black circle) constructively interfere in the far field.

only into the adjacent emitters through the coupling regions, but also into other emitters in the array. This implies that a large number of emitters can be coherently combined [25,74], which would lead to a bar-scale single mode diode laser with diffraction-limited output.

2.2 Modal and Scalability Analysis of a Zigzag Structure for Passive Coherent Beam Combining

We have shown that the proposed coherent beam combining structure can be easily expanded to a coherently combined laser array. In this section, we perform the modal and scalability analysis of the proposed zigzag beam combining structure. For simplicity, a fiber laser system with the same topographic structure is used, the schematic plot of which is shown in Fig. 2.4(a). The entire system consists of two groups of mirrors, two groups of couplers, and the laser emitters/gain medium at the center. The red blocks next to the left group of mirrors denote a short length of gain medium, which is important for increasing

the modal discrimination in our structure. This will be discussed in details in the following section. Unlike the conventional tree-like beam combining structure [75, 76] shown in Fig. 2.4(b), no extension of couplers along the light propagating direction is needed in the zigzag array structure when the number of emitters (N) increases, which makes the zigzag array more compact. This is an important advantage for the development of on-chip semiconductor laser systems, since the longer the coupler array, the more nonlinear effects and unwanted feedback it may produce, which will degrade the performance of beam combining. In addition, this proposed zigzag design will save the wafer space and increase the yield. Unlike the Y-junction laser array [77, 78] in which the 2X1 coupler divides the power equally, the proposed zigzag laser array benefits more design flexibility from the 2X2 coupler since we can adjust the power division at two ports to compensate the difference among laser emitters/gain medium in the array. In the following section, a modal analysis is presented to show the supported array super-modes and the performance against the phase variation of the proposed structure. In the third section, based on the assumption that the system operates at a single super-mode, we detail our investigations of the array scalability by means of brightness in the presence of a certain level of phase noise. Then a possible experimental realization is briefly discussed before the conclusion.

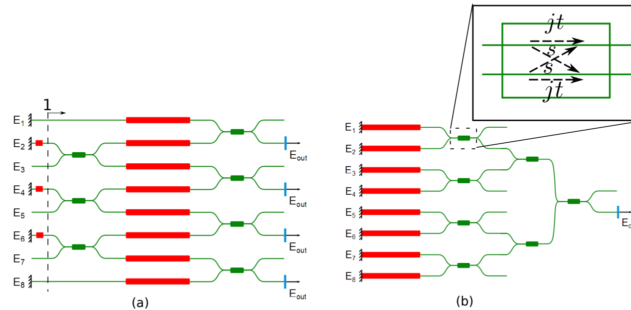

Figure 2.4: Topographic structures of different passive beam combining systems. Adjacent laser beams are connected by 2X2 coupler.(a) The proposed zigzag-like structure. Each laser beam is directly coupled with adjacent neighbors. The system has N/2 output ports; (b)The tree-like structure. The system has only one output port. schematic.eps

2.2.1 Modal analysis

The modal analysis is performed by a transfer matrix method. The building element shown in Fig.2.4(a) is a 2X2 coupler with a transfer function described by a matrix as:

$$\begin{bmatrix} jt & s \\ s & jt \end{bmatrix} \tag{2.1}$$

where t and s are described in the inset of Fig. 2.4(b) and they should satisfy $|t|^2 + |s|^2 = 1$. For simplicity, we use a 50:50 coupler in this paper by setting $r = s = 1/\sqrt{2}$.

Starting from position 1(shown in Fig. 2.4(a)), the round trip matrix for the lightwave propagating in the array can be expressed as:

$$X = R_1 A^* S B^* R_2 B S A \tag{2.2}$$

where A and B are the transfer matrices of the left and right groups of couplers, respectively; S is the phase change in each laser beam; R_1 and R_2 are the reflection matrices of the left and right mirrors and the operator * denotes the complex conjugate. In the following analysis, we assume the left mirrors have perfect reflectivity. To support a super-mode, the array should be able to reproduce the electric field, $\boldsymbol{E}$ after a round trip, which means the following equation should be satisfied:

$$X\boldsymbol{E} = \mu \boldsymbol{E} \tag{2.3}$$

where μ is the eigenvalue of X and $\boldsymbol{E}$ is the eigenvector. Each pair of μ and $\boldsymbol{E}$ corresponds a super-mode. The eigenvalue μ can be regarded as the modal gain and the eigenvector can be used to obtain the power distribution at the output ports. Take $N = 4$ for example, all

the matrices in the round trip matrix, X are expressed as follows:

$$A = \begin{bmatrix} 0 & & & \\ & jt & s & \\ & s & jt & \\ & & & 0 \end{bmatrix}, S = \begin{bmatrix} e^{j\Phi_1} & & & \\ & e^{j\Phi_2} & & \\ & & e^{j\Phi_3} & \\ & & & e^{j\Phi_4} \end{bmatrix}, B = \begin{bmatrix} jt & s & & \\ s & jt & & \\ & & jt & s \\ & & s & jt \end{bmatrix}, \tag{2.4}$$

$$R_1 = \begin{bmatrix} 1 & & & \\ & 1 & & \\ & & 0 & \\ & & & 1 \end{bmatrix}, R_2 = \begin{bmatrix} 0 & & & \\ & R & & \\ & & 0 & \\ & & & R \end{bmatrix}$$

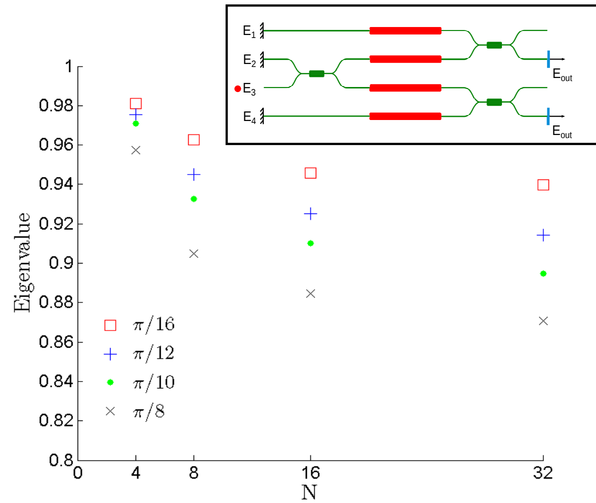

Figure 2.5: Dependence of eigenvalues on phase variation $\Delta\Phi$ and total beam number N in the zigzag array structure. phase_noise.eps

The schematic plot for $N = 4$ is shown in the inset of Fig. 2.5 for reference. If R is set to be 0.99 and the phase change in all the laser beams is the same, the non-zero eigenvalues

and the corresponding eigenvectors are shown as follows:

$$\begin{aligned} X_a &= 0.99, \quad |\boldsymbol{E}_a| = [0.5, 0.7071, 0, 0.5] \\ X_b &= 0.495, \quad |\boldsymbol{E}_b| = [0.5, 0, 0.7071, 0.5] \end{aligned} \tag{2.5}$$

The four elements in the eigenvector correspond to the electric field amplitudes of the four channels at the position 1 shown in Fig. 2.4(a). It is worth noting that in the second eigenmode, the constructive interference occurs at the port (marked by a red dot in the inset of Fig. 2.5) where there is no feedback. The loss of power at that port is the reason why X_b is a half of X_a. The current array design only provides 3dB modal discrimination. In order to increase the array modal discrimination, a short length of gain medium can be introduced right ahead of the middle(fixing) mirror at the left end. Due to this additional gain, modes with the constructive interference at the port with feedback, like X_a are preferable, whereas modes like X_b are suppressed with the enhanced modal discrimination. When the number of emitters (N) becomes larger, take $N = 16$ for example, there are eight super-modes with nonzero eigenvalues and the modal discrimination becomes smaller as shown in Eq. 2.6. However, only the mode with the lowest modal loss has the constructive interferences at all feedback ports. In the other super-modes, there are always destructive interferences at some of the feedback ports. Therefore, the additional gain medium at the feedback ports can enhance the modal discrimination to make our proposed structure able to operate at a

single super-mode with the lowest modal loss.

$$
X = \begin{bmatrix} 0.99 \\ 0.952 \\ 0.845 \\ 0.684 \\ 0.495 \\ 0.306 \\ 0.145 \\ 0.038 \end{bmatrix}, |E| = \begin{bmatrix}
0.25 & 0.354 & 0 & 0.354 & 0 & 0.354 & 0 & 0.354 & 0 & 0.354 & 0 & 0.354 & 0 & 0.354 & 0 & 0.25 \\
0.354 & 0.462 & 0 & 0.354 & 0 & 0.191 & 0 & 0 & 0 & 0.191 & 0 & 0.354 & 0 & 0.462 & 0 & 0.354 \\
0.354 & 0.354 & 0 & 0 & 0 & 0.354 & 0 & 0.5 & 0 & 0.354 & 0 & 0 & 0 & 0.354 & 0 & 0.354 \\
0.354 & 0.191 & 0 & 0.354 & 0 & 0.462 & 0 & 0 & 0 & 0.462 & 0 & 0.354 & 0 & 0.191 & 0 & 0.354 \\
0.354 & 0 & 0 & 0.5 & 0 & 0 & 0 & 0.5 & 0 & 0 & 0 & 0.5 & 0 & 0 & 0 & 0.354 \\
0.354 & 0.191 & 0 & 0.354 & 0 & 0.462 & 0 & 0 & 0 & 0.462 & 0 & 0.354 & 0 & 0.191 & 0 & 0.354 \\
0.354 & 0.354 & 0 & 0 & 0 & 0.354 & 0 & 0.5 & 0 & 0.354 & 0 & 0 & 0 & 0.354 & 0 & 0.354 \\
0.354 & 0.462 & 0 & 0.354 & 0 & 0.191 & 0 & 0 & 0 & 0.191 & 0 & 0.354 & 0 & 0.462 & 0 & 0.354
\end{bmatrix} \tag{2.6}
$$

Actually, the phase change for the light propagating within different beams denoted by S will not be identical due to the variation of individual cavity length and the refractive index. To take this variation into consideration, we introduce an independent random phase variation $\Delta\phi_j$ to each gain channel. The phase variation is modeled as a zero mean uniform distribution $U(-\Delta\phi, \Delta\phi)$, where $\Delta\phi(> 0)$ presents the strength of phase variation. Through calculating the eigenvalues and eigenvectors, the dependence of the modal gain of the preferred super-mode on the phase variation $\Delta\phi_j$ and total beam number N, can be determined, as shown in Fig. 2.5. Here, the modal gain decreases as both the phase variation and N increase. Besides the decrease of modal gain, the phase variation will also change the power distribution at the output ports, since the zigzag array structure has multiple output ports. As an example we refer to, let $N = 4$. Without the phase variation, the powers at the output ports are $|BSA \times \boldsymbol{E}|^2 = [0, 0.5, 0, 0.5]$. Under the influence of the phase variation $\Delta\phi = \pi/4$, however, the power distribution becomes [0,0.4992,0.5008,0] and this situation will become worse when either the phase variation or the number of emitters further increases. Generally, uneven power distribution at the near field will degrade both the far-field pattern and the brightness.

2.2.2 Scalability analysis

The modal analysis above shows that our proposed zigzag array structure can support several super-modes, only one of which exhibits the highest modal gain with good modal discrimination. Therefore, it is reasonable to assume that the whole system operates at a single super-mode. Since different longitudinal modes are spatially coherent, we further assume that the array operates at a single wavelength, thusly making it possible to estimate the scalability of the proposed structure from the perspective of brightness which can be defined as

$$B = \frac{P}{A\Omega} \tag{2.7}$$

where P is the total optical power, A is the emitter area and Ω is the solid emission angle [79]. Let B_0 be the brightness of one single emitter in the array,

$$B_0 = \frac{P_0}{A_0\Omega_0} \tag{2.8}$$

Thus, the ratio B to B_0 shows the improvement of brightness after combining,

$$\frac{B}{B_0} = \frac{P}{P_0}\frac{A_0\Omega_0}{A\Omega} \tag{2.9}$$

Since the solid angle Ω can be expressed as follows:

$$\Omega = \frac{S}{r^2} \approx \frac{\pi r\theta_x r\theta_y}{r^2} = \pi\theta_x\theta_y \tag{2.10}$$

where S is the area of the observation plane, r is the distance between the light source and the observation plane, θ_x is the divergence angle along the slow axis and θ_y is the divergence angle along the fast axis. For simplicity, the filling factor is assumed to be 1. Since the beam

is almost diffraction limited along the fast axis(y direction), we have $\theta_{y,0} = \theta_{y,tot}$, then

$$\frac{B}{B_0} = \frac{1}{N}\frac{P}{P_0}\frac{\theta_{x,0}}{\theta_{x,tot}} \tag{2.11}$$

To evaluate the above equation, we must calculate the far field to obtain the divergence angle, using the method in Ref. [1]. Assuming that the near field distribution of one single emitter in the array, denoted by $u_0(x)$ is Gaussian shape and identical, the near field of the array can be expressed as

$$u(x) = u_0(x) \otimes \sum_{j=1}^{N} \delta(x - jd) \exp(i\phi_j) = u_0(x) \otimes g(x) \tag{2.12}$$

where $\otimes$ is the convolution operator, d is the period of emitters and ϕ_j is the random phase of each emitter. Then the far field of $u(x)$, denoted by $U(s_x)$ with parameters $s_x \overset{\text{def}}{=} \theta_x/\lambda$, is found by taking the Fourier transformation of $u(x)$. That is

$$U(s_x) = U_0(s_x) \sum_{j=1}^{N} \exp(2\pi i j s_x d + i\phi_j) = U_0(s_x)G(s_x) \tag{2.13}$$

Then the far-field intensity can be calculated by:

$$I(s_x) =< |U(s_x)|^2 >= |U_0(s_x)|^2 < |G(s_x)|^2 >= I_0 I_G \tag{2.14}$$

where <> is the expectation operator and I_G can be expressed as follows:

$$I_G = \sum_{j=1}^{N} \sum_{l=1}^{N} \exp(2\pi i s_x d(j - l)) < \exp(i(\phi_j - \phi_l)) > \tag{2.15}$$

Thus all the phase information is included in I_G.

In the zigzag array structure, each emitter is directly coupled with the several emitters

nearby. Here, we will only investigate two cases: the fully-correlated case and the adjacent-correlated case. In the fully-correlated case, the phase difference between any two elements obeys the same zero-mean Gaussian distribution. And in the adjacent-correlated case, we only require that the phase difference between the adjacent elements obeys the same zero-mean Gaussian distribution. The strength of the phase variation will be denoted by the standard deviation of the Gaussian distribution, σ_Φ. For purposes of comparison , the ideal exemplar with no phase noise is also calculated and studied. We have to emphasize that the fully-correlated case discussed in this paper is not attainable. While it is possible to ensure a relationship between all the elements, they are not guaranteed to obey an identical distribution. Therefore, this fully-correlated case is only a simplified and theoretical simulacrum with which we may establish the limitation of scalability.

For the ideal case:

$$I_G^{ideal} = \frac{\sin^2(\pi N s_x d)}{\sin^2(\pi s_x d)} \tag{2.16}$$

and for the fully correlated case:

$$I_G^{ful_corr} = \exp(-\frac{\delta_\phi^2}{2}) I_G^{ideal} + N(1 - \exp(-\frac{\delta_\phi^2}{2})) \tag{2.17}$$

and for the adjacent correlated case:

$$\begin{aligned} I_G^{adj_corr} =& \frac{1}{[1 - 2\alpha\cos(\beta) + \alpha^2]^2} \Big(4\alpha^2 + N(1 - \alpha^4) + 2\alpha\cos(\beta)[\alpha^2(N-1) - N - 1] \\ & + 2\alpha^{N+1}\left\{\alpha^2\cos[(N-1)\beta] - 2\alpha\cos(N\beta) + \cos[(N+1)\beta]\right\}\Big) \end{aligned} \tag{2.18}$$

where $\alpha = \exp(-\sigma_\Phi^2/2)$ and $\beta = 2\pi s_x d$. Equations 2.16, 2.17 and 2.18 can be found in Ref. [1] in details.

Figure 2.6 shows the plots of I_G^{ideal}, $I_G^{ful_corr}$,$I_G^{adj_corr}$ when $\sigma_\Phi = \pi/5$. Here, the phase noise exhibits a different impact on the far-field pattern: in the fully correlated occurrence,

only the amplitude decreases due to the phase noise, compared to the ideal occurrence. In the adjacent correlated case the amplitude is decreased and the width of the main lobe is also widened. Both effects will degrade the brightness.

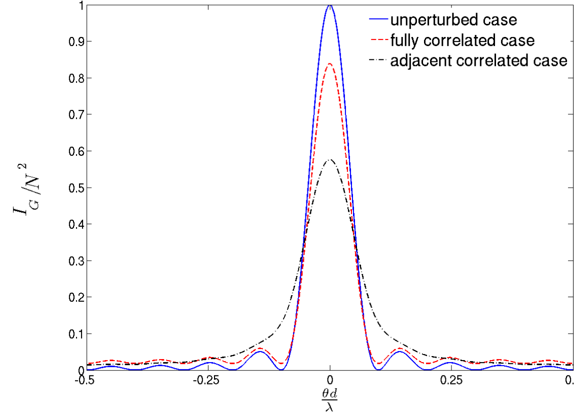

Figure 2.6: Normalized I_G vs. $\frac{\theta d}{\lambda}$. The solid line shows the ideal case. The dash line shows the fully correlated case. The dot-dash line shows the adjacent correlated case. In the simulation, σ_ϕ is set to be $\pi/5$ [1]. IG.eps

The results of B/B_0 with respect to σ_ϕ and with respect to N are shown in Fig. 2.7(a) and (b), respectively. Figure 2.7(a) shows the decrease of brightness in both fully correlated case and adjacent correlated case as σ_ϕ increases. The fully correlated case exhibits a superior performance against the phase noise than the adjacent correlated counterpart. In Fig. 2.7(b), the fully correlated exemplar exhibits a closely similar result as the ideal case. The only difference is a smaller slope due to the availability of less power (as shown in Fig. 2.6). Unlike the ideal case and fully correlated case, the adjacent correlated case exhibits a saturation behavior in brightness. When the number of elements, N exceeds a certain value, the brightness is nearly identical, allowing us to define a characteristic number by the saturation value of brightness. This number can also be regarded as the maximum number of elements that can be coherently combined. In the case shown in Fig. 2.7(b), the maximum number of elements is approximately 30.

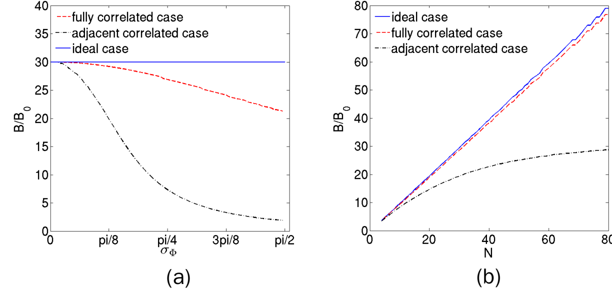

Figure 2.7: (a) Brightness with respect to the standard variation of phase noise σ_ϕ. N is set to be 30 in the calculation;(b) Brightness with respect to the number of emitters N. σ_ϕ is set to be $\pi/8$ in the calculation. The solid line shows the ideal case. The dash line shows the fully correlated case and the dot-dash line shows the adjacent correlated case. Brightness.eps

The proposed zigzag array structure should be considered as a situation between the fully correlated case and the adjacent correlated case because of the coupling mechanism explained above. Consequently, the performance of our structure should be superior to the adjacent correlated case and the scalability will be larger than the characteristic number in the adjacent correlated case. Since the evanescent-wave coupled array is more like the adjacent correlated case, our laser structure should provide better performance. Compared to the coupling mechanism of the strong spatial filtering in an external common cavity(Talbot cavity [61], self-Fourier cavity [63], etc.), however, it is difficult to determine the advantage of our construct. Specifically, although arrays with a common cavity are more analogous to the fully correlated simulacrum, the coupling strengths between any two emitters are not likely to be equal. Consequently, the common cavity is more likely to be in the same category as our laser structure, between the fully correlated case and the adjacent correlated case. We finally wish to emphasize that the brightness saturation is due to the locally phase-correlated emitters based upon our adjacent correlated assumption. Thus, it is reasonable to consider that as long as the locally phase-correlated assumption (not necessarily the adjacent correlated assumption) holds, brightness saturation behaviour will occur.

In term of experimental realization, we can pattern some single-mode ridge waveguides and 2X2 couplers by E-beam lithography and dry etch them in semiconductor wafers. The fabrication process will be similar to that of Y-junction laser arrays, but with a different coupler design. Ion implantation can be used at one port of the 2X2 couplers to eliminate the optical gain. The challenge lies in the selective facet coating to produce different reflectivity at two ports of the coupler.

2.3 Grating design

We have used two epitaxy wafer designs for demonstration of our laser diodes. One is InGaAsP/InP multiple-quantum-well wafer design which is mainly used with surface etched gratins. The other one is InGaAs/GaAs single quantum well wafer design which is used with regrowth gratings. All the epitaxy layers were grown by 3rd part foundry services.

2.3.1 Surface ethced gratings

Table. 2.1 shows the detail description on each epitaxy layer in the InGaAsP/InP wafer design. All the InGaAsP layers are InP lattice-matched. The center wavelength of photoluminescence is set at 1550nm. The fundamental slab waveguide mode is shown in Fig. 2.8 and the effective refractive index of the fundamental mode(n_{eff}) is 3.266.

To calculate the parameters of the gratings, the tilting angle should be first determined. The larger the tilting angle is, the higher modal diffraction loss is. And the modal discrimination between the first and second order Bragg modes becomes larger at a larger tilting angle. The cavity length is another consideration when to determine the tilting angle. Due to the suppression of the small modal-angle modes, the cavity length(L) should be long enough to make the two facet ends not directly meet with each other. Therefore, the minimum cavity length at a certain tilting angle can be obtained as $L_{min} = W/\tan\theta$. In our

Description	Material	Thickness (nm)	Doping	Refractive Index	x	y
Substrate	InP	n/a	$n = 2e18$	3.1720	n/a	n/a
Buffer	InP	1000	$n > 1e18$	3.1720	n/a	n/a
Waveguide	InGaAsP	130	$n = 1e17$	3.3203	0.1449	0.3167
Waveguide	InGaAsP	40	undoped	3.3203	0.1449	0.3167
Waveguide	InGaAsP	50	undoped	3.3755	0.2467	0.5353
Quantum Well	InGaAsP	8.5	undoped	3.5300	0.4402	0.9425
Barrier	InGaAsP	10	undoped	3.3755	0.2467	0.5353
Quantum Well	InGaAsP	8.5	undoped	3.5300	0.4402	0.9425
Barrier	InGaAsP	10	undoped	3.3755	0.2467	0.5353
Quantum Well	InGaAsP	8.5	undoped	3.5300	0.4402	0.9425
Barrier	InGaAsP	10	undoped	3.3755	0.2467	0.5353
Quantum Well	InGaAsP	8.5	undoped	3.5300	0.4402	0.9425
Waveguide	InGaAsP	50	undoped	3.3755	0.2467	0.5353
Waveguide	InGaAsP	40	undoped	3.3484	0.2144	0.4663
Waveguide	InGaAsP	120	$p = 1e17$	3.3484	0.2144	0.4663
Cladding	InP	1000	$p = 1e17\ 2e18$	3.1720	n/a	n/a
Contact layer	$In_{0.53}Ga_{0.47}As$	20	$p > 1e19$	3.55	n/a	n/a

Table 2.1: $In_{1-x}Ga_xAs_yP_{1-y}$/InP epitaxy wafer design

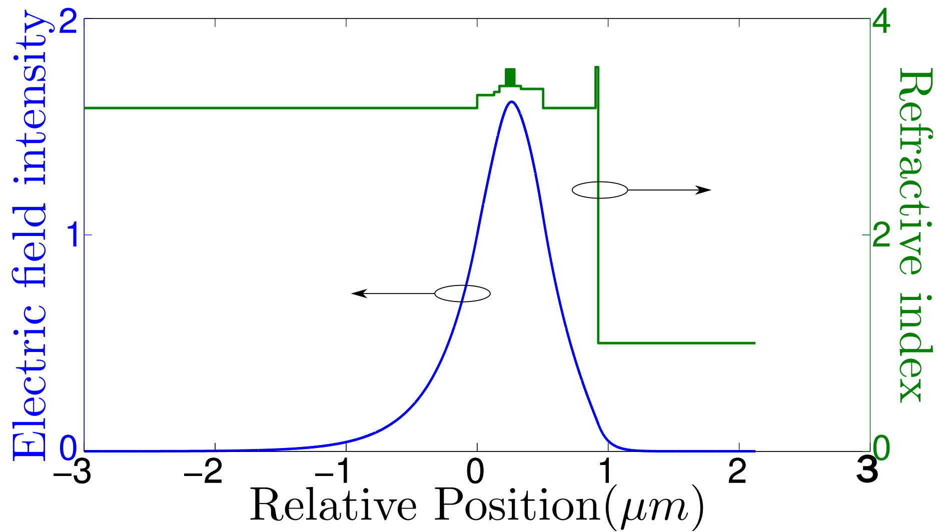

Figure 2.8: The fundamental slab waveguide mode profile and refractive index profile of the InGaAsP/InP wafer design

demonstration, the tilting angle 10° is used mainly to reduce the modal diffraction loss.

Once the tilting angle is determined, the grating period can be calculated as

$$\Lambda = \frac{\lambda}{2n_{eff}\sin\theta}$$

where n_{eff} is the effective refractive index of the epitaxy wafer. And the calculated period is $1.3663\mu m$. The etching depth is determined according to the desired coupling coefficient. The coupling coefficient of a first-order 1D square grating is defined as

$$\kappa = \Gamma\frac{2\Lambda}{\lambda^2}(n_h^2 - n_l^2)\sin(\pi D) \tag{2.19}$$

where n_h and n_l are the high and low refractive indices of the grating respectively, Γ is the confinement factor of the grating and D is the duty cycle of the grating. Γ can be related to the etch depth as

$$\Gamma = \frac{\int_0^d \varepsilon(x)|E(x)|^2 dx}{\int_{-\infty}^{\infty} \varepsilon(x)|E(x)|^2 dx} \tag{2.20}$$

where d is the etching depth and the top layer of the epitaxy wafer is aligned at $x = 0$. Figure 2.9 shows the coupling coefficient of the surface etched gratings at different etching depth in the InGaAsP/InP epitaxy wafer.

2.3.2 Regrowth gratings

Table. 2.2 shows the detail description on each epitaxy layer in the InGaAs/GaAs wafer design. There are two main reasons for changing to this new InGaAs/GaAs wafer design. One is the better material quality of GaAs material system which results in less loss and higher output power. The other one is that this InGaAs/GaAs wafer design has been reported to work well with single angled-grating broad-area lasers in a regrowth method.

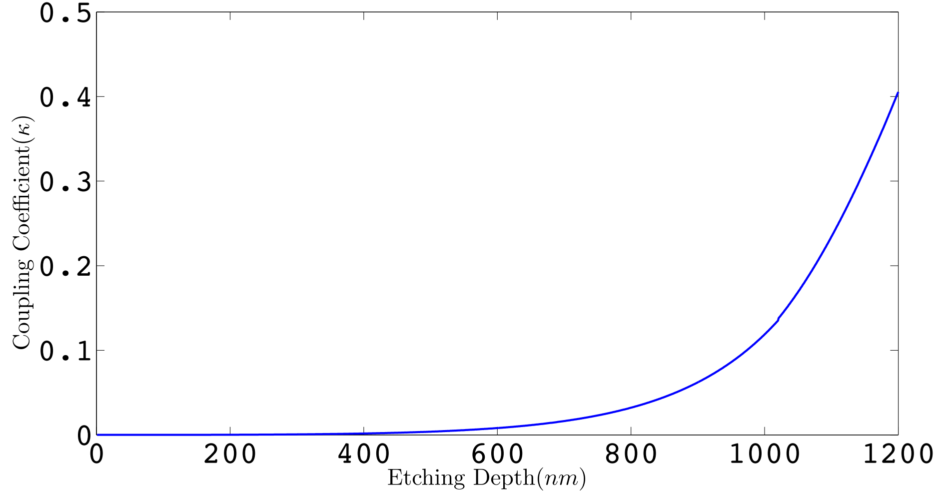

Figure 2.9: The coupling coefficient at different etching depth of the surface etched gratings in InGaAsP/InP epitaxy wafer.

Layer	Description	Material	Thickness (nm)	Dopant	Doping	Refractive Index
0	Substrate	GaAs	300	Si	$n = 2e18$	3.464
1	Cladding	$Al_{0.25}Ga_{0.75}As$	1360	Si	$n = 2e18$	3.359
2	Waveguide	GaAs	400	Si	$n = 1e17 \sim 1e18$	3.464
3	Barrier	$GaAs_{0.9}P_{0.1}$	12	undoped	na	3.45
4	Quantum Well	$In_{0.28}Ga_{0.72}As$	8	undoped	na	3.698
5	Barrier	$GaAs_{0.9}P_{0.1}$	12	undoped	na	3.45
6	Waveguide	GaAs	400	Zn	$p = 1e17 \sim 1e18$	3.464
7	Cladding	$Al_{0.25}Ga_{0.75}As$	940	Zn	$p = 2e18$	3.359
8	Contact layer	GaAs	50	Zn	$p > 2e19$	3.464

Table 2.2: InGaAs/GaAs epitaxy wafer design

The photoluminescence peak is designed at 1064*nm*. Figure. 2.10 shows the mode profile of the fundamental slab waveguide mode as well as the refractive index profile. The effective refractive index of the fundamental slab waveguide mode is 3.4011. Since this wafer design is for the regrowth gratings, there are two phases on growing this epitaxy wafer. Phase 1 growth stops after growing the layer 6, the p doped GaAs waveguide. Then the gratings are etched in this layer. After that, phase 2 growth completes the whole wafer by planarizing the etched gratings with the rest of layers.

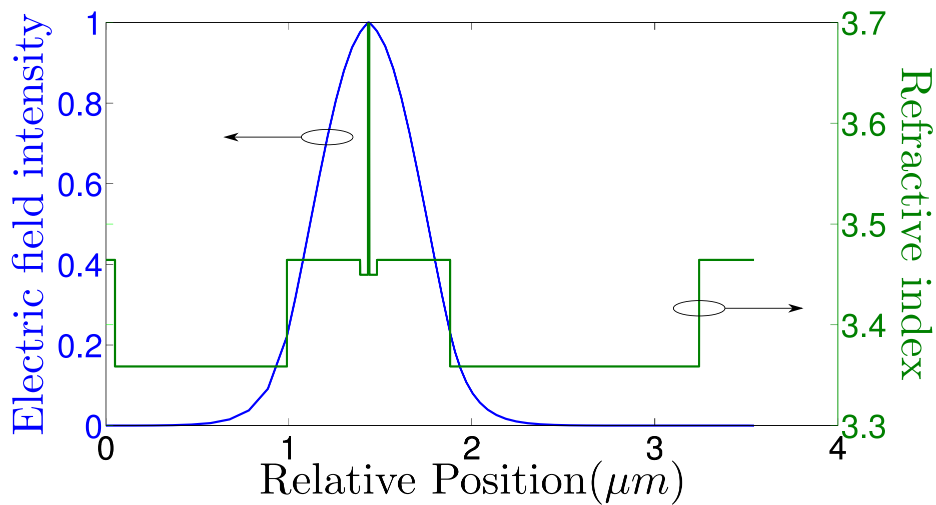

Figure 2.10: The fundamental slab waveguide mode profile and refractive index profile of the InGaAs/GaAs wafer design

Chapter 3

FABRICATION OF COHERENTLY COMBINED ANGLED-GRATING BROAD-AREA LASERS

In this chapter, I will discuss each fabrication process in details, including recipes, equipments used, process conditions and results. The immediate following part contains the discussion about surface etched gratings. The surface etched gratings are used for demonstration since it is simple and flexible enough for fabrication and design parameter optimization. In the latter part of this chapter, I will present the fabrication of regrowth gratings. Unlike the surface etched gratings, the regrowth gratings are buried in the epitaxy wafer during growth. Since the gratings are much closer to the quantum well, the etch depth can be much shallower than the surface etched gratings. The shallow regrowth gratings can be obtained by wet etching. Therefore, the sidewall can be smoother than that of the surface etched gratings. And as a result, the laser diode with regrowth gratings can suffer less loss induced by the gratings and obtain higher output power.

3.1 Surface Etched Gratings

Figure 3.1 shows schematic plots of each key step through the fabrication procedures of two coherently combined angled-grating broad-area lasers with surface etched gratings. Starting from the bare wafer, the fabrication includes SiO_2 deposition, Ebeam lithography, dry etching, planarization, metallization, ion implantation and lapping before we can cleave and package diodes for measuring. In the following sections, I will discuss each step in details including the machine and recipe used, process condition and results.

3.1.1 Deposition of SiO_2 hard mask layer

Since the etchant for etching InP/GaAs based compound semiconductor is usually chlorine-based gas or HBr in a heated up etching chamber which is around 180C, photoresist is usually carbonized in such a high temperature and not capable to be the mask layer for InP/GaAs base compound semiconductor etching. Therefore, in the bare wafer, a SiO_2 layer is first deposited as the mask layer in the following dry etchings. Two main methods can be used for SiO_2 deposition, one is LPCVD (thermal oxide) and the other one is PECVD (PECVD oxide). The thermal oxide usually requires high reactive temperature ($> 1000°C$) which will likely destroy the quantum wells. Therefore, we will go with PECVD oxide for the deposition. Considering the depth that we are going to etch in the wafer and the thickness of the ebeam resist, the thickness of the SiO_2 layer is chosen to be $300nm$. The STS PECVD 2 is used with the recipe as shown in Table 3.1. Usually the recipe will run for 2 minutes for chamber conditioning with nothing in chamber, and then run for 5 minutes with a silicon sample. The deposited SiO_2 in the silicon sample will be measured in Nanospec profilometer for the thickness to calibrate the deposition rate. It is usually around $400A/min$. Then the real sample will be inserted in for a amount of time of deposition based on the calibrated deposition rate. A simple and quick way to determine

the thickness of SiO_2 is based on the color of SiO_2 film. Different thickness of SiO_2 films reflect different colors. It is dark blue in a 300*nm* thick SiO_2 film and yellow in a 200*nm* thick SiO_2 film.

PECVD Oxide Recipe
Pressure: 650mT
Temperature: Platen 300°C, Showerhead 200°C
Gas: N_2O 1420sccm, 2%SiH_4 400sccm
13.56MHz RF Power: 25W

Table 3.1: PECVD oxide recipe in STS PECVD 2

3.1.2 Ebeam Lithography

Our grating design shows that the feature size of the one dimension gratings is around half micron and it becomes even smaller at the two dimension region. Such small feature size requires deep UV photolithograhy and elaborate calibration for fairly good results. Therefore we choose ebeam lithography which is capable to resolve several hundred nanometer lines quite easily. We spin a layer of ZEP 520A, a positive ebeam resist on the deposited SiO_2 layer using the recipe shown in Tab 3.2. The spinned resist thickness is around 360*nm* on small pieces (around $1cm \times 1cm$). It should be noticed that different sample size may result in different resist thickness even using the same recipe. The resist thickness is chosen based on the SiO_2 layer thickness to be etched and the selectivity of the SiO_2 etch recipe. The recipe we use is shown in Tab 3.4. It has a selectivity (resist over SiO_2) of around 2.

ZEP 520A Spinning Recipe
Speed: 4000rpm
Acceleration: 2000rpm/s
Duration:60s
Soft bake: 180°C on hotplate for 2mins

Table 3.2: Ebeam resist spinning recipe

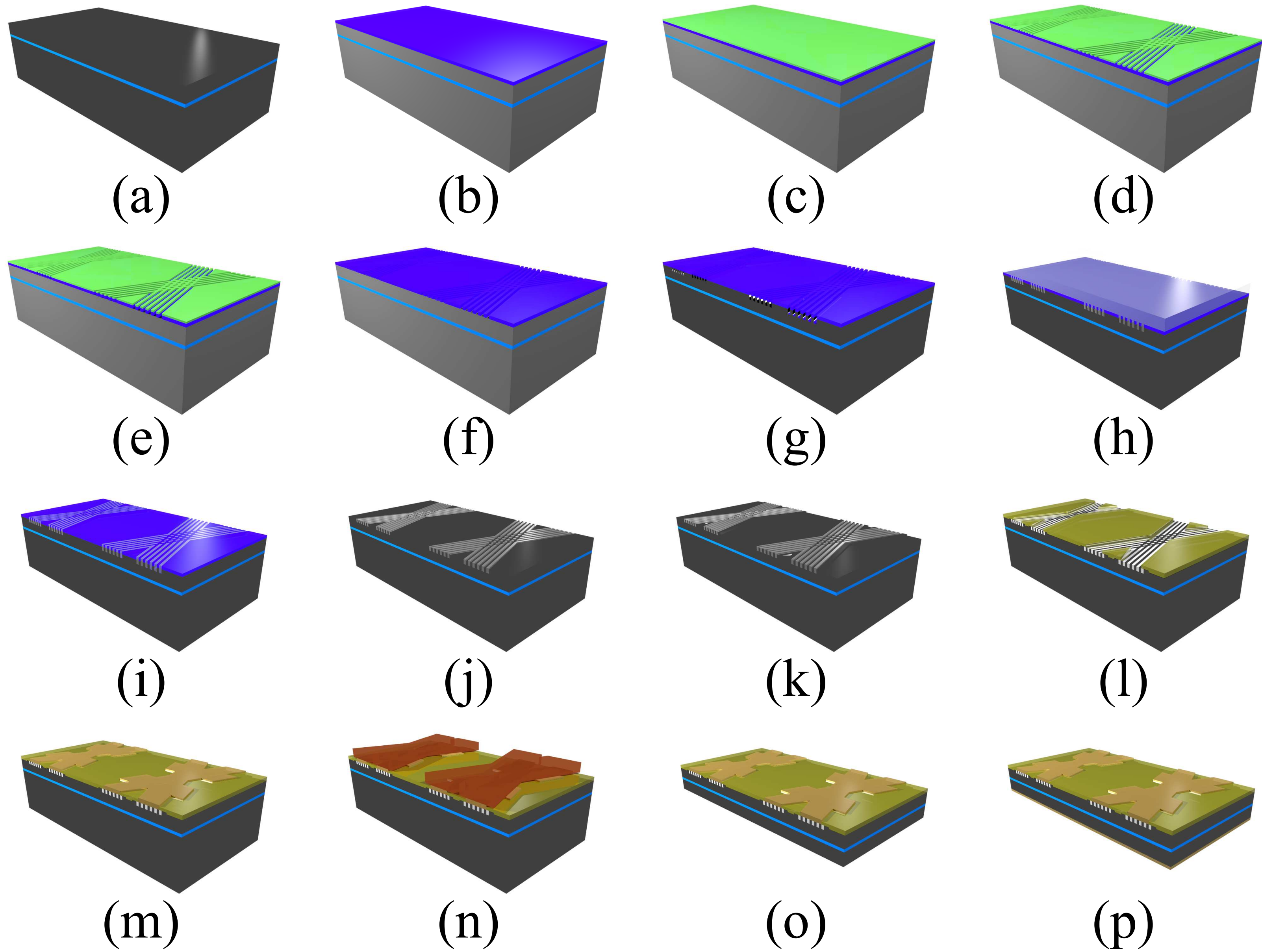

Figure 3.1: Overview of the fabrication procedures of two coherently combined angled-grating broad-area lases with surface etched gratings

Since the patterns are 50% duty cycle gratings, PEC(Proximity Effect Correction) is necessary to obtain clear patterns with right dose in all parts of patterns. The dose correction is calculated based on the back scattering electron simulation. Therefore, once the layer material, thickness or structure is changed, it is better to rerun the simulation for correct PEC.

After exposure, the patterns can be developed by following the procedure listed in Tab 3.3. The SEM picture of the developed grating pattern is shown in Fig. 3.3. No post-exposure bake or hard bake is necessary for developing or dry etching. The hard bake can be used for resist reflow if the smoothness of resist is really critical. However, the resist reflow can also alter the profile of the developed pattern as shown in Fig 3.2. We don't use the resist reflow process due to the repeatability issue.

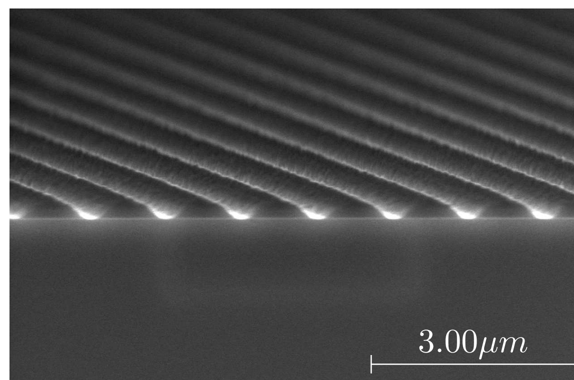

Figure 3.2: SEM picture of the resist after the reflow process.

ZEP 520A developing recipe
Developer: Amyl Acetate Duration: 2mins Soak in IPA for 30s and then N_2 blow dry

Table 3.3: ZEP 520A developing recipe

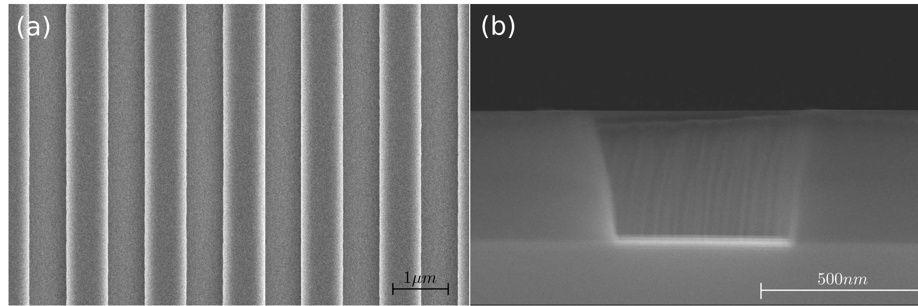

Figure 3.3: Top view (a) and cross section view (b) of the ebeam resist after development.

3.1.3 SiO_2 Dry Etch

With the ebeam resist as the mask, the grating patterns are transferred to the SiO_2 layer using ICP dry etch. The machine used is Plasma Thermal ICP and the recipe is shown in Tab. 3.4. The tool is designed to process full 4 inch wafer. Therefore, we need to fix our piece samples on a Si carrier wafer with cool grease which also has a good thermal conductivity between sample and carrier wafer. It is noticed that different carrier wafers may result in different DC biases and slightly different etching rates and selectivity. For the best repeatability, it is best to always use the same carrier wafer and recheck the etch results once a new carrier wafer is used. The SEM picture after SiO_2 dry etch is shown in Fig. 3.4. Before proceeding to the III-V dry etch, the rest of the ebeam resist should be removed first. It can be done by soaking samples in 1165 for about 10 hours and then in a ultrasonic bath. The power of ultrasonic should be chosen carefully in case it may damage the delicate grating structure.

Oxide etching recipe in Plasma Thermal ICP
Pressure: 5mT
RIE Power: 40W
ICP Power: 800W
Gas: Ar 5sccm, C_4F_8 15sccm, CO_2 28sccm

Table 3.4: SiO_2 dry etch recipe in Plasma Thermal ICP

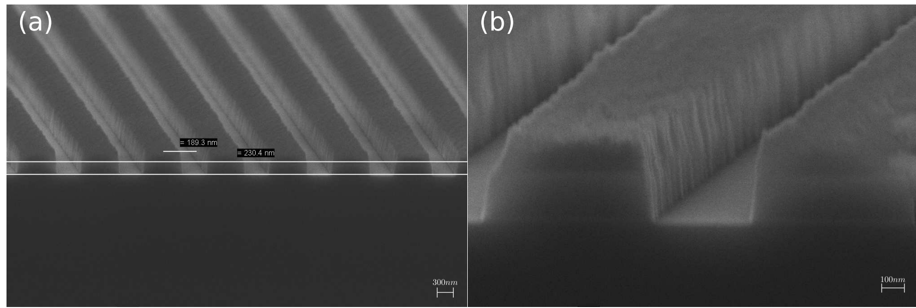

Figure 3.4: Cross section view of devices after SiO_2 layer dry etched.

3.1.4 III-V Dry Etch

Till now, we have obtained a patterned SiO_2 hard mask as shown in Fig. 3.1(f) and have been ready for the next step, the III-V dry etch. The material going to be etched is the compound semiconductor of In,Ga,As,P with different element ratios on either InP or GaAs substrate. The tool used is STS SOE and the recipe is shown in Tab. 3.5. The advantage of the etchant HBr is that it can attack all the III-V layers at a similar rate and has a fairly high selectivity of 5~10. However there might be some undercut as shown in Fig. 3.5. The STS SOE, same as the Plasma Thermal ICP is designed to process 4 inch wafers. A Si carrier wafer is still needed for our piece samples. Besides all the issues related to the repeatability, it is reported that the Si carrier wafer may help to reduce the undercut and keep a straight sidewall profile due to a thin deposition of Si on the sidewall.

III-V etching recipe in STS SOE
Pressure: 5mT
RIE Power: 40W
ICP Power: 800W
Gas: HBr 10sccm

Table 3.5: III-V(InP/GaAs) dry etch recipe in STS SOE

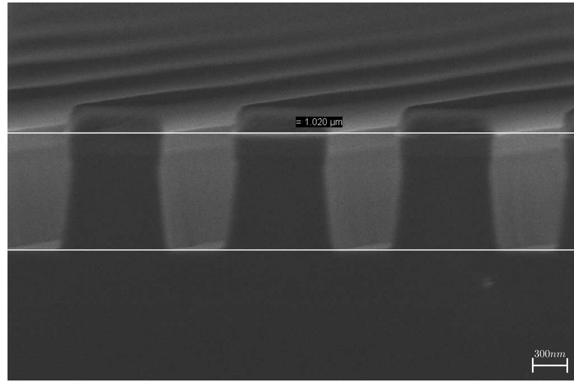

Figure 3.5: Cross section view of the device after III-V dry etch.

3.1.5 BCB Etch Back

Now, we have transferred the gratings into the III-V wafer. Before we can deposit the metal contact, the etched trenches should be filled up to prevent the metal contact from falling into the trenches and causing high loss. Therefore, after the III-V etching, we spin a layer of BCB to planarize the etched gratings. The spin coating recipe is shown in Tab. 3.6. After spinning, the BCB layer need to be fully cured in a vacuumed oven with a temperature profile as described in Tab. 3.7. The oven should be kept vacuumed during the whole cure process until the temperature goes back below 100°C. The temperature must be below 100°C before taking out the samples otherwise it is very likely that the BCB layer will peel off. Figure 3.6 shows the cross section view after BCB cure.

BCB spin coating recipe
Chemical: AP3000, adhesive promoter Speed: 3000rpm Acceleration: 1500rpm/s Duration:30s
Chemical: Cyclotine BCB 3022-46 Speed: 2500rpm Acceleration: 2s Duration:45s

Table 3.6: BCB spin coating recipe

Then we need to etch the BCB layer back to the position close to the top surface of

BCB cure temperature setting
Ramp to 100°C in 15 mins
Hold at 100°C for 15 mins
Ramp to 150°C in 15 mins
Hold at 150°C for 15 mins
Ramp to 250°C in 60 mins
Hold at 250°C for 60 mins
Cool down below 100°C

Table 3.7: BCB temperature profile for cure

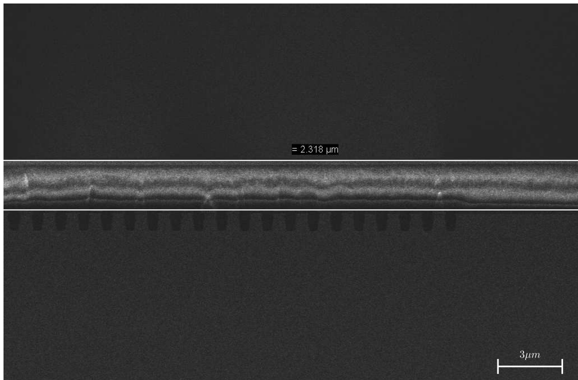

Figure 3.6: Cross section view of BCB planarization after BCB layer is completely cured.

the wafer. This is the most tricky part in the fabrication processes. With the SiO_2 layer as a buffer layer, it is feasible using the ICP dry etch. The etch recipe is shown in Tab. 3.8. The etching process can be monitored under SEM to make sure it is at the right position. Figure 3.7 shows the top view of the planarized gratings after BCB etch back.

BCB etch back recipe
Pressure: 8mT
RIE Power: 75W
ICP Power: 250W
Gas: CF_4: 9sccm, O_2: 21sccm

Table 3.8: BCB etch back recipe in Plasma Thermal ICP

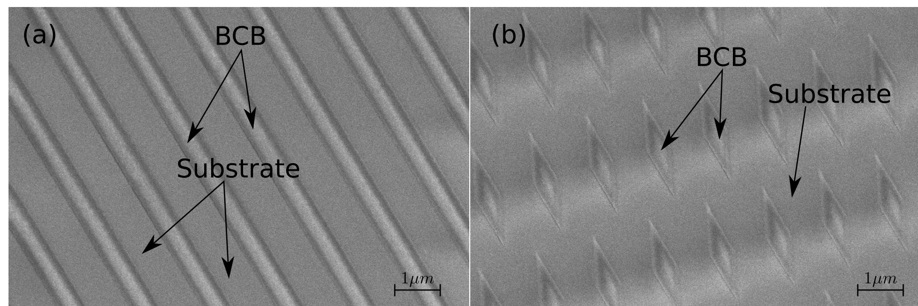

Figure 3.7: SEM pictures of devices after the step of BCB etch back. (a) the 1D grating area; (b) 2D overlapped area.

3.1.6 P-Contact Deposition

Now, we have already obtained a surface etched and planarized grating in the wafer. Next step, we need to make the p metal contact. Before the deposition of the metal contact, there is still a layer of SiO_2 needed to be removed. And this can be done in buffered oxide etcher as shown in Fig. 3.1(j). In Fig. 3.1(l), a new SiO_2 layer is deposited in STS PECVD 2 using the recipe in Tab. 3.1. The new SiO_2 layer is about 200*nm* and is used as an insulation layer. The device window is opened using standard photolithography and BOE wet etching. There will be another run of photolithography to define the device window

with bonding pads for the lift-off process following the metal contact deposition. The Denton Explorer ebeam evaporator is used to deposit p metal contact. The composite of contact is Ti/Pt/Au($28nm/100nm/300nm$) counting from the wafer. The Ti/Pt/Au metal contact can be used as p-type ohmic metal contact in both InP and GaAs wafer due to the tunneling effect of the thin, heavily doped p contact layer in the wafer. After deposition, the extra metal contact can be lifted off by soaking in acetone. If the photolithography works well, the extra metal contact may peel off itself due to the high strain of metal contact. If not, a low power ultrasonic bath may help the lift-off process. Figure 3.8 shows the cross section view of the gratings after p-contact deposition.

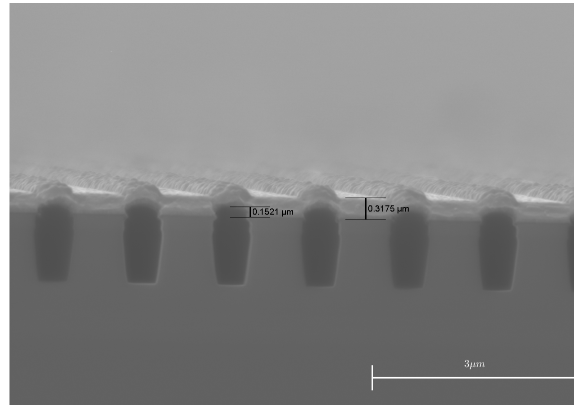

Figure 3.8: Cross section view of the device after depositing P metal contact.

3.1.7 Ion Implantation

There are two main purposes to introduce the ion implantation to our fabrication process. One is to confine the injected current within the device area for electrical insulation, the other one is to obtain uniform current distribution to improve the laser output beam quality. There will be detail analysis and discussion in the characterization section. We don't have the facility for ion implantation. Therefore, our samples are sent out to a 3rd part manufacturer for this process. The recipe we used is shown in Tab. 3.9. Only the area other than the

metal contacts is implanted and the devices under metal contacts are protected by a thick layer of photoresist as shown in Fig. 3.1(n). After developing, the photoresist should be hard baked for better protection.

Ion implantation recipe for InP wafer
Spices: H^+ Energy: $260KeV$ Dose: 5×10^{14}

Table 3.9: Ion implantation recipe for InP wafer

3.1.8 Lapping

When the samples are shipped back, the photoresist mask should be removed first. Since the photoresist has already been hard baked, it may take some time to soak samples in 1165 or acetone before it can be removed. We can still use ultrasonic bath for a little help. The thickness of the wafer we use is from $350\mu m$ to $600\mu m$. Since the optical mode is confined within only tens of μm, the extra substrate has no help with the optical confinement but to increase the electrical resistance. Therefore, the final device will be lapped to around $100\mu m$. The lapping process is done by a manual lapping tool from the back side (n-type substrate). Samples are mounted by wax on a fixture and are lapped on a glass plate with $8\mu m$ diameter SiC abrasive powder. After lapped, the samples can be soaked in ultrasonic bath while still being waxed on fixture to shake off the extra SiC powder attached to the samples. This can help improve the adhesion of n-contact. Samples can be released from the fixture by soaking in acetone. This may take up several hours to resolve the wax in acetone. After lapping, the samples are extremely fragile. So try to push gently without breaking the samples.

3.1.9 N-Contact Deposition

Now, samples are ready for the n-contact deposition. In the InP substrate, we can still use Ti/Pt/Au($28nm/100nm/300nm$) as the n metal contact. Therefore, we can use the same tool and recipe as the p-type metal contact deposition described above. Figure 3.1(p) shows the schematic plot of a completed sample after n metal contact deposition.

3.1.10 Packaging

Till now, we have already had the gratings for mode control, metal contact for current injection. The only thing that is still missing is the facet to define the resonant cavity. The cleaved crystal face can be used as the laser facet. In the edge mode, the scriber only scribes part of the sample from the edge and leaves the devices untouched. Then the impulse bar makes the sample break along the scribed line to obtain a laser bar. It is then scribed through along the direction perpendicular to the facet to separate each device. Figure 3.9 shows a schematic plot of the cleavage process.

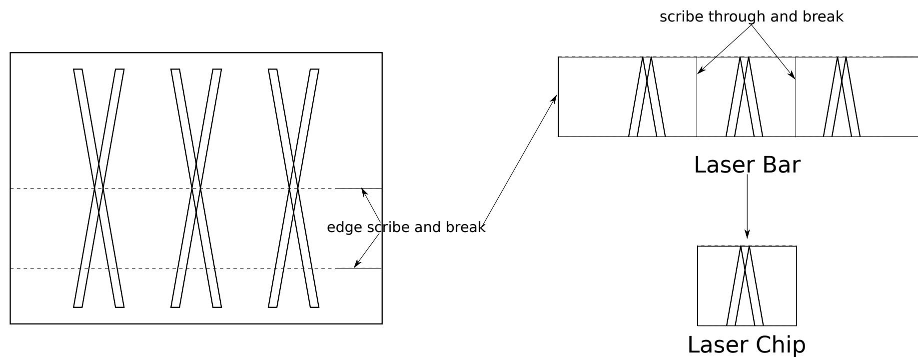

Figure 3.9: Schematic plot of the cleavage process: from die to separate laser diode.

After that, we have completed the fabrication of the laser diodes theoretically. However, the small die is too hard to handle and measure. Therefore, we need to package the laser diode. First, we will do die bonding to bond the laser diode onto a c-mount. Besides to make it easy to handle, it also provides a heat sink to the laser diode. There are two kinds

of die bonding, p-side up and p-side down bonding. In the p-side up bonding, the n-side of the laser diode is bonded to the c-mount while in the p-side down bonding, the p-side is directly bonded to the c-mount. The advantage of the p-side down bonding is obvious, which is that bringing the heat source closer to the heat sink can help the heat dissipation. However, because the quantum well is very close to the melting solder in the p-side down bonding, it is very easy to get laser facet contaminated. Besides, since we scribe through the laser bar to separate the laser diodes, the insulation SiO_2 is damaged along the edges other than the facets. Therefore, we need to apply other insulated material to the edges before we can do the p-side down bonding. Otherwise, there will be a large current leakage along the edges.

Wire bonding is needed to make electrical connection after the die bonding. In the p-side up bonding, wires are bonded on the bonding pads not directly on the devices. The wire bonding is done in the wire bonder(K&S 4526 wedge bonder) with 1mil diameter gold wire. The packaged device that is ready for the following measurement is shown in Fig. 3.10.

3.2 Regrowth Gratings

Figure 3.11 shows schematic plots of each key step through the fabrication procedures of coherently combined angled-grating broad-area lasers with regrowth gratings. The fabrication processes are very similar to those of surface etched gratings described previously, only simpler. The wafer we start from is not a complete grown epi wafer. It is only grown to the p-side waveguide layer. And we need to fabricate the gratings in the waveguide layer and then send it back to the foundry service to grow the rest layers in the wafer structures. In the following sections, I will discuss in detail the steps that are different from the surface etched gratings.

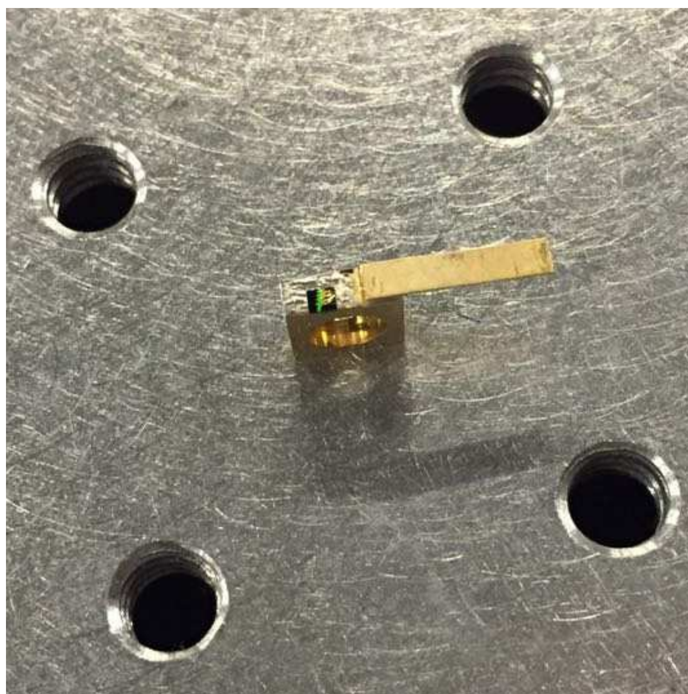

Figure 3.10: The image of the packaged device.

3.2.1 Deposition of SiO_2 mask layer

In the surface etched grating fabrication, the first layer of SiO_2 is used as the hard mask for dry etching III-V material because photoresist is carbonized in the high temperature chamber during dry etching. In the regrowth grating fabrication, the gratings are wet etched. The reason for still choosing SiO_2 as the mask layer other than photoresist is that the grating pitch is too small that photoresist may lose the adhesion during wet etching. Since the etchant for wet etching barely attacks the SiO_2, we do not need a thick SiO_2 layer. The thickness is chosen to be $100nm$. We use the same tool and recipe described in Tab. 3.1.

3.2.2 Ebeam lithography

We use the same patterns as in the surface etched gratings. There is some slight difference. After regrowth, the patterns will be completely planarized. But we need some alignment

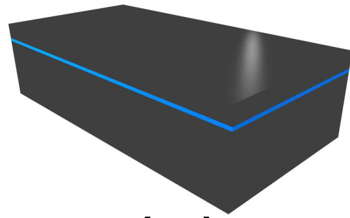
(a)

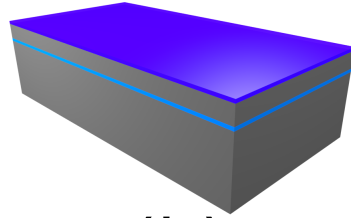
(b)

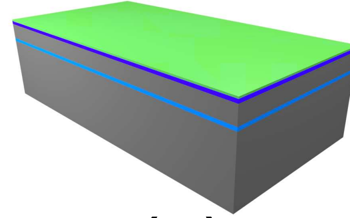
(c)

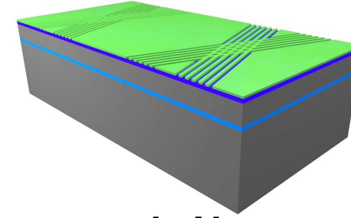
(d)

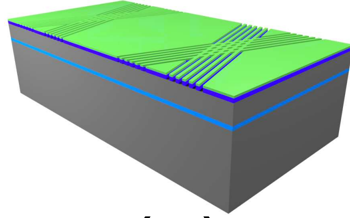
(e)

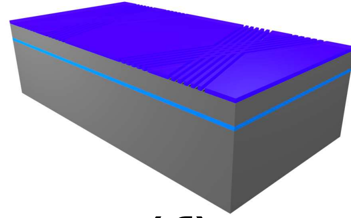
(f)

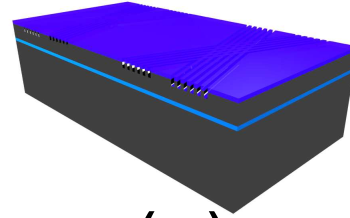
(g)

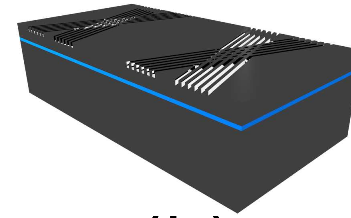
(h)

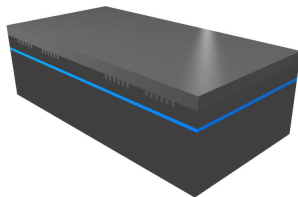
(i)

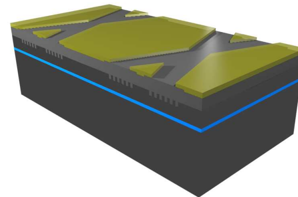
(j)

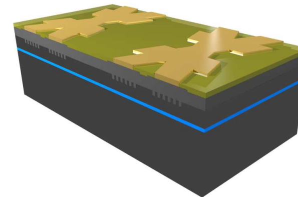
(k)

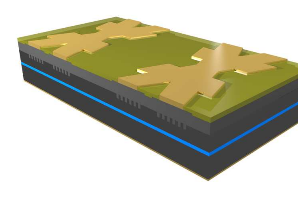
(l)

Figure 3.11: Overview of the fabrication procedures of two coherently combined angled-grating broad-area lases with regrowth gratings

marks for metal contact deposition. Therefore, we will do twice ebeam lithography. The first time just writes the alignment marks which will be etched deep enough to be seen after regrowth. The second time writes the actual grating patterns. We will use the same recipe described in previous section.

One notice here is that since we are going to wet etch the gratings, the etching profile is isotropic, which means the trench becomes wider when going deeper. Therefore, the exposed area is pre-biased a little smaller taking the expansion into consideration.

3.2.3 SiO_2 dry etch

With the ebeam resist as the mask, the grating patterns are transferred to the SiO_2 layer using ICP dry etch, the same as what we did in the surface etched gratings. The same tool and recipe can be used and the only difference is the thickness of SiO_2 layer which may result in different processing time. Before proceeding to the following wet etch, the rest of the ebeam resist should be removed first. It can be done by soaking samples in 1165 for about 10 hours and then in a ultrasonic bath. The power of ultrasonic should be chosen carefully in case it may damage the delicate grating structure.

3.2.4 GaAs wet etch

In the regrowth grating fabrication, we choose wet etch to transfer the patterns into GaAs waveguide layer, because the grating is pretty shallow and wet etch can avoid the bombardment damage in the dry etch. The etchant is H_2SO_4:H_2O_2:$H_2O$$(1 : 1 : 10)$. The etch rate is pretty fast compared to the target depth and it may vary a little at different temperature or after different shelf time. Therefore, it is best to wait for the solution to cool down after pouring H_2SO_4 into H_2O. Also it is much better to calibrate the etch rate every time right before etching the real samples. The wet etching recipe is shown in Tab. 3.10. Figure 3.12

shows the cross section view after GaAs wet etching.

GaAs wet etching recipe
H_2SO_4(96%):H_2O_2(30%):H_2O = 1:1:10

Table 3.10: GaAs wet etching recipe

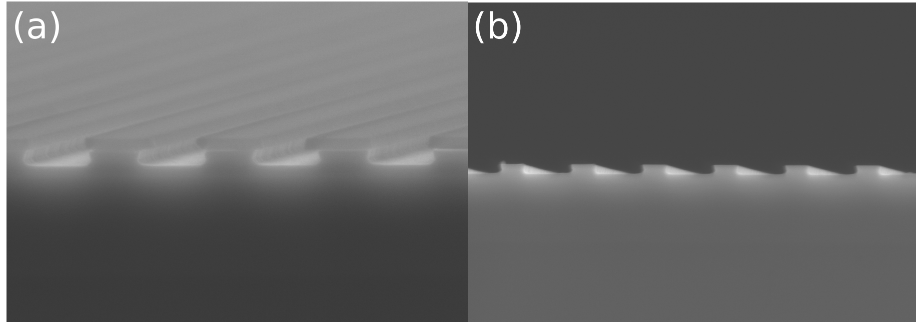

Figure 3.12: Cross section view of the wet etched gratings (a) with SiO2etch mask (b) after removing the etch mask.

3.2.5 P-contact deposition

Before we can do the p metal deposition, the SiO_2 mask layer should be removed first in BOE and then the samples should be sent out to the foundry service to planarize the gratings by the rest of wafer structure, cladding and contact layers. Since the alignment marks have been etched deeply enough, they can be visually seen under the mask aligner. The photolithography and lift-off process are the same as in the surface etched gratings. Figure 3.11(k) shows the schematic plot of the device after p-contact deposition.

3.2.6 Ion Implantation

Ion implantation is also used to confine the current distribution in the regrowth grating fabrication. The procedure is the same. The only difference is the recipe which is shown in Tab. 3.11. It has a lower energy but higher dose.

Ion implantation recipe for GaAs wafer
Spices: H^+
Energy: $250KeV$
Dose: 1×10^{15}

Table 3.11: Ion implantation recipe for GaAs wafer

3.2.7 N-Contact Deposition

The lapping process is the same as described in surface etched grating fabrication. The final thickness of regrowth sample is also around $100\mu m$. For n-contact deposition, we will use Ni/AuGe/Au(5/100/150nm) to obtain ohmic contact. The AuGe alloy consists of 88% Au and 12% Ge in weight. The deposition is done in the PVD filament evaporator. Figure 3.11(l) shows the schematic plot of a completed sample after n metal contact deposition. Then the samples will be cleaved to individual devices and packaged through die bonding and wire bonding for measurement.The process afterwards should be the same as described in the surface etched grating fabrication. Please refer to the section 3.1.10 for details.

Chapter 4

CHARACTERIZATION OF COHERENTLY COMBINED ANGLED-GRATING BROAD-AREA LASERS

In this chapter, the measurement setups for characterzing laser diodes are first described. Then the measurement results of several different laser designs are also shown and discussed. These results include the L-I curve, near field, far field and optical spectrum. The far field measurement results of the coherently combined angled-grating broad-area lasers show single lobe, high contrast interferece patterns with near-diffraction-limited beam quality. It is also shown in this chapter that the ion implantation is helpful to obtain uniform current distribution and single modal operation. The results with and without ion implantation are presented and compared.

4.1 Measurement setup

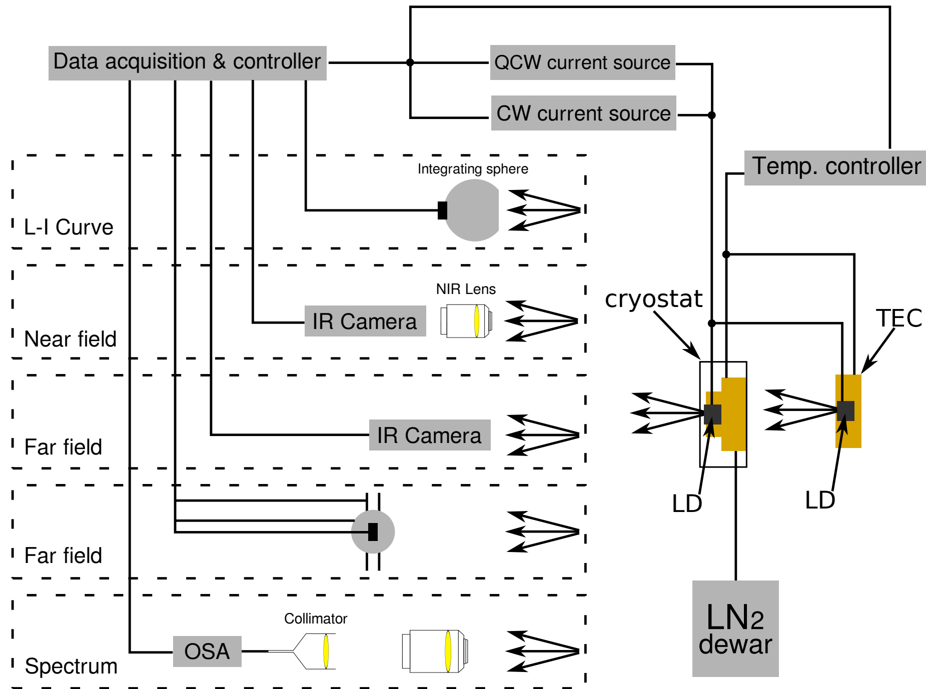

Figure 4.1: Schematic plot of the measurement setup for L-I curve, near field, far field and optical spectrum.

Figure 6.4 shows the measurement setups for characterizing the laser diodes. The laser diode can be mounted either in a cryostat for low temperature measurement or on a TEC(Thermal Electric Cooler) for room temperature measurement. Liquid nitrogen is used along with the heater controlled by the temperature controller to maintain the temperature in the cryostat. The main purpose of measuring in low temperature is to reduce the intrinsic loss of the laser diodes. Either CW or QCW current source can be used to pump our laser diodes as shown in Fig. 6.4.

4.1.1 L-I curve

For L-I curve measurement, the laser output power is collected by an integrating sphere. The advantage of using integrating sphere is that the collection efficiency is insensitive to the laser beam quality. The integrating sphere we use is calibrated to have a 30dB attenuation in the reading of the connected power meter. Considering that only one side output power is collected, the total output power in CW measurement can be calculated as:

$$P_{tot} = 2 \times 1000 \times P_{read} \tag{4.1}$$

where P_{read} is the reading value from the power meter.

In the QCW measurement, the output power is still collected by the integrating sphere. Due to the slow sampling rate of the power meter compared to the current pulse width, we use an oscilloscope to collect the analog signal directly from the power head. The collected analog signal can be converted to the output power. Figure. 4.2 shows the collected signal for example.

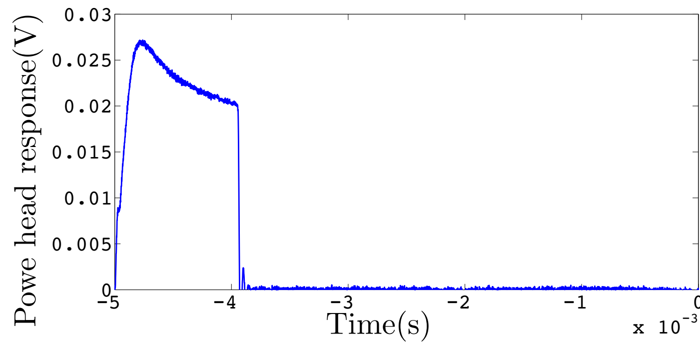

Figure 4.2: The optical power head response of the laser output in one period of QCW measurement.

Then the output power can be calculated as:

$$P_{tot} = 2 \times 1000 \times \frac{G}{D}\frac{1}{T}\int_0^T V(t)dt \tag{4.2}$$

where $V(t)$ is the collected analog signal, T is the period of pulse train, D is the duty cycle of the pulse and G is the coefficient to convert the voltage signal to power. G can be found in the manual of the power meter.

4.1.2 Near Field

We take the image of the laser output facet as the near field measurement result. This can be obtained by a simple optical imaging system. As shown in Fig. 6.4, the laser facet is imaged by a NIR lens and the image is captured by an IR camera.

4.1.3 Far Field

We have two setups for measuring the far field results. One is as simple as using only an IR camera. The IR camera is placed several centimeters away from the laser diode. The image obtained from the IR camera is the far field image and can be converted to angular distribution according to the distance between the laser diode and the camera. This simple setup is just for quick check. The resolution of the IR camera is not adequate to resolve the interference fringes. Therefore, another setup is used for high-precision far field profile measurement. A detail schematic plot of the measurement setup is shown in Fig. 4.3.

In this setup, there are two linear stages, one is for x direction movement and the other one is for y direction movement. On top the 2D stage is a rotation stage and a power head is placed at the center of the rotation stage. In order to obtain the high precision far field profile, the position of the laser diode relative to the power head is required. If the far field is assumed to be near diffraction limited, we can scan the far field profile at two different x positions (pos 1 and pos 2 shown in Fig. 4.3). The distance between this two positions in x direction is Δx. The widths of the far field profile at the two positions are D_1 and D_2, respectively. Then the distance between the laser diode and the power head in x direction,

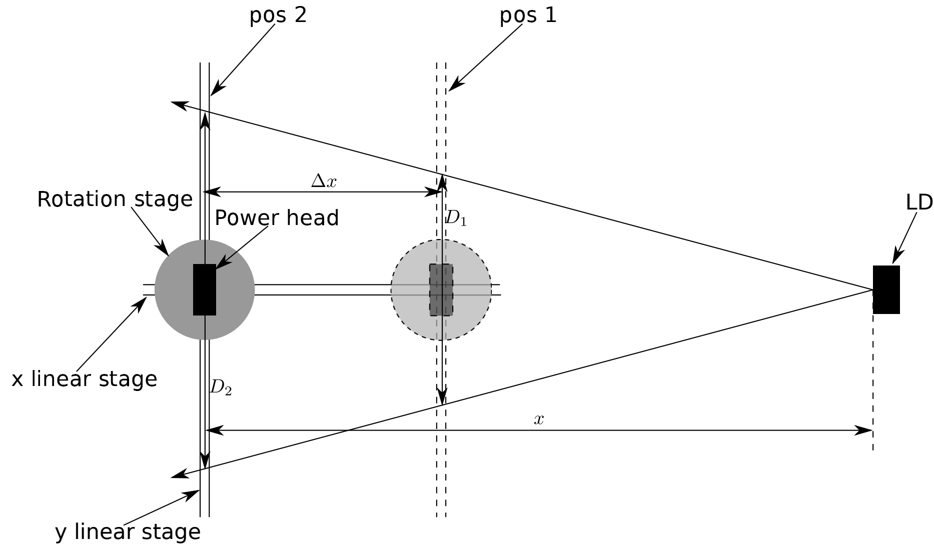

Figure 4.3: Schematic plot of the far field profile scanning setup.

x can be obtained by

$$\frac{D_1}{D_2} = \frac{x - \Delta x}{x} \tag{4.3}$$

Once the relative position of the laser diode is obtained, the power head can move along the y linear stage to scan the far field profile. In order to obtain the highest power at each position, the power head should be rotated to be perpendicular to the laser output. The rotation angle can be calculated as

$$\theta = \arctan\left(\frac{y_1 - y_0}{x_1 - x_0}\right) \tag{4.4}$$

where (x_0, y_0) is the position of power head and (x_1, y_1) is the position of the laser diode. The angular resolution of this setup is about $\frac{l}{x}$ where l is the sensor size in the power head. Therefore, the resolution can be easily improved by just increasing x.

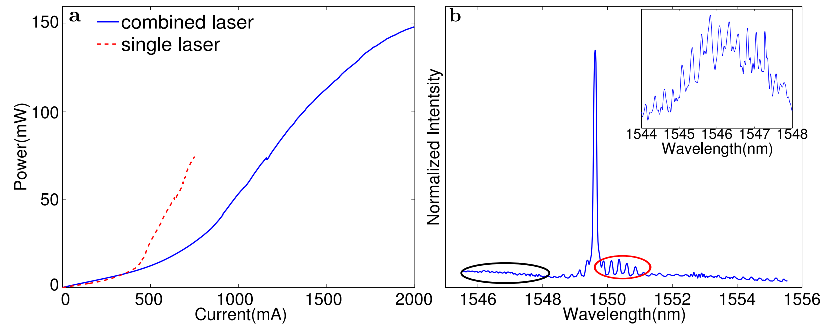

Figure 4.4: Measurements of the light-current curve and optical spectrum. (a) L-I curves of the combined angled-grating laser (solid line) and the single emitter (dashed line). (b) Spectrum of the combined laser diode when the injection current is 1200mA. The inset is a zoomed-in spectrum in the black circle.

4.1.4 Optical Spectrum

In order to obtain the optical spectrum of laser diodes, the output light is first collimated by a NIR objective lens and then collected and focused onto a multimode optical fiber. The optical fiber is then connected to an optical spectral analyzer to obtain the optical spectrum.

4.2 Results of two coherently combined angled-grating broad-area lasers

The measurement results of the L-I curve, spectrum, near field and far field shown in this section are obtained in a cryostat system with the heat sink temperature set at 230K. In all the measurements, the lasers are electrically pumped in CW operation.

4.2.1 L-I curve and optical spectrum

Figure 4.11(a) shows the light-current curve of the combined angled-grating laser. The threshold current is around 700mA and the slope efficiency is about 0.12W/A. The relatively low slope efficiency indicates high optical loss in the cavity which is mainly caused

by the roughness of the gratings induced during the dry etching process. As for the power combining efficiency, ideally, the output power of a coupled emitter should be twice output power of a single emitter when the injected current is doubled. However, thermal effects are more serious in the combined laser due to nearly doubled heat load. When the thermal effect is not obvious, for example at 1.2A, the output power of the coupled emitter is 78.57 mW. The output power of the single emitter is 44.74 mW at 0.6A. Thus the corresponding power combining efficiency is about 0.9. Figure 4.11(b) shows the optical spectrum of the same laser diode. The pump current is 1200*mA* which is about $1.7I_{th}$. The peak wavelength is 1549.62*nm* close to the designed grating resonance wavelength. The inset shows a zoomed-in spectrum from 1544*nm* to 1548*nm* indicating a free spectrum range (FSR) of 0.22*nm*, in agreement with the cavity length of 1.3*mm*. The FSR suggests that the longitudinal modes are defined by two end facets. Longitudinal mode competition is observed around the peaks in the red circle due to the small modal gain difference between the adjacent longitudinal modes [43].

4.2.2 Near field and far field

Figure 4.5(a) and (b) show the near-field image and profile of the combined angled-grating laser. It is clear that there are two emitting regions along the facet. The difference between the intensities of the two regions comes from the nonuniformity in the wafer and induced by the fabrication processes. The distance between the two emitting regions (368μm) and the emitting width of each region (106μm) indicates that light indeed emits from the designed angled-grating areas. The area between two emitters is illuminated a little bit due to the current leakage. The far field of the same coupled laser is shown in Fig. 4.5(c) and (d). We compare the far field profile of the combined laser with an uncoupled single emitter. If two coupled emitters are coherently combined and in-phase, they will constructively interfere

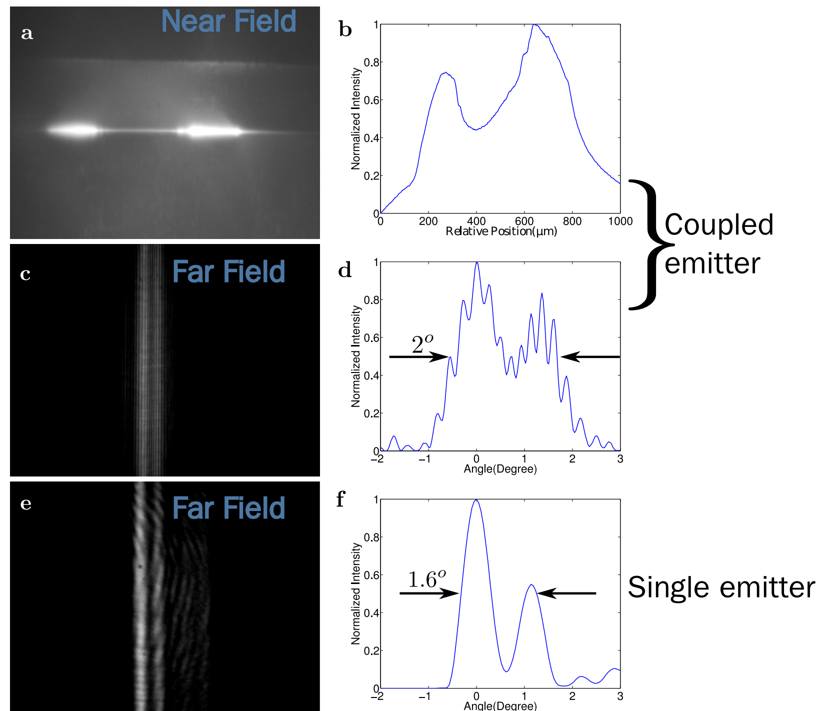

Figure 4.5: Measurements of the near field and far field of the coupled emitter and single emitter. (a, b) The near field image and profile of the coupled emitter; (c, d) The far field image and profile of the coupled emitter; (e, f) The far field image and profile of a single emitter.

in the far field and the overall envelop of the interfered far field remains the same as that of a single emitter. The only difference is that within the overall envelop, interference patterns present. This is exactly our measurement results, as shown in Fig. 4.5 (c-f). The uncoupled single emitter was fabricated on the same chip with the combined laser. The grating parameters such as the period, duty cycle, and total width are also the same. It is clear that the overall envelop of the combined laser's far field is very similar to that of the uncoupled single emitter. The fine interference patterns in Fig. 4.5(c) and (d) prove that two emitters are coherently combined. The FWHM divergence angles (1.6°for the single emitter and 2°for the combined laser) of these two lasers are still much smaller than a conventional broad-area laser ($\sim$ 10°). The difference in the divergence angles between the single emitter and coupled emitters are mainly due to different near-field distribution

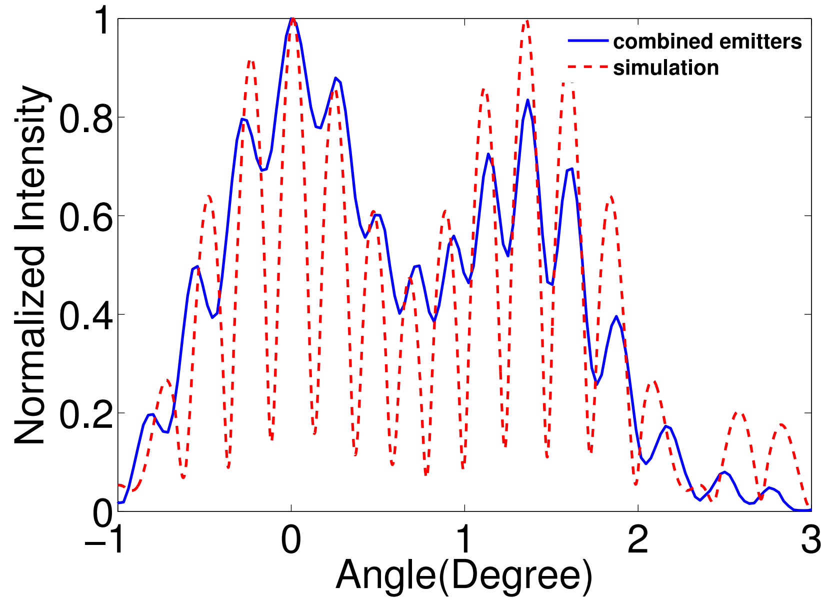

Figure 4.6: Far-field profiles of the coherently combined laser and simulation result. Solid line presents the measurement result of the coherently combined laser and the dashed line is the simulation result.

induced by the non-uniformity of fabrication and current injection.

We extracted the distance between two emitters and the width of one emitter from the measured near-field in Fig. 4.5(a). We assumed that the two emitters were in phase and calculated the far-field pattern by use of the standard diffraction theory. The calculation result is shown in Fig. 4.6 in the red dashed line and agrees well with the measured result. The angular distance between two interference stripes in the measurement result is 0.246°and it is 0.234°in the calculation. Steady interference patterns are observed when we increase the pump current up to $2A$, which proves that the combining approach is still effective under a high pump condition.

The distinction of the fringes shown in Fig. 4.6 is low for a few possible reasons. One is the uneven outputs from two beams as shown in Fig. 4.5(b). Multiple longitudinal modes observed in the spectrum also reduce the visibility of the fringes due to the incoherent addition of different sets of interference patterns with different spacing of fringes. Another

important reason is the strong background noise in the infrared vidicon camera we used.

4.2.3 Improve Beam Quality by Ion Implantation

In the previous sections, there is an overall double-lobe envelope in the far field results. Further investigation shows that the double lobe envelope comes from the second order Bragg mode, which is excited by the nonuniform current/gain distribution due to the lateral current leakage. In this section, ion implantation is used to confine the current within the grating area so that the fundamental Bragg mode will be the preferred lasing mode. The simulation results, as well as the measurement results are also presented to show the improvement of beam quality after ion implantation.

Simulation results

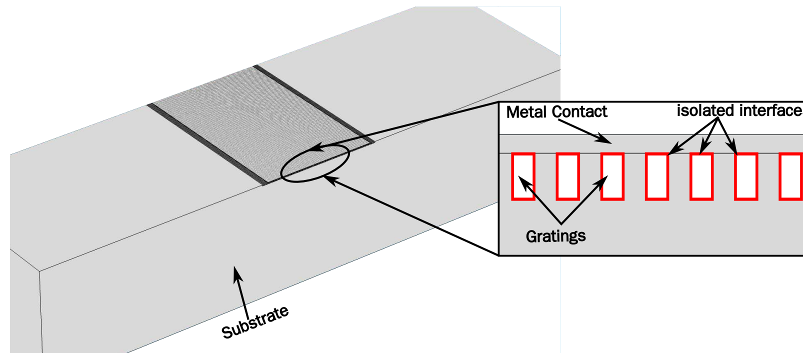

Figure 4.7: Simulation geometry in COMSOL®. The inset is a zoom-in view around the metal contact. The isolated interfaces are marked in red.

The planarization material, BCB, is an electrical isolator. Therefore, the effective resistance of the grating area under the metal contact is larger than that of the p-type highly doped area outside the gratings. As a result, the injected current will concentrate at the edges of the grating area. We carried out a 3D current distribution simulation in COMSOL® for a single emitter. The simulation geometry is shown in Fig. 4.7. In the simulation model,

a grating structure is set on the surface of substrate. All the interfaces contacting with BCB are set to be electrically isolated and all the other materials are set to have the same electrical conductivity for simplicity. A gold plate is placed right on the top of the gratings as the metal contact. A current source is set on it. Figure 4.8(a) shows the top view of the current density at the position of the quantum well region. The result shows a nonuniform current

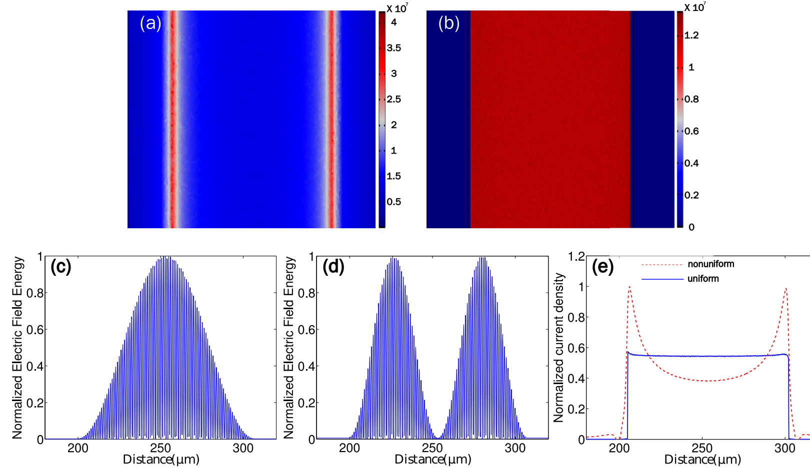

Figure 4.8: Simulation results of the injected current distribution. (a) Nonuniform current distribution without ion-implantation. (b) The distribution becomes more uniform after increasing the resistance outside the grating area.(c) and (d) Electric fields of the first and second order Bragg modes, respectively. (e) Normalized line current density corresponding to (a) in dashed red line and (b) in solid blue line.

distribution with less current at the center and more current at the edges. We can calculate the modal gain of the first two Bragg modes and show that with such a nonuniform current distribution, the modal gain of the second order Bragg mode is actually larger than that of the fundamental mode. We first calculate the model profiles of the first and second order Bragg modes by using the transfer matrix method [45]. They are shown in Fig. 4.8(c) and (d), respectively. If we denote the modal gain as g_m, it should satisfy:

$$\int \mathbb{E}(x) e^{2g(x)\Delta z} dx = \left(\int \mathbb{E}(x) dx \right) e^{2g_m \Delta z} \tag{4.5}$$

where $\mathbb{E}(x)$ is the electrical field energy and $g(x)$ is the material gain.

Therefore, the modal gain can be defined as:

$$g_m = \lim_{\Delta z \to 0} \frac{\ln(\int \mathbb{E}(x) e^{2g(x)\Delta z} dx) - \ln(\int \mathbb{E}(x) dx)}{2\Delta z} = \frac{\int \mathbb{E}(x) g(x) dx}{\int \mathbb{E}(x) dx} \tag{4.6}$$

In the region around threshold, the material gain can be assumed to be linearly proportional to the current density [80], therefore, we can substitute $g(x)$ in Eqn. 4.6 with $J(x)$ we obtained from the simulation. Obviously, after such substitution we can only obtain the relative modal gain of different modes, which should be adequate for comparison purpose. We also need to point out that to make a fair comparison between different current density profiles, we should use the current density profiles obtained with the same current source amplitude. Mathematically, the current density should be normalized as

$$\int J(x) dx = constant \tag{4.7}$$

where $J(x)$ is the line current density obtained from the simulation result. Figure 4.8(e) shows the normalized line current density corresponding to Fig. 4.8(a) and (b), respectively. Following the steps above, we find the normalized modal gain of the first two Bragg modes with the nonuniform current distribution to be 0.4153 and 0.4498, respectively, The second order Bragg mode has a larger modal gain than the fundamental mode, which makes it more preferable to be the lasing mode in this situation. To select the fundamental mode, a more uniform current distribution is needed. A practical method to obtain this goal is to increase the resistance of the materials outside of the grating region. Thus, the lateral current leakage is decreased and the current is confined under the metal contact. The simulation result of the current distribution in this situation is shown in Fig. 4.8(b) and the normalized modal gains of the first two Bragg modes change to be 0.5311 and 0.5, respectively. Now, with a more

uniform current density profile, the fundamental Bragg mode will be preferred as the lasing mode due to a larger modal gain. Experimentally, we can use ion implantation [81, 82] to increase the material resistance outside of the grating region. We first tested several ion implantation recipes with different ion energies in broad-area lasers. Figure 4.9 shows the near-field pictures of different recipes. The near-field images were directly measured by using a near-infrared objective lens and camera, showing the beam profile at the emitting facet. In Fig. 4.9(a), the non-implanted device shows obvious tails in the near field. As the ion energy increases, the tails of the emitting aperture become smaller which indicates less current leakage. As a result, we choose $260KeV$ proton with the dose of $5 \times 10^{14}/cm^2$ as our ion implantation recipe.

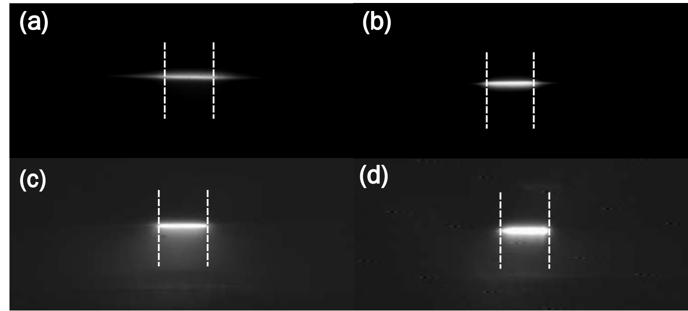

Figure 4.9: Near field images after proton implantation at different energies with the dose of $5 \times 10^{14}/cm^2$. (a) Not implanted. (b) Ion energy is $180KeV$. (c) Ion energy is $220KeV$. (d) Ion energy is $260KeV$. Between the dashed lines is the emitting aperture.

Measurement results

We measured the completed laser under CW pump condition in a cryostat with the heat sink temperature set at 230K. Figure 4.10 shows the near field and far field measurement results of our laser. In the near field shown in Fig. 4.10(a), the total width of the emitting aperture is about $160\mu m$ and the distance between the two apertures is about $425.6\mu m$. There is about 10% difference in the intensities of the two beams. These values will be used in the theoretical far-field calculation. Compared with the near field reported in Ref. [83], the

near-field profile of the ion implanted lasers has sharper edges of the emitting apertures and larger distinction ratio between the emitting area and dummy area due to better current confinement. In the far field shown in Fig. 4.10(b), an overall single lobe envelope is obtained. Multiple fringes in the far field are due to the interference of two coherently combined emitters. The full width at half maximum (FWHM) is about 1.08°. The angular distance between fringes is about 0.2073°. Compared with our previous far-field result, a much better contrast ratio of the interference fringes is obtained. The difference between peaks and valleys for our previous device is only about 0.2 and in our current device, the difference is improved to be 0.9 in the normalized scale, which indicates better coherence of the two emitters. The reason for better coherence is that after ion implantation, the first order Bragg mode becomes the dominant lasing mode and has stronger coupling efficiency.

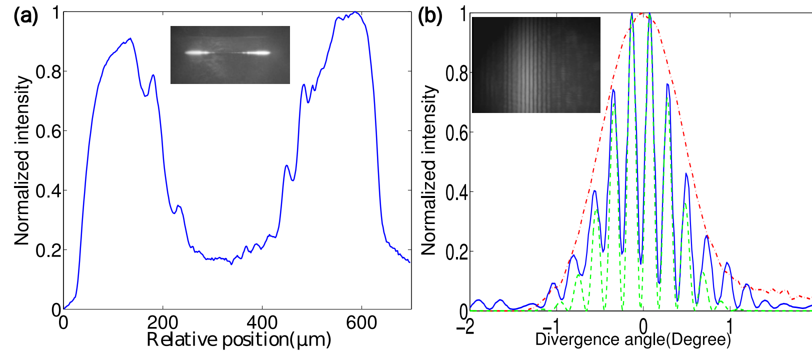

Figure 4.10: (a) Near field of the coupled laser. The inset is the camera image. (b) Far field profiles: the blue solid line is the measured far field of the coupled laser, the green dashed line is the calculated far field and the red dash-dot line represents the measured far field of a single angled-grating broad-area laser. We obtain a good agreement between the measured and calculated far field. The inset is the camera image.

We also calculate the far-field pattern by applying Fourier transform on the measured near-field profile and compare the calculated result (green dashed line) with the measured far field (blue solid line) in Fig. 4.10(b). The angular distance between fringes in the calculated result is about 0.2040°. We obtain a good agreement between the two results.

Besides, we also show the measured far field of an ion-implanted single angled-grating broad-area laser. It is presented as the red dash-dot line in Fig. 4.10(b). In Ref. [83], the divergence angle of the combined laser is slightly larger than that of the single emitter. For our current lasers, however, the envelope of the far field of the combined laser is almost the same as that of the single emitter, which also suggests better coherence.

At last, the measured L-I curve and spectra are shown in Fig. 4.11. In the L-I curve, the threshold is found to be about $555mA$ and the slope efficiency is about $0.15W/A$. The strong spontaneous emission is due to the relatively high optical loss of angled-grating cavity before the threshold. The performance is slightly better than our previous device, benefiting from better current confinement. The kinks in the L-I curve are caused by mode hopping which can be observed in the spectrum measurement shown in Fig. 4.11(b). When we increase the pump current to about $1200mA$, the peak wavelength suddenly changes from $1546.2nm$ to $1550.6nm$. The far-field profile remains the same when the mode hoping happens, so it is only the longitude mode hoping. We believe that the mode hopping is the result of longitudinal mode competition. All the near field and far field results were acquired under $1200mA$ pump current condition. When we further increase the pump current, the performance of the laser degrades due to the thermal problem.

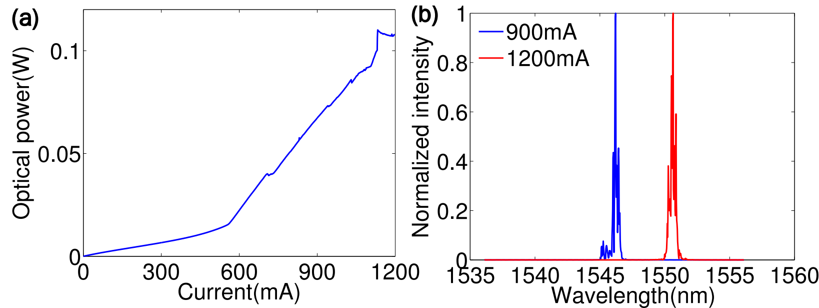

Figure 4.11: (a) L-I curve. (b) Spectra at two different pump currents.

4.2.4 P-side down bonding

In the previous sections, the thermal rollover in the LI curves indicates that the output power is limited by the thermal effect. A better thermal management would help improve the output power. Since in our epitaxy wafer design, the active region, quantum well, is located closer to the p contact, we can use p-side down bonding to bring the active region closer to the heat sink. When we first tried the p-side down bonding, the cleaved chip is directly bonded on the head sink with the flip-chip bonder. During measurement, the voltage on the laser diode becomes unstable and the laser is switched on and off from time to time, indicating that there is other current paths besides the one through the laser diode. First we thought that might be due to the extra soldier touching the laser side wall. However, after careful examination under SEM, all the laser side walls are clear without any soldier. Remembering the scribing process when we break down a laser bar to separate lasers described in Fig. 3.9, the insulation layer is actually scribed through at the laser edges. There may be some area at the edges with semiconductor exposed as shown in Fig. 4.12. Therefore, before p-side down bonding, we protect the exposed area by dip-coating some BCB at the edges of the laser diode. Figure 4.13(a) shows the LI curves of the p-side-up bonded and p-side-down bonded single angled-grating broad-area lasers. It is obvious that the p-side-down bonding laser diode has a larger slope efficiency than that of the p-side-up bonding device. The LI curves of p-side-down bonded single and two combined lasers are also shown in Fig. 4.13(b). The output power of both devices can go over $1W$ at high current without thermal rollover. The dashed line represents the twice output power of a single emitter at doubled pump current($2L_{single}$ vs. $2I_{single}$). Along all the pump currents, the LI curve of the combined laser(in red line) is very close to the dashed line, indicating almost 100% combining efficiency. With better thermal management, the two combined laser can even lase at room temperature on a TEC heat sink with quasi-CW

pumping. The LI curve in QCW measurement is shown in Fig. 4.14. The pumping pulses are $1ms$ width with 20% duty cycle. The high threshold and small slope efficiency are due to the high internal loss of the device which may be induced by the deep III-V dry etching.

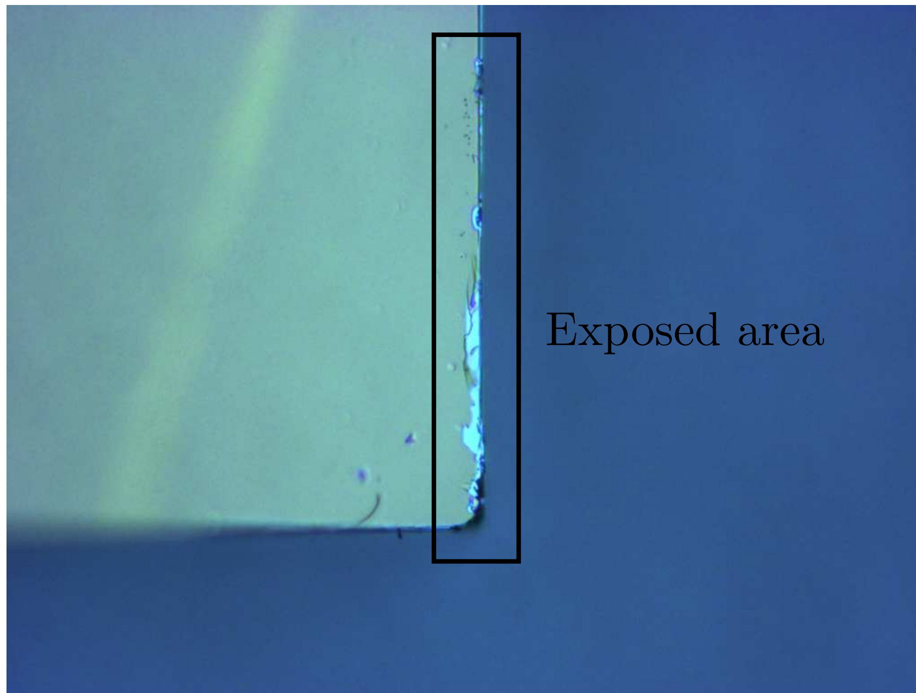

Figure 4.12: Camera image of the broken insulation layer and exposed semiconductor after scribing.

4.3 Results of six coherently combined angled-grating broad-area lasers

Figure 6.3 shows scanning electron microscopy(SEM) pictures of the completed device. We measured the light-current(L-I) curve, near field, far field and optical spectra of the mini laser bar. All the measurements are carried out with CW current source in a cryostat with the temperature set at 200K to reduce the thermal effect. Figure 4.16(a) shows the light

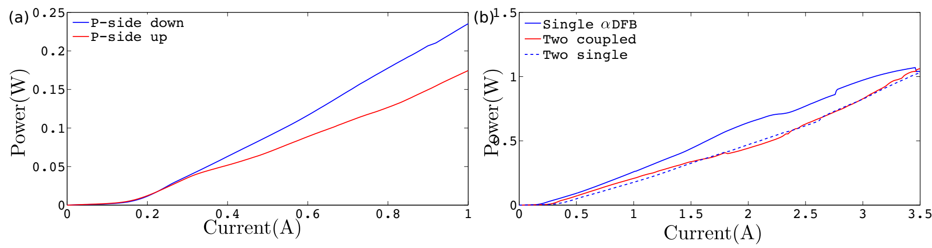

Figure 4.13: (a) LI curves of the p-side-up bonded(in red) and p-side-down bonded(in blue) single angled-grating broad-area lasers.(b) LI curves of the p-side-down bonded single angled-grating broad-area laser(in solid blue line) and two coherently combined lasers(in red line). The dashed line is the twice of the single emitter output power at doubled pump current to be compared to the combined output.

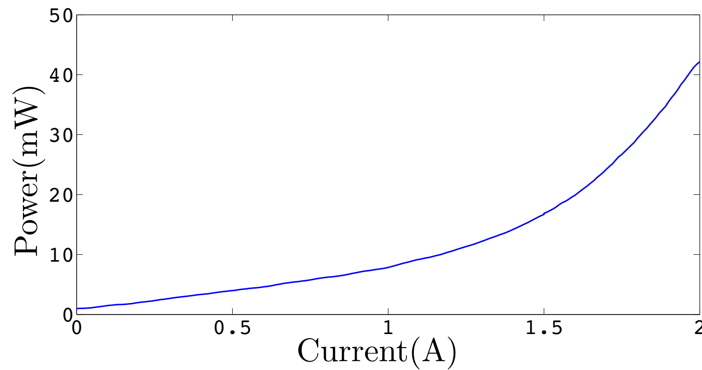

Figure 4.14: LI curve of the two combined laser with quasi-CW pumping on a TEC heat sink setted as $16°C$. The pumping pulses are $1ms$ width with 20% duty cycle.

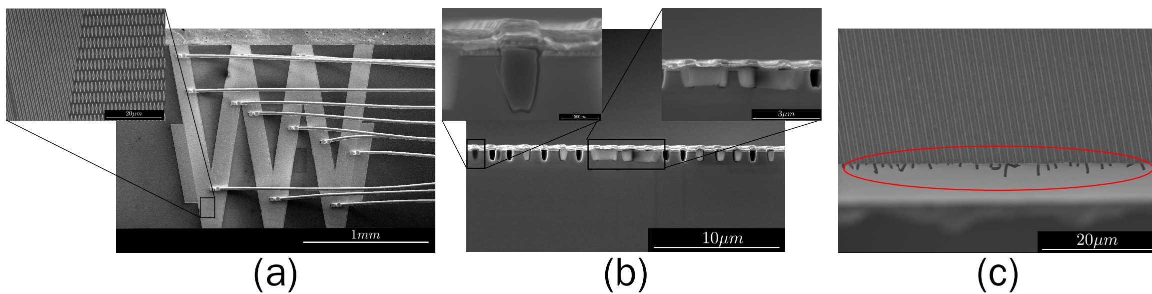

Figure 4.15: (a) Top view of a completed laser mini bar. The inset is the zoom-in view of the coupling region. (b) Cross-section of the gratings. From left to right, the insets are the zoom-in view of one tooth of the gratings and zoom-in view of the stretched-out BCB filling, respectively. (c) Top view of gratings at the facet. The stretched-out BCB fillings are shown in the red circle.

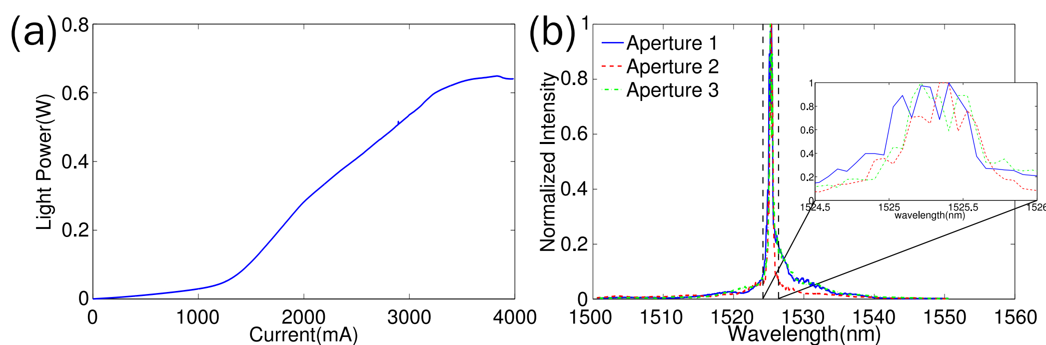

Figure 4.16: (a) Light power vs. current curve of the mini laser bar. (b) Light spectrum of three apertures at 2000mA; the inset is the zoom-in view between 1524.5nm and 1526nm.

power vs. current curve of the mini laser bar. The threshold current is about 1213.6mA. The slope efficiency is 0.362W/A near threshold and changes to 0.247W/A at around 2000mA. The slope efficiency drop is mainly due to thermal effects since we did not observe the changes in the near field and far field profiles. The maximum power reaches about 650mW which is limited by the thermal rollover. In our mini laser bar, the optical spectra of each emitting aperture are measured through the configuration shown in Fig. 4.17. The laser bar output facet is first imaged through the obj. lenses 1. An iris is placed at the image plane after the obj. lenses 1 as a spatial filter, which lets the light from one aperture pass through and blocks the light from other apertures. This setup ensures that only the light emitting from one aperture can be collimated by the obj. lenses 2 and then collected by the collimator. At last, the collected light is characterized by an optical spectrum analyzer(OSA) through a multi-mode fiber. The optical spectra of the three emitting apertures are shown in Fig. 4.16 (b). The three apertures have the same lasing wavelengths around 1525.3nm with a span of 0.4nm as shown in the inset of Fig. 4.16(b), which indicates good spectral coherence of the mini laser bar.

The fabricated mini laser bar has two output facets. One contains three apertures and each of them consists of the combination of two emitters. At the other side, the two middle apertures consist of the combined outputs and the other two aside only consist of the output

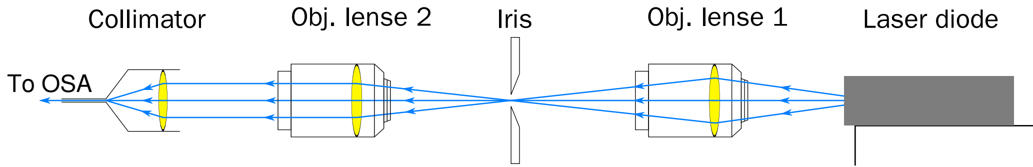

Figure 4.17: Diagram of the optical setup used to measure the optical spectrum of each aperture.

of one laser diode. Figure 4.18(a) shows the near field profile measured at the three-aperture facet. In this figure, the distances between the neighbouring apertures are very close to each other and match well with the design parameters. The similar intensities and widths of the three apertures indicate an uniform distribution of injected current. These values are denoted in this figure and used to calculate the theoretical far field profiles. In Fig. 4.18(b), we show the measured and calculated far field profiles, along with the far field profile of a single angled-grating broad-area laser. High contrast ratio interference fringes are clearly observed in this figure. The measured average angular distance between fringes

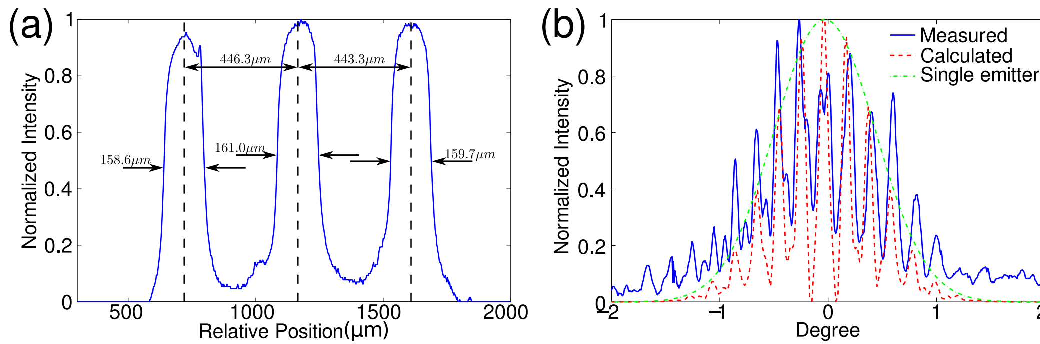

Figure 4.18: Near field and far field profiles of the three coherent output apertures of a mini-bar at 2000mA. (a) Near field profile. (b) Measured far field profile(blue solid line); calculated far field profile(red dashed line); far field profile of a single angled-grating broad-area laser(green dash-dotted line).

is about 0.2093^o which is very close to the theoretical result of 0.2077^o. The measured FWHM of the far field is about 1.5^o which is slightly larger than the calculated result of 1.1^o. All the results above demonstrate that the mini laser bar is coherently combined

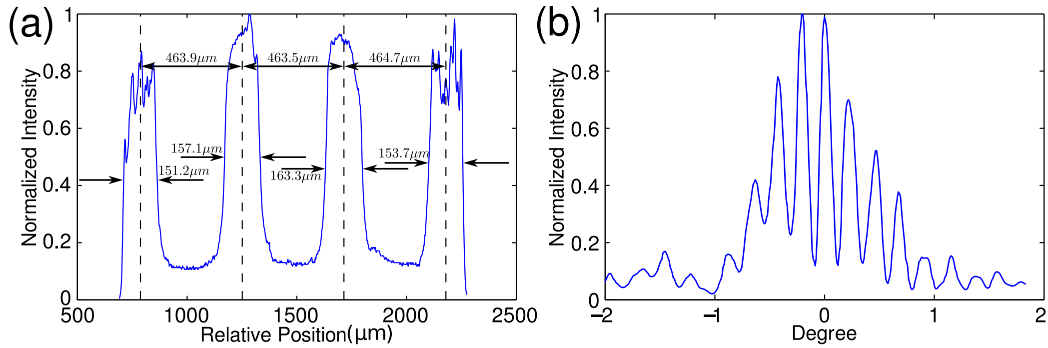

Figure 4.19: Near field and far field profiles of the four coherent output apertures of a mini-bar at 2000mA. (a) Near field profile. (b) Measured far field profile.

with near diffraction-limited beam quality. Figure 4.19 shows the near field and far field measurement results of the four-aperture side, respectively. In the near field profile, the two side apertures have slightly smaller intensities than the two middle apertures. Interference fringes are clearly observed in the far field profile as well, indicating good spatial coherence of this emitting facet. We also observe some non-uniform spikes in the near field profile of two side apertures. We consider the reason as follows. When cleaved, the polymer used for planarizing the gratings may not break uniformly along the cleavage plane of the substrate and some of them stretch out in front of the laser facet, as shown in Fig. 6.3(c). These polymer causes scattering of the output light resulting in the spikes in the near field.

4.3.1 Small modal angle modes in the combined mini bar

When we scan the far field profile of the laser mini bar in a large range, we find two side peaks at a large divergent angle as shown in Fig. 4.20. The two peaks are due to the small modal angle modes. In a single angled-grating broad-area laser, the small modal angle modes are eliminated due to the large reflection loss at the facet as described in Fig. 1.8. The large reflection loss comes from the angle mismatch which means the reflected wave can not be coupled back into the cavity. However, in a combined mini laser bar, the small modal

angle modes can be reflected to the adjacent emitter as shown in Fig. 4.21. Therefore, only the two output ports at the sides of the laser mini bar (P1 and P2 in Fig. 4.21) can help diminish the SMA modes no matter how many emitters are in the laser bar. In the two coherently combined angled-grating broad-area laser, the reflection loss is still big enough to suppress the SMA modes. That is why we didn't find the side peaks at the large divergent angle in the far field profile. While in the six combined laser mini bar, there are four more emitters in the array to provide gain and the reflection loss is not big enough any more. We can calculate the divergent angle of the SMA mode as

$$\begin{aligned} \frac{\sin\theta_t}{\sin\theta_i} &= n_{eff} \\ \therefore \theta_t &= \arcsin(n_{eff}\sin\theta_i) \end{aligned} \tag{4.8}$$

where $\theta_i = 10°$ and $n_{eff} = 3.2665$. We find the divergent angle is 34.5567° which matches the measurement result as shown in Fig. 4.21.

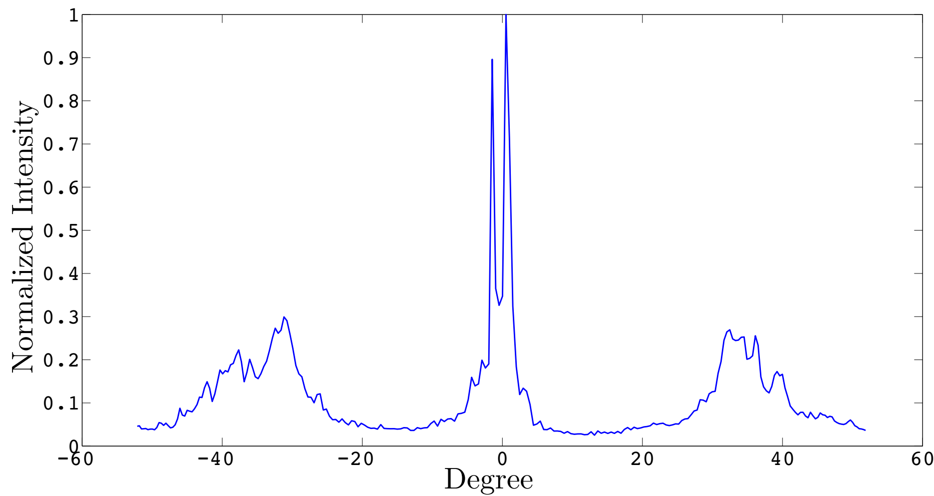

Figure 4.20: Coarse far field profile of the six combined laser mini bar in a large range of divergent angle. Two side peaks present at around 35°.

We can deposit a multiple layer facet coating to increase the reflection loss of SMA modes. Figure 4.22(a) and (b) shows the facet coating design and the reflectivity of this

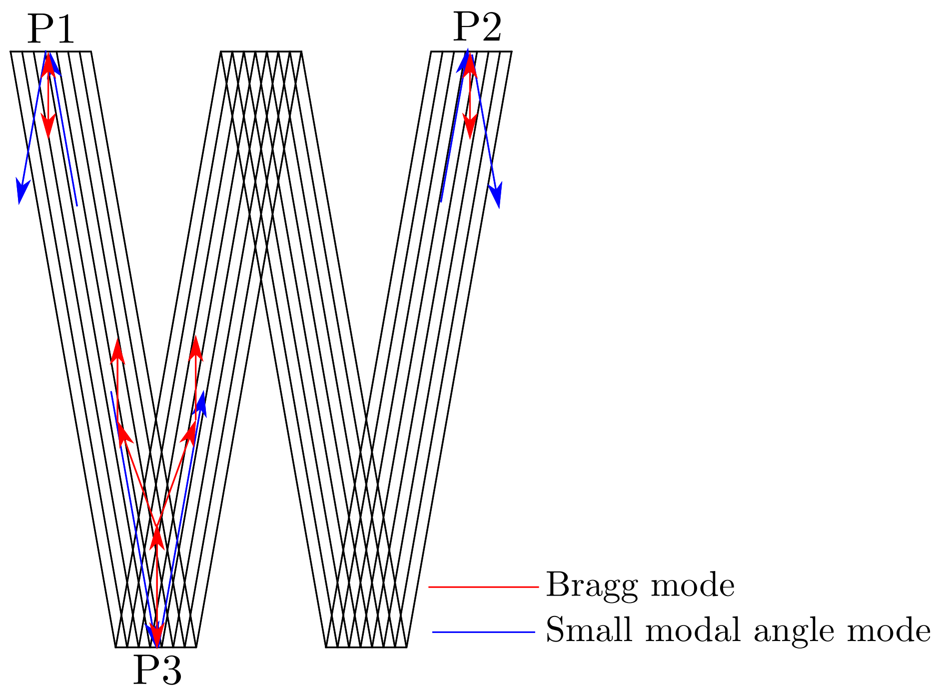

Figure 4.21: Schematic plot of the reflection of Bragg modes and small modal angle modes in the combined laser mini bar. P1, P2 and P3 are the labels of the output ports.

coating at different incident angles, respectively. The lowest reflectivity happens around 13° in this design. The refractive index of the materials are measured by an ellipsometer. However, the ebeam evaporator we used to deposit the facet coating design cannot monitor the film thickness accurately enough. Figure 4.23(a) shows the SEM picture of the deposited facet coating with noticeable thickness errors in each layer. The near field of the combined laser mini bar with the facet coating is shown in Fig. 4.23(b) and cracks can be found in the coating due to the flip chip bonding process. Therefore, some effort in the fabrication process is still needed to improve the accuracy in film thickness and the film quality to obtain the lowest reflectivity at the designed angle.

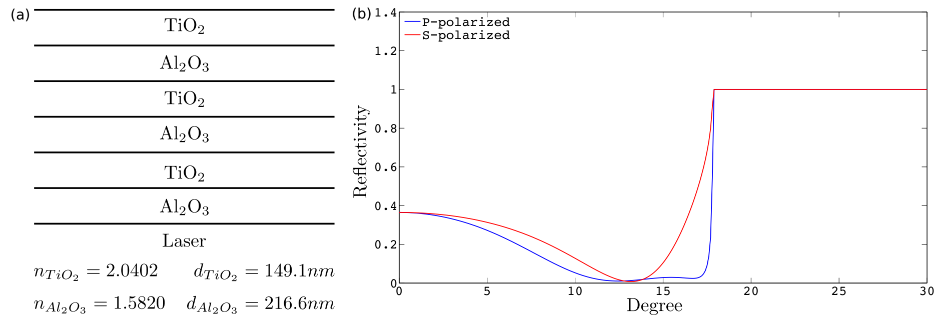

Figure 4.22: (a) Facet coating design; (b) Plot of the reflectivity of the coating in(a) at different incident angles.

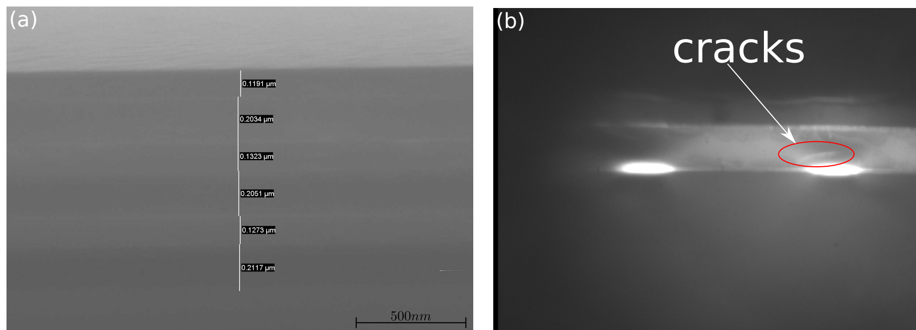

Figure 4.23: (a)SEM picture of the designed facet coating;(b) Near field of the laser mini bar with the facet coating.

4.4 Results of regrowth angled-grating broad-area lasers

Since we don't have access to the epitaxy layer growth, we have to use the third part foundry service. After the quantum well is grown, we fabricate the grating in the cladding layer by wet etching and then shipped back to the foundry service to grow the rest layers. The most important thing in this project is the quality of epitaxy layers which we cannot control. Unfortunately, after regrowth, we find there are a lot of defects in the regrowth layers which may be because the surface is not clean enough for the regrowth process. Figure 4.24 shows the SEM pictures of the defects in the regrowth layers. Due to the high density defects in the regrowth wafer, we find that even the broad-area laser doesn't work. We still finished the whole fabrication process, but none of the fabricated devices actually work.

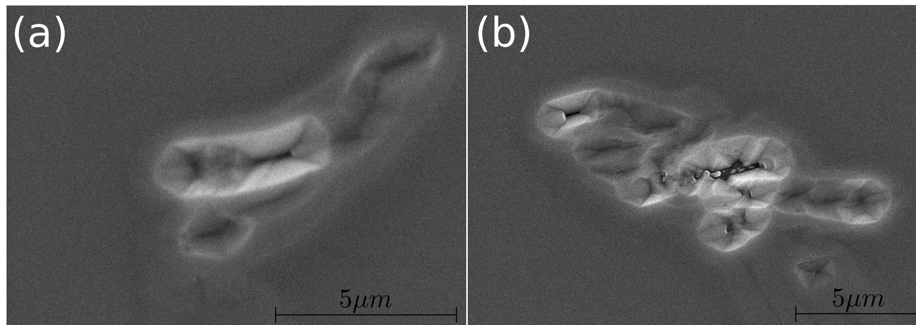

Figure 4.24: SEM pictures of the defects in the regrowth wafer.

Chapter 5

PHOTONIC CRYSTAL BRAGG LASER WITH TRIANGULAR LATTICE

5.1 Introduction

In the previous chapters, we have demonstrated the coherent beam combining of angled-grating broad-area lasers. The TBR grating is 1D periodic structure with 50% duty cycle. During fabrication, around 50% percent of semiconductor is etched/removed and replaced by an insulation material. On one hand, this may result in a higher electricity resistance due to a smaller cross-section area. On the other hand, the etched surface may introduce some surface defect states and increase the non-radiation recombination rate. In this chapter, we propose to replace the 1D TBR grating with the 2D photonic crystal cavity. Since there is also periodic structure along the propagation direction in the 2D photonic crystal cavity, it is possible to obtain single wavelength as well as single transverse mode simultaneously. As shown in fig. 5.1, there are two methods to design the 2D photonic crystal cavity, one

is with rectangle lattice [84, 85] and the other one is with triangle lattice. Compared to the rectangle lattice, the triangle lattice cavity is much easier to be coherently combined in the same method as in the coherently combined angled-grating broad-area laser. It can be shown that the coupling region in the triangle lattice 2D photonic crystal cavity has the same lattice unit as in the rest of cavity. Therefore, unlike in the combined angled-grating broad-area lasers, there should be no interfaces around the coupling region. In the following section, the design of the triangle lattice 2D photonic crystal cavity is present to obtain both single wavelength and single transverse mode. Then the measurement results of the single and combined photonic crystal Bragg lasers are shown and compared to the results of rectangle lattice photonic crystal cavity.

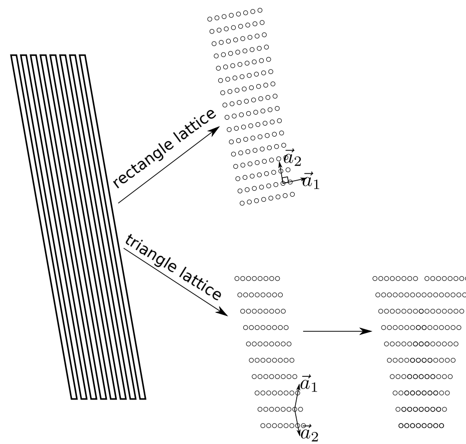

Figure 5.1: Schematic plot of rectangle and triangle 2D photonic crystal cavities substituting the 1D TBR grating.

5.2 Design

Figure. 5.2(a) and (b) show the triangle lattice in real and reciprocal space, respectively. $\vec{a}_1$,$\vec{a}_2$ and $\vec{b}_1$,$\vec{b}_2$ are the base vectors for the real and reciprocal lattices, respectively. Figure 5.3 shows the band structure of the triangle lattice along the $\vec{k}_x$ and $\vec{k}_y$ directions. k_x

and k_y are normalized by $\frac{2\pi}{d\cos\theta}$ and $\frac{2\pi}{l}$, respectively. We can find that along x direction, the effective period is $d\cos\theta$ and along y direction, the effective period is about l if θ is small enough($\theta = 10°$ in the simulation). Therefore in the following derivation, we use $d\cos\theta$ and l as the periods in the x and y directons.

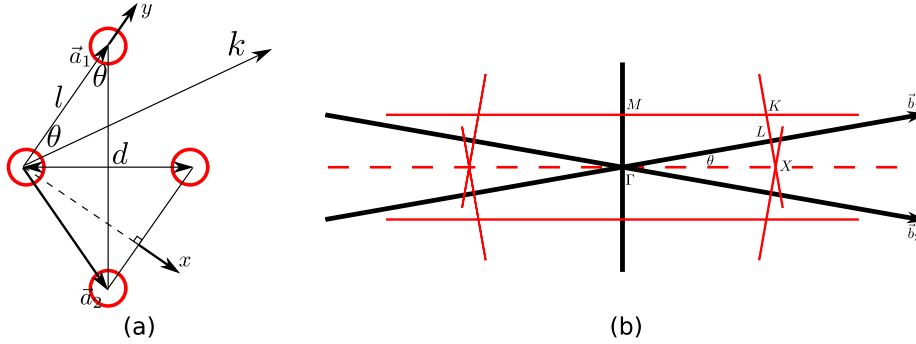

Figure 5.2: (a)Geometries and relationship with k vector in a triangle lattic with $\vec{a}_1$ and $\vec{a}_2$ as the base vectors;(b) Reciprocal lattice of (a) with $\vec{b}_1$ and $\vec{b}_2$ as the base vectors.

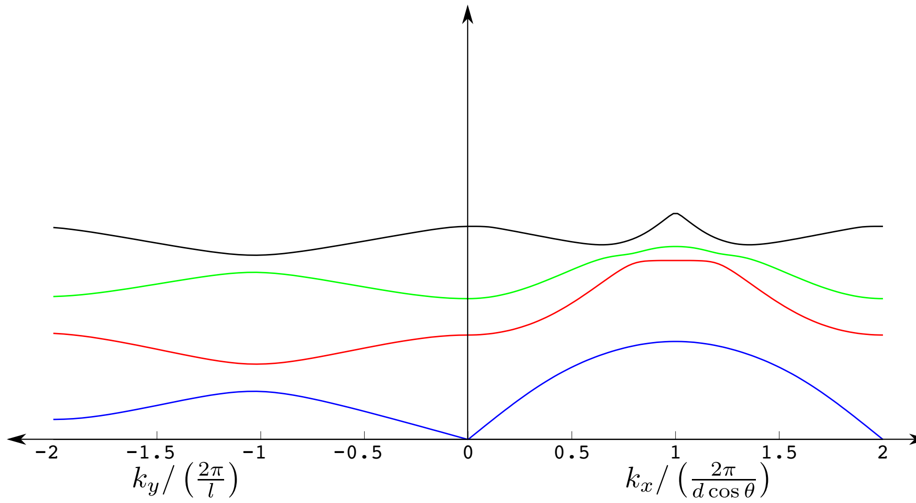

Figure 5.3: Band structures of triangle lattice with first four bands along both $\vec{k}_x$ and $\vec{k}_y$ direction,k_x is normalized by $\frac{2\pi}{d\cos\theta}$ and k_y is normalized by $\frac{2\pi}{l}$.

In order to obtain single wavelength and single mode operation, we would like to make the lattice resonate with the cavity mode in both the transverse and longitudinal direction(k_x and k_y in Fig. 5.2) and both with first order gratings in the best. From the resonance condi-

tion, we can obtain a relation between l and d. At the same time, l and d are also geometrically related. The two constrains are too strict to satisfy if we require first order grating as well. Therefore, we can loose the limitation of the grating order in one direction in order to meet the both constrains. Since the transverse mode control is more important to keep a good beam quality, I choose to set free the grating order of the longitudinal mode. That is why the integer parameter m shows in the following derivation.

$$k_x = k \sin\theta, k_y = k \cos\theta \tag{5.1}$$

Along the transverse direction(x), the cavity mode is resonate with the first order grating.

$$\begin{aligned} d\cos\theta &= \frac{1}{2}\frac{2\pi}{k_x} \\ &= \frac{1}{2}\frac{2\pi}{k\sin\theta} \\ &= \frac{1}{2}\frac{2\pi}{n_{eff}k_0\sin\theta} \\ &= \frac{1}{2}\frac{\lambda_0}{n_{eff}\sin\theta} \\ \therefore d &= \frac{\lambda_0}{n_{eff}\sin 2\theta} \end{aligned} \tag{5.2}$$

where λ_0 is the wavelength in vacuum.

Along the longitudinal direction(y), the cavity mode can be resonate with the mth order

grating.

$$
\begin{aligned}
l &= \frac{m}{2}\frac{2\pi}{k_y} \\
&= \frac{m}{2}\frac{2\pi}{k\cos\theta} \\
&= \frac{m}{2}\frac{2\pi}{n_{eff}k_0\cos\theta} \\
&= \frac{m}{2}\frac{\lambda_0}{n_{eff}\cos\theta} \\
\therefore l &= m\frac{\lambda_0}{2n_{eff}\cos\theta}
\end{aligned}
\tag{5.3}
$$

In the triangle lattice, l and d are related by

$$
l\sin\theta = \frac{d}{2} \tag{5.4}
$$

By substituting Equ. 5.2 and 5.3 in Equ. 5.4, we can obtain the following equation:

$$
m = \frac{1}{2\sin^2\theta} \tag{5.5}
$$

where m must a integer.

Equation. 5.5 indicates that only discrete value of θ can be used in the 2D photonic crystal cavity design. And the relation between m and θ is shown in Fig. 5.4. According to this figure, we will use $\theta = 10°$ where $m = 16$.

5.2.1 Coupled mode theory in 2D photonic grating

Starting from the coupled wave equation:

$$
\frac{\partial^2 E(x,z)}{\partial x^2} + \frac{\partial^2 E(x,z)}{\partial z^2} = -k_0^2(\varepsilon_0 + \Delta\varepsilon(x,z))E(x,z) \tag{5.6}
$$

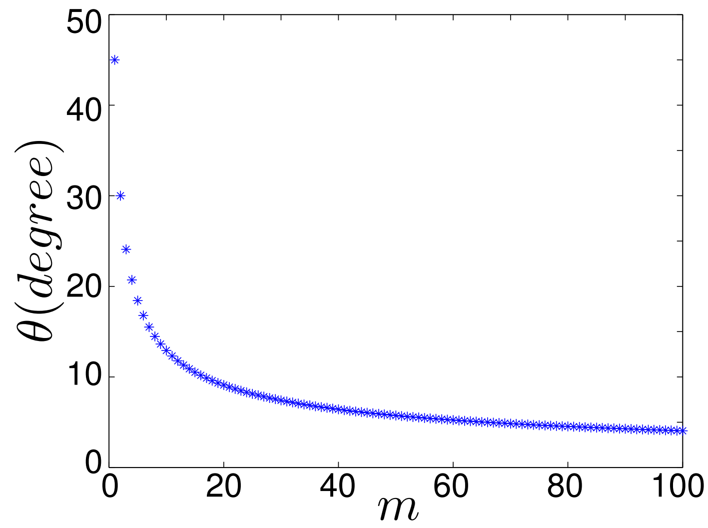

Figure 5.4: Relation between m and θ in the 2D photonic crystal cavity design

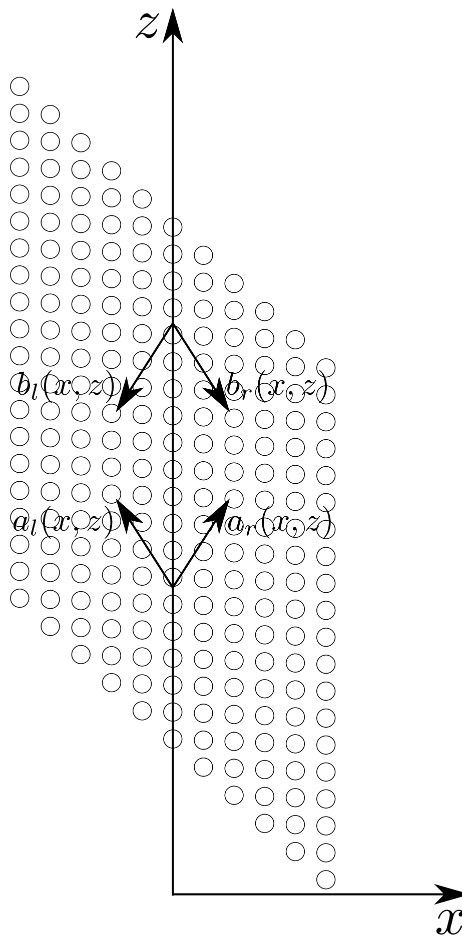

Figure 5.5: Schematic plot of 2D photoic crystal cavity with triangle lattice.

where ε_0 is the effective permittivity, $\Delta\varepsilon(x,z)$ is the permittivity difference and $E(x,z)$ is the electrical field distribution which can be written as

$$\begin{aligned} E(x,z) = {} & a_r(x,z)e^{-jk_x x}e^{-j\beta z} + a_l(x,z)e^{jk_x x}e^{-j\beta z} \\ & + b_r(x,z)e^{-jk_x x}e^{j\beta z} + b_l(x,z)e^{jk_x x}e^{j\beta z} \end{aligned} \tag{5.7}$$

where a_r, a_l, b_l and b_r are shown in Fig. 5.5.

We can substitute Equ. 5.6 with Equ. 5.7 and obtain

$$\begin{aligned} & \frac{\partial^2 a_r(x,z)}{\partial x^2}e^{-jk_x x}e^{-j\beta z} - 2jk_x\frac{\partial a_r(x,z)}{\partial x}e^{-jk_x x}e^{-j\beta z} - a_r(x,z)k_x^2e^{-jk_x x}e^{-j\beta z} \\ & +\frac{\partial^2 a_l(x,z)}{\partial x^2}e^{jk_x x}e^{-j\beta z} + 2jk_x\frac{\partial a_l(x,z)}{\partial x}e^{jk_x x}e^{-j\beta z} - a_l(x,z)k_x^2e^{jk_x x}e^{-j\beta z} \\ & +\frac{\partial^2 b_r(x,z)}{\partial x^2}e^{-jk_x x}e^{j\beta z} - 2jk_x\frac{\partial b_r(x,z)}{\partial x}e^{-jk_x x}e^{j\beta z} - b_r(x,z)k_x^2e^{-jk_x x}e^{j\beta z} \\ & +\frac{\partial^2 b_l(x,z)}{\partial x^2}e^{jk_x x}e^{j\beta z} + 2jk_x\frac{\partial b_l(x,z)}{\partial x}e^{jk_x x}e^{j\beta z} - b_l(x,z)k_x^2e^{jk_x x}e^{j\beta z} \\ & +\frac{\partial^2 a_r(x,z)}{\partial z^2}e^{-jk_x x}e^{-j\beta z} - 2j\beta\frac{\partial a_r(x,z)}{\partial z}e^{-jk_x x}e^{-j\beta z} - a_r(x,z)\beta^2e^{-jk_x x}e^{-j\beta z} \\ & +\frac{\partial^2 a_l(x,z)}{\partial z^2}e^{jk_x x}e^{-j\beta z} - 2j\beta\frac{\partial a_l(x,z)}{\partial z}e^{jk_x x}e^{-j\beta z} - a_l(x,z)\beta^2e^{jk_x x}e^{-j\beta z} \\ & +\frac{\partial^2 b_r(x,z)}{\partial z^2}e^{-jk_x x}e^{j\beta z} + 2j\beta\frac{\partial b_r(x,z)}{\partial z}e^{-jk_x x}e^{j\beta z} - b_r(x,z)\beta^2e^{-jk_x x}e^{j\beta z} \\ & +\frac{\partial^2 b_l(x,z)}{\partial z^2}e^{jk_x x}e^{j\beta z} + 2j\beta\frac{\partial b_l(x,z)}{\partial z}e^{jk_x x}e^{j\beta z} - b_l(x,z)\beta^2e^{jk_x x}e^{j\beta z} \\ & = - k_0^2(\varepsilon_0 + \Delta\varepsilon(x,z))\Big(a_r(x,z)e^{-jk_x x}e^{-j\beta z} + a_l(x,z)e^{jk_x x}e^{-j\beta z} \\ & \quad +b_r(x,z)e^{-jk_x x}e^{j\beta z} + b_l(x,z)e^{jk_x x}e^{j\beta z}\Big) \end{aligned} \tag{5.8}$$

We can use slow variation assumption and ignore the second derivative terms. Thus, we

can obtain

$$
\begin{aligned}
&\left(-2jk_x\frac{\partial a_r(x,z)}{\partial x}-2j\beta\frac{\partial a_r(x,z)}{\partial z}\right)e^{-jk_xx}e^{-j\beta z}-a_r(x,z)(k_x^2+\beta^2)e^{-jk_xx}e^{-j\beta z}\\
&+\left(2jk_x\frac{\partial a_l(x,z)}{\partial x}-2j\beta\frac{\partial a_l(x,z)}{\partial z}\right)e^{jk_xx}e^{-j\beta z}-a_l(x,z)(k_x^2+\beta^2)e^{jk_xx}e^{-j\beta z}\\
&+\left(-2jk_x\frac{\partial b_r(x,z)}{\partial x}+2j\beta\frac{\partial b_r(x,z)}{\partial z}\right)e^{-jk_xx}e^{j\beta z}-b_r(x,z)(k_x^2+\beta^2)e^{-jk_xx}e^{j\beta z}\\
&+\left(2jk_x\frac{\partial b_l(x,z)}{\partial x}+2j\beta\frac{\partial b_l(x,z)}{\partial z}\right)e^{jk_xx}e^{j\beta z}-b_l(x,z)(k_x^2+\beta^2)e^{jk_xx}e^{j\beta z}\\
&=-k_0^2(\varepsilon_0+\Delta\varepsilon(x,z))\left(a_r(x,z)e^{-jk_xx}e^{-j\beta z}+a_l(x,z)e^{jk_xx}e^{-j\beta z}\right.\\
&\quad\left.+b_r(x,z)e^{-jk_xx}e^{j\beta z}+b_l(x,z)e^{jk_xx}e^{j\beta z}\right)
\end{aligned}
\tag{5.9}
$$

Since $k_x^2+\beta^2=k_0^2\varepsilon_0$, the above equation can be simplified as

$$
\begin{aligned}
&\left(-2jk_x\frac{\partial a_r(x,z)}{\partial x}-2j\beta\frac{\partial a_r(x,z)}{\partial z}\right)e^{-jk_xx}e^{-j\beta z}+\left(2jk_x\frac{\partial a_l(x,z)}{\partial x}-2j\beta\frac{\partial a_l(x,z)}{\partial z}\right)e^{jk_xx}e^{-j\beta z}\\
&+\left(-2jk_x\frac{\partial b_r(x,z)}{\partial x}+2j\beta\frac{\partial b_r(x,z)}{\partial z}\right)e^{-jk_xx}e^{j\beta z}+\left(2jk_x\frac{\partial b_l(x,z)}{\partial x}+2j\beta\frac{\partial b_l(x,z)}{\partial z}\right)e^{jk_xx}e^{j\beta z}\\
&=-k_0^2\Delta\varepsilon(x,z)\left(a_r(x,z)e^{-jk_xx}e^{-j\beta z}+a_l(x,z)e^{jk_xx}e^{-j\beta z}+b_r(x,z)e^{-jk_xx}e^{j\beta z}+b_l(x,z)e^{jk_xx}e^{j\beta z}\right)
\end{aligned}
\tag{5.10}
$$

where $\Delta\varepsilon(x,z)$ can be expressed as

$$\Delta\varepsilon(x,z)=\sum_{p,q}\Delta\varepsilon_{p,q}e^{-i\vec{K}_{p,q}\cdot\vec{r}} \tag{5.11}$$

where

$$\vec{K}_{p,q}=p\frac{2\pi}{p_x}\hat{x}+q\frac{2\pi}{p_y}\hat{y}$$

and

$$\Delta\varepsilon_{p,q}=\frac{1}{S_{cell}}\iint_{cell}\Delta\varepsilon(x,z)e^{i\vec{K}_{p,q}\cdot\vec{r}}dxdy$$

where S_{cell} is the area of a unit cell, p_x and p_y are the periods in x and y directions, respec-

tively.

In a triangle unit cell,

$$\Delta\varepsilon(x,z) = \begin{cases} \Delta\varepsilon \ (r < r_h) \\ 0 \ (\text{elsewhere}) \end{cases} \tag{5.12}$$

and

$$\begin{aligned}
&\iint_{cell} \Delta\varepsilon(x,z) e^{i\vec{K}_{p,q}\cdot\vec{r}} dxdy = \iint_{hole} \Delta\varepsilon e^{i\left(p\frac{2\pi}{px}x + q\frac{2\pi}{py}y\right)} dxdy \\
=&\Delta\varepsilon \int_0^{r_h} \int_0^{2\pi} e^{ir\left(p\frac{2\pi}{px}\cos\theta + q\frac{2\pi}{py}\sin\theta\right)} r d\theta dr \\
=&\Delta\varepsilon \int_0^{r_h} r \int_0^{2\pi} e^{irK\cos(\theta+\theta_0)} d\theta dr \ (\text{where } K = \sqrt{\left(p\frac{2\pi}{p_x}\right)^2 + \left(q\frac{2\pi}{p_y}\right)^2}) \\
=&2\pi\Delta\varepsilon \int_0^{r_h} rJ_0(rK)dr = 2\pi\frac{\Delta\varepsilon}{K^2} \int_0^{r_h} KrJ_0(rK)dKr = 2\pi\frac{\Delta\varepsilon}{K^2} Kr_h J_1(Kr_h) \\
=&2\pi r_h^2 \Delta\varepsilon \frac{J_1(Kr_h)}{Kr_h}
\end{aligned} \tag{5.13}$$

Thus,

$$\Delta\varepsilon_{p,q} = 2\pi r_h^2 \frac{\Delta\varepsilon}{S_{cell}} \frac{J_1(Kr_h)}{Kr_h} \tag{5.14}$$

where $S_{cell} = \frac{1}{2} dl \cos\theta$, $p_x = d\cos\theta$ and $p_y = l$.

Therefore, the coupling coefficient κ_x can be expressed as

$$\kappa_x = \Gamma \frac{k_0^2}{2k_x} \Delta\varepsilon_{1,0} \tag{5.15}$$

where Γ is the confinement factor of the gratings.

Figure 5.6 shows the κ_x with respect to the etch depth. Like in the design of angled-grating broad-area lasers, the κ_x is preferred to be around $0.1/\mu m$. However, the corresponding etch depth is so deep that it will touch the quantum well. Therefore, we will set the etch depth between $1\mu m$ and $1.12\mu m$ without etching the undoped waveguide layer(indicated as

the dashed line in Fig. 5.6).

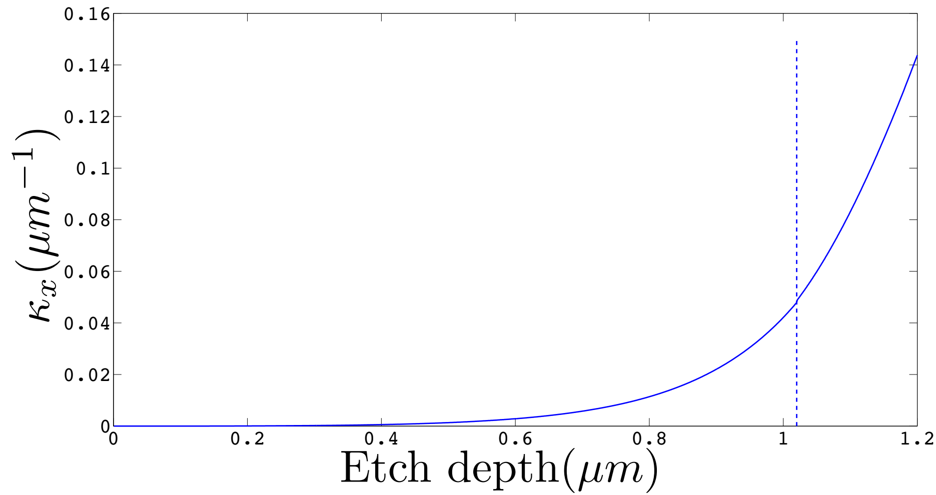

Figure 5.6: The plot of κ_x with respect to the etch depth

5.3 Measurement Results

The fabrication process is similar to the process described in Sec. 3.1. Different etch time is needed for different etch depth. Figure 5.7 shows the cross section of the 2D photonic crystal Bragg laser.

We take the measurement of LI curve, optical spectrum, near field and far field of the single and two coherently combined 2D photonic crystal Bragg lasers. Figure 5.8 shows the LI curve and optical spectrum of the triangle lattice 2D photonic crystal Bragg laser. In Fig. 5.8(a), we also include the LI curve of the rectangle lattice PC Bragg laser for comparison. It is obvious that the triangle lattice 2D PC Bragg laser has similar threshold and slope efficiency to those of the rectangle lattice 2D PC Bragg laser. In the angled-grating broad-area lasers, since the TBR grating is only resonant with the transverse wavevector, the longitude mode is actually defined by the two facets. Therefore, the angled-grating broad-area laser usually works in multiple wavelengths. In the 2D PC Bragg laser, both

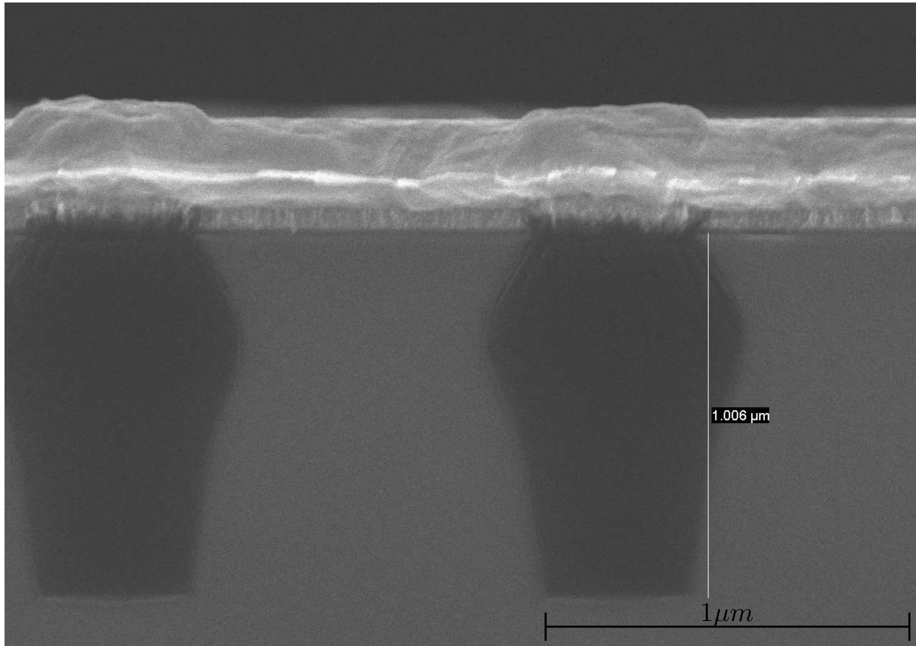

Figure 5.7: SEM picture of the cross section of a 2D photonic crystal Bragg laser.

the transverse and propagation wavevectors are required to be resonant with the 2D PC. Therefore the 2D PC Bragg laser is able to be single wavelength. During the optical spectrum measurement, it shows stable single wavelength without mode hopping and the stable spectrum is shown in Fig. 5.8(b). Figure 5.9(a) and (b) show the near field and far field of

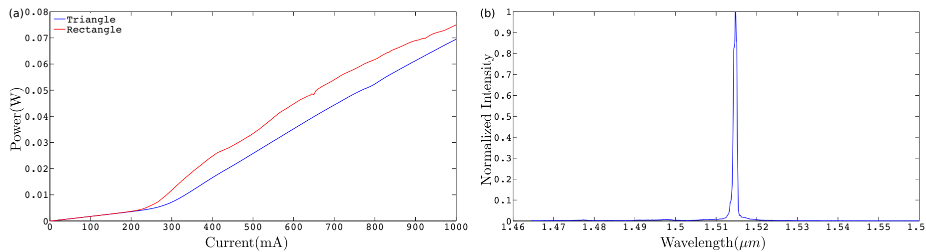

Figure 5.8: (a) LI curves of the single triangle lattice and rectangle lattice 2D photonic crystal Bragg lasers with the same parameters. (b) Optical spectrum of single triangle lattice 2D photonic crystal Bragg laser.

the single triangle lattice 2D PC Bragg laser, respectively. The near field profile shows that the aperture width is about $115.4\mu m$. The far field profile is a single lobe with divergent angle around 0.82° which indicates near diffraction-limited beam quality. Figure 5.10(a)

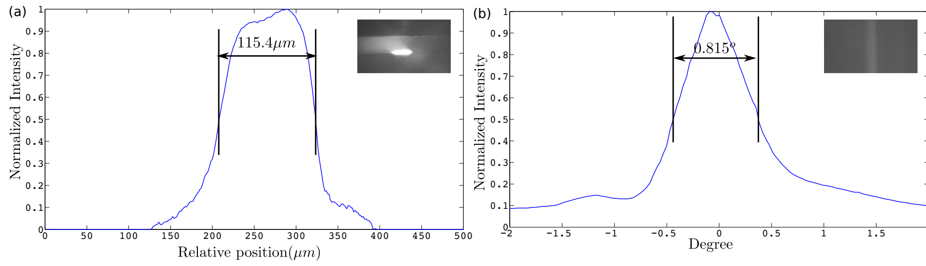

Figure 5.9: (a) Near field profile of single 2D PC Bragg laser. The camera image is shown in the inset. (b) Far field profile of single 2D PC Bragg laser. The inset is the camera image.

and (b) show the LI curve and far field of the tow combined PC Bragg laser. Along with the LI curve, we also show the result of the single PC Bragg laser and the twice output power of single emitter in the same figure for comparison. The low combining efficiency around 50% is due to the shallow etching depth of the grating. In the far field profile, multiple peaks are observed which indicates that the coherent combining is not obtained and the reason is the weak coupling coefficient due to the shallow etching depth of grating. As pointed out in the previous section, the etching depth is mainly limited by the wafer design, because we do not want to disturb the undoped waveguide epitaxy layer by dry etching. Therefore, in order to get a stronger coupling coefficient, a new wafer design with larger confinement factor may be needed.

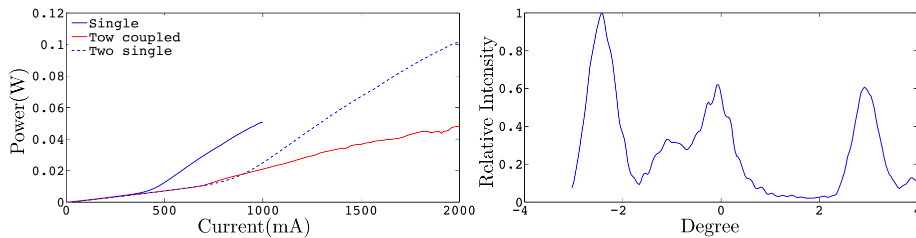

Figure 5.10: (a) LI curves of the single and two combined 2D PC Bragg lasers; (b) Far field profile of the two combined 2D PC Bragg lasers.

Chapter 6

FOLDED STRUCTURE OF ANGLED-GRATING BROAD-AREA LASERS

6.1 Introduction

The angled-grating broad-area laser is a promising candidate for high power, high brightness diode laser source. The key point in the design is the angled gratings which can simultaneously support the unique snake-like zigzag lasing mode and eliminate the direct Fabry-Perot(FP) feedback. In a conventional waveguide laser, the phase front of the guided mode does not change along the propagation direction. But for angled-grating broad-area lasers, the phase front exhibits a zigzag pattern with a large angle(equal to the grating tilt angle) with respect to the propagation direction, which provides an effective method to fold the cavity by use of mirror symmetry. In this chapter, we propose and experimentally demonstrate a folded cavity design for angled-grating broad-area lasers. The folded design can be also interpreted as two cascaded angled-grating broad-area lasers with opposite

tilting directions. We show that with a careful selection of the cavity length, a low loss lasing mode can be obtained. Compared to the regular angled-grating broad-area laser, we experimentally demonstrate that the folded cavity laser provides similar beam quality, but with a slightly higher threshold and smaller slope efficiency due to the additional loss at the interface.

One instant benefit of the new design is to occupy less wafer space than the regular angled-grating broad-area laser. In a regular angled-grating broad-area laser, the tilt angle is usually from 10° to 20° and the length of cavity can be as long as $4mm$. As a result, angled-grating broad-area lasers can use 10 times wafer space more than conventional straight cavity broad-area lasers. The proposed design only takes 50% wafer space of the regular angled-grating broad-area laser with the same cavity length. And in principle, multiple foldings can be used to further reduce the required wafer space for a long cavity laser.

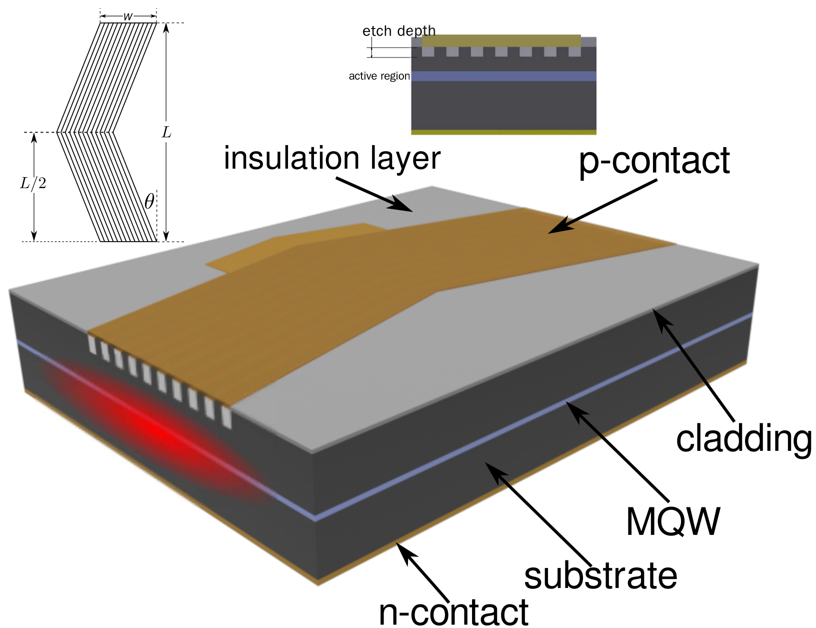

Figure 6.1: Schematic plot of a folded angled-grating broad-area laser.

6.2 Laser design

Figure 6.1 shows the schematic plot of a folded cavity angled-grating broad-area laser. The laser consists of two cascaded angled-grating broad-area lasers that tilt to opposite directions. The waveguide mode in each half is the same as that in an unfolded angled-grating cavity as shown in Fig. 6.2(a). The snake-like zigzag mode consists of two planewave-like components in resonance with the gratings, denoted as R_1 and R_2 in Fig. 6.2(b). The wavevectors of R_1, R_2 and the gratings satisfy the phase matching condition: $\vec{k}_{R_1} + \vec{k}_G = \vec{k}_{R_2}$ as shown in the inset of Fig. 6.2(b). The angle between $\vec{k}_{R_1}(\vec{k}_{R_2})$ and the grating axis is equal to θ, the grating tilt angle. A detailed modal gain analysis of the grating confined modes can be found in [45] and the mode theory of an unfolded angled-grating broad-area laser is well explained in [43]. At the two end facets in Fig. 6.2(c), the propagation direction of $R_1(R_2^{'})$ component is perpendicular to the facet and that of $R_2(R_1^{'})$ is tilted by 2θ. When reflected, $R_1(R_2^{'})$ component will be efficiently fed back to the cavity and $R_2(R_1^{'})$ component will be lost. Therefore, at the facet, the preferred cavity mode will have the maximum perpendicular component(R_1, $R_2^{'}$ in this example) and minimum tilted component(R_2, $R_1^{'}$ in this example). At the interface between two halves, the cavity mode with the maximum transmissivity, T, from one half to another will be preferred. According to [43, 46], the transmissivity T can be expressed as:

$$T = T_0 \times \frac{\eta_0}{2c_0\mu_0 P_0} \int_{-\infty}^{\infty} |E_{R_1} E_{R_2^{'}}| e^{j2k\sin(\theta_B)x} dx \tag{6.1}$$

where T_0 is the Fresnel transmission coefficient, P_0 is the power in the incident mode, μ_0 and c_0 are the magnetic permeability and speed of light in vacuum, and θ_B is the actual incident angle of the incident mode relative to the middle interface as shown in the inset of Fig. 6.2(c). The maximum transmissivity is obtained when $\theta_B = 0$. This means that the

maximum transmission happens between two perpendicular components on both sides(R_1, $R_2^{'}$ in this example). This is also indicated by the k-vector relationship in Fig. 6.2(c). It shows that the transmission from R_2 to $R_2^{'}/R_1^{'}$ and from R_1 to $R_1^{'}$ suffers high loss due to the large wavevector mismatch. Since the phase front and mode profile of R_1 and $R_2^{'}$ are identical, it allows for efficient mode coupling. As a result, the length of one half($L/2$) should be integer times of $2L_c$, where L_c is the coupling length of R_1 and R_2, defined as the length during which the power of one component is fully coupled into the other component. The coupling length can be calculated through $L_c = \pi/|\beta_1 - \beta_2|$, where β_1 and β_2 are the propagation constants of the first two lowest modal loss Bragg modes confined by the gratings. If this condition is not satisfied, the mode will suffer high loss at the interface. Figure 6.2(d) and (e) show the mode profiles in a symmetrically folded angled-grating cavity when $L = 4NL_c$ and $L = (4N + 2)L_c$, respectively, where N is an integer. When the correct cavity length condition is satisfied in Fig. 6.2(d), we can obtain a low loss folded cavity mode with efficient mode coupling at the middle interface. But strong diffraction loss is observed in Fig. 6.2(e) when this condition is not satisfied. There is another constraint condition on the cavity length L. To suppress the direct FP feedback between two end facets, we have to eliminate that on both halves, which means L must satisfy $\tan(\theta)\,(L/2) > W$. All the mode profiles are obtained by the FDTD method.

The folded cavity angled-grating broad-area lasers are fabricated in an InP-based multiple quantum well (MQW) epitaxy wafer. The details of the epitaxy wafer is described in [83]. The tilting angle θ is set to be 10° and accordingly, the grating period is calculated to be $1.368\mu m$. The etch depth of $900nm$ is chosen to obtain a grating coupling coefficient around $0.1/\mu m$ and 100 periods of gratings are etched, resulting in a total width around $140\mu m$. The grating coupling length is calculated to be about $150\mu m$ which matches well with our previous experiments on the conventional angled-grating broad-area lasers. Accordingly, the final length of the folded cavity is selected to be around $1.8mm$ which is

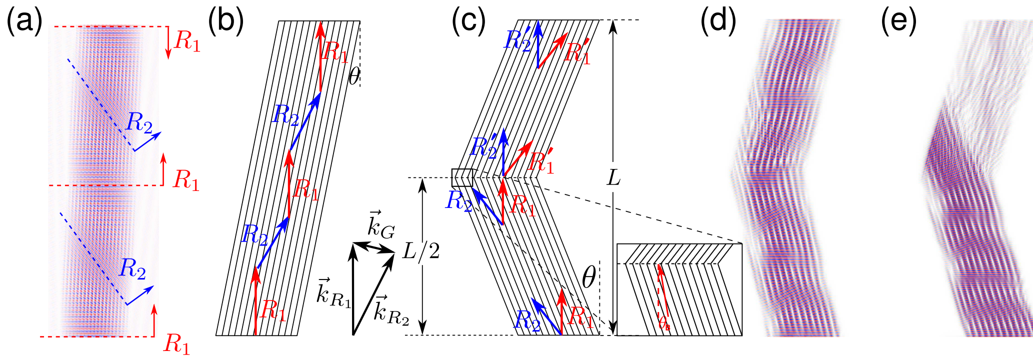

Figure 6.2: (a) and (b) Simulation result and mode profile of an unfolded angled-grating broad-area laser; (c) Mode coupling in a folded cavity angled-grating broad-area laser. The inset is the zoom-in view at the interface; (d) Simulation result of the preferred mode when $L = 4NL_c$; (e) Simulation result of high diffraction loss when $L = (4N + 2)L_c$.

about 12 times of the calculated coupling length. The fabrication process is similar to that of angled-grating broad-area lasers in Section 3.1. Figure 6.3 shows the scanning electron microscope pictures of the devices.

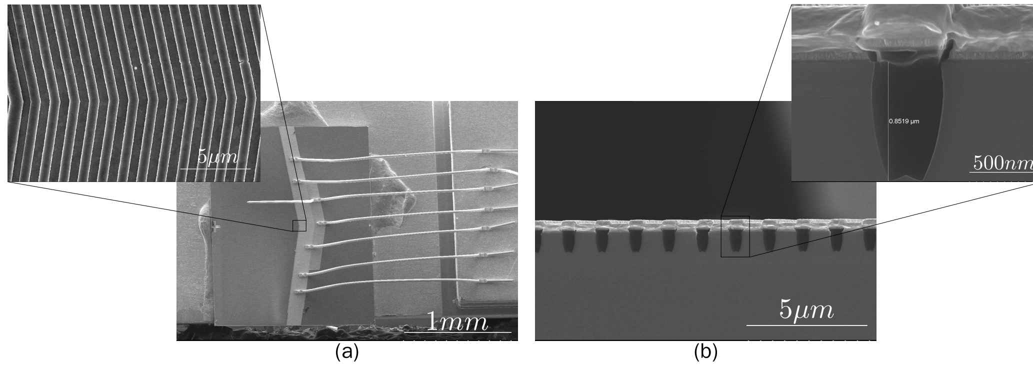

Figure 6.3: (a) Top view of the packaged folded cavity angled-grating broad-area laser. The inset is the zoom-in view at the interface; (b) Cross-section of the folded cavity laser. The inset is the zoom in view of one etched trench.

6.3 Measurement results and discussion

We measure the folded and unfolded cavity angled-grating broad-area laser with the same cavity length for comparison. The two types of devices are fabricated together with the

same fabrication processes and parameters. All the measurements are carried out with a CW current source in a cryostat with the temperature set at 250K. Figure 6.4(a) shows the near field profiles of the folded cavity and unfolded cavity angled-grating broad-area laser. The widths of aperture are $155.3\mu m$ and $156.1\mu m$ for folded and unfolded cavity, respectively. The width should be similar because both cavities have the same grating design. The far field profiles and camera images are shown in Fig. 6.4(b). The divergence angles are 0.96^o and 0.78^o for the folded cavity and unfolded cavity, respectively. We also include the theoretical far field calculated from a planewave aperture with the same width as what we measured. The simulated result is shown in green dash-dotted line in Fig. 6.4(b). The divergence angle of the folded cavity is a little bit larger than that of the unfolded cavity due to the existence of the middle interface. The angled gratings can be considered as a waveguide where the desired Bragg mode is filtered. The folded design needs longer cavity or stronger coupling to eliminate the undesired components induced by the interface. This means with the same etching depth and cavity length as in our situation, the folded cavity will have a slightly larger divergence angle along the slow axis. However, the difference is small in our experiments and both devices can be considered as near diffraction-limited. Figure 6.4(c) shows the light-current(LI) curves of the folded and unfolded cavity. For the unfolded cavity, the threshold and slope efficiency are $365.5mA$ and $0.21W/A$, respectively. Compared to the unfolded cavity, the folded cavity has a larger threshold of $436.4mA$ and smaller slope efficiency of $0.14W/A$. The differences in LI curves are due to the extra optical loss induced by the interface in the folded cavity. The relatively strong spontaneous emission before lasing is due to the scattering loss induced by the deeply etched gratings. We believe that the output power is mainly limited by thermal management and the epitaxy wafer which is not designed or optimized for high power applications. The interface may also be the reason for the different lasing wavelength in the two devices as shown in Fig. 6.4(d). The lasing wavelengths for the folded and unfolded cavity are $1542.7nm$ and $1521.8nm$, respectively.

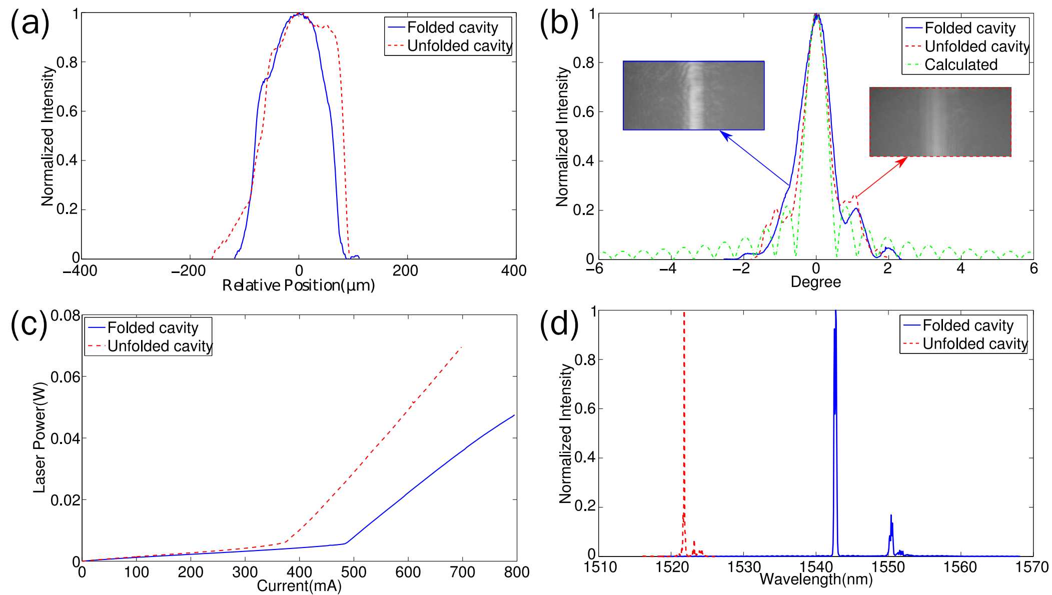

Figure 6.4: (a) Near field profiles of the folded cavity(blue solid line) and unfolded cavity(red dashed line). (b) Far field profiles and camera images of the folded cavity(blued solid line) and unfolded cavity(red dashed line). The calculated far field is shown in green dash-dotted line. (c) Light-current curves of the folded cavity(blue solid line) and unfolded cavity(red dashed line). (d) Optical spectrum of the folded cavity(blue solid line) and unfolded cavity(red dashed line).

It is possible that extra heat is generated because of the extra loss induced by the interface in the folded cavity. This reduces the efficiency and the wavelength is red-shifted due to the heat. Since the gratings are only resonant with the transverse wave vector, multiple longitudinal modes are allowed in the angled-grating broad-area lasers [43]. The existence of the interface also changes the longitudinal mode resonance condition, resulting in the small peak at 1550nm in the spectrum of the folded cavity laser.

6.4 Coherent beam combining of two folded angled-grating broad-area lasers

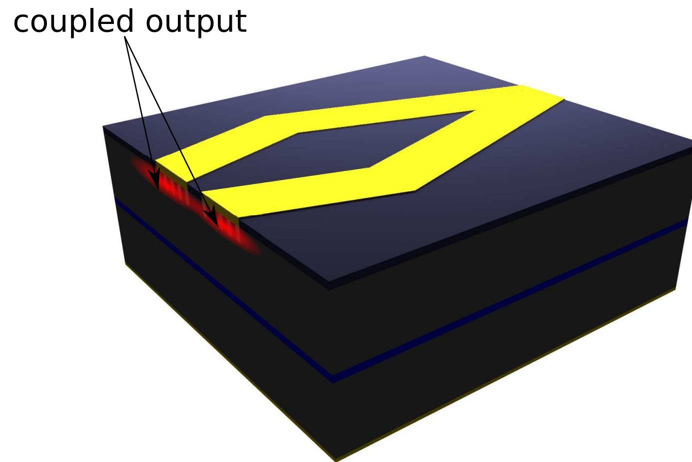

Figure 6.5: Schematic plot of the combined folded angled-grating broad-area laser.Two folded angled-grating broad-area lasers are coherently combined in the same way as in the combined angled-grating broad-area laser. The distance between the two emitters is reduced, resulting in an increased angular distance in the far field.

In the first chapter, we have mentioned that the brightness of a coherently beam combined laser array can only be improved by around N times in practice instead of N^2 times in theory because the filling factor is less than one. In the previous measurement results of the coherently combined angled-grating broad-area laser, the angular distance in the far-field

pattern will increase if we can reduce the distance between the emitter apertures. And once the angular distance is larger than the diffraction angle, there will be only the center peak in the far field. With the angled-grating broad-area lasers as the building block in the array, the longer the laser cavity, the further the distance between the emitter apertures and the smaller the filling factor which may diminish the brightness improvement.

Figure 6.5 shows the schematic plot of a two coherently combined folded angled-grating broad-area laser. With the folded angled-grating broad-area laser coherently combined in the same way as in the coherently combined angled-grating broad-area laser, it is possible to reduce the distance between the two apertures. In the previous section, we have shown that the folded angled-grating broad-area laser has similar performance to that of the angled-grating broad-area laser. Therefore, the combined folded angled-grating broad-area laser should have similar performance to the combined angled-grating broad-area laser, but with a larger angular distance in the far field measurement. Figure 6.6 shows the near field and far field profiles of the coherently combined folded angled-grating broad-area laser. The total length of the laser cavity is about 1.8mm and the distance between the two apertures is about 344.2μm compared to 634.8μm in the combined angled-grating broad-area laser with the same cavity length. And the angular distance in the far field profile as shown in fig. 6.6(b) is increased to 0.3736°. The angular distance of the combined angled-grating broad-area laser with the same cavity length is about 0.1399°.

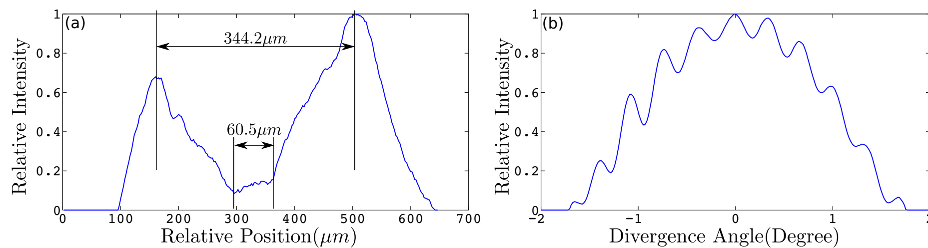

Figure 6.6: (a) Near field profile and (b) Far field profile of the coherently combined folded angled-grating broad-area laser.

The preliminary results have shown that the combined folded angled-grating broad-area laser has a larger angular distance. We can further reduce the distance between the apertures since there is still about $60.5\mu m$ gap. However, only reducing the distance may be not enough to obtain the single peak in the far field, because the filling factor of the mode in one aperture is small. Therefore, in future, along with reducing the aperture distance, we should also increase the output power to increase the mode filling factor and the overall filling factor as well.

Chapter 7

CONCLUSION

In summary, we have demonstrated the coherent beam combining of angled-grating broad-area lasers with two and six emitters coherently combined in an array. Both the far fields with interference fringes in a single lobe envelope prove that the emitters in the array are indeed coherently combined with near diffraction-limited beam quality. For the two combined laser, the output power can be above $1W$ using p-side-down bonding. And it is shown that the combining efficiency is almost one. For the six combined laser array, due to the propagation of SMA modes within the cavity, there are two symmetry peaks in the far field measurement. One possible way to eliminate the SMA modes in the multiple emitters combined array is to deposit a angular selective coating which has a larger reflectivity at perpendicular incident and small reflectivity at some certain incident angle. However, the evaporator is not accurate enough to deposit such a multilayer facet coating, therefore we still cannot get rid of those SMA modes peaks in the far field.

In order to reduce the total loss and to obtain single wavelength as well, we investigate and fabricate the 2D triangle lattice PC Bragg laser. The results of the single 2D triangle-lattice PC Bragg laser show single longitudinal and transverse mode at the same time with near diffraction-limited beam quality. However, due to the limitation on the etching depth,

the coupling coefficient is smaller than the design value and there are multiple peaks in the far field profile of the two combined 2D triangle lattice PC Bragg laser. For the regrowth laser diodes, none of the devices lase because of the bad regrowth quality in the wafer.

At last, we investigate the folded cavity angled-grating broad-area laser and the two combined folded cavity lasers. We compare the results of a folded cavity laser to those of a regular angled-grating broad-area laser with the same cavity length. The folded cavity has a slightly higher threshold and smaller slope efficiency due to some extra loss induced by the folded interface. It has been pointed out that the folded cavity design uses less wafer area and consequently can increase the yield. More important I think is that unlike in the combined angled-grating broad-area laser where the longer the cavity length, the smaller the filling factor, the combined folded cavity lasers can still have almost the unity filling factor due to the folded cavity feature. The far field of the fabricated laser shows a larger angular distance between the interference fringes than that of the angled-grating broad-area laser with the same length.

In the future, I still think the regrowth method is the most promising direction, because the regrowth grating should have the least loss because it has very shallow wet etching and the high temperature during growth may reflow the gratings a little bit to make it more smooth. With a better regrowth quality, I think better results including higher output power, diffraction-limited beam quality and etc. can still be expected.

BIBLIOGRAPHY

[1] C D Nabors. Effects of phase errors on coherent emitter arrays. *Applied Optics*, 33(12):2284–2289, 1994.

[2] B Lax. Semiconductor lasers. *Science*, 141:1247–1255, 1963.

[3] Z. I Aleerov, V. M Andreev, E. L Portnoi, and M. K Trukan. AlAs-GaAs heterojunction injection lasers with a low room-temperature threshold. *Soviet Physics Semiconductors-USSR*, 3(9):1107–&, 1970.

[4] H. Kroemer. A proposed class of hetero-junction injection lasers. *Proceedings of the IEEE*, 51(12):1782–1783, Dec 1963.

[5] R. D Dupuis, P. D Dapkus, N Holonyak, E. A Rezek, and R Chin. Room-temperature laser operation of quantum-well Ga(1-x)AlxAs-GaAs laser-diodes grown by organometalluic chemical vapor-deposition. *Applied Physics Letters*, 32(5):295–297, 1978.

[6] K. J Vahala, J. A Lebens, C. S Tsai, T. F Kuech, P. C Sercel, M. E Hoenk, and H Zarem. Quantum wire and quantum dot semiconductor-lasers. In PEYGAMBARIAN, N, editor, *Nonlinear Optical Materials and Devices for Photonic Switching*, volume 1216 of *Proceedings of the society of photo-optical instrumentation engineers (SPIE)*, pages 120–129, 1990.

[7] LA Coldren. Monolithic tunable diode lasers. *IEEE Journal of Selected Topics in Quantum Electronics*, 6(6):988–999, NOV-DEC 2000.

[8] Pja Thijs, Lf Tiemeijer, Pi Kuindersma, Jjm Binsma, and T Vandongen. High-performance 1.5 micro-m wavelength InGaAs-InGaAsP strained quantum-well lasers and amplifiers. *IEEE Journal of Quantum Electronics*, 27(6):1426–1439, JUN 1991.

[9] R. Menna, A. Komissarov, M. Maiorov, V. Khalfin, L. DiMarco, J. Connolly, and D. Garbuzov. High power 1550 nm distributed feedback lasers with 440 mw cw output power for telecommunication applications. In *Lasers and Electro-Optics, 2001. CLEO '01. Technical Digest. Summaries of papers presented at the Conference on*, pages CPD12–CP1, May 2001.

[10] F. Gerschuetz, M. Fischer, J. Koeth, I. Krestnikov, A. Kovsh, C. Schilling, W. Kaiser, S. Hoefling, and A. Forchel. 1.3 mu m Quantum Dot Laser in coupled-cavity-injection-grating design with bandwidth of 20 GHz under direct modulation. *OPTICS EXPRESS*, 16(8):5596–5601, 2008.

[11] MG Allen. Diode laser absorption sensors for gas-dynamic and combustion flows. *Measurement Science & Technology*, 9(4):545–562, 1998.

[12] P Werle, F Slemr, K Maurer, R Kormann, R Mucke, and B Janker. Near- and mid-infrared laser-optical sensors for gas analysis. *Optics and Lasers in Engineering*, 37(2-3):101–114, 2002.

[13] N Fabricius, G Gauglitz, and J Ingenhoff. A gas sensor based on an integrated optical Mach-Zehnder interferometer. *Sensors ans Acutators B-Chemical*, 7(1-3):672–676, 1992.

[14] G Hollemann, B Braun, F Dorsch, P Hennig, P Heist, U Krause, U Kutschki, and H Voelckel. RGB lasers for laser projection displays. In Wu, MH, editor, *Projection Displays 2000: Sixth in a series*, volume 3954 of *Proceedings of the society of photo-optical instrumentation engineers (SPIE)*, pages 140–151, 2000.

[15] G Hollemann, B Braun, P Heist, J Symanowski, U Krause, J Kranert, and C Deter. High-power laser projection displays. In Wu, MH, editor, *Projection Displays VII*, volume 4294 of *Proceedings of the society of photo-optical instrumentation engineers (SPIE)*, pages 36–46, 2001.

[16] Hui Dong, Yunfang Zhang, Hui Li, Jingyuan Duan, Ancun Shi, Qing Fang, and Yu-liang Liu. High-performance illumination system design with new light source of LD array for laser projection display. In Guo, H and Ding, Q, editor, *2012 International Workshop on Image Processing and Optical Engineering*, volume 8335 of *Proceedings of SPIE*, 2012.

[17] Tao Fang, Yiyuan Liu, Yan Qi, Ying Zhang, Bin Wang, Guang Zheng, Shaowei Chu, Boxia Yan, Hua Cheng, Yanwei Wang, and Yong Bi. Highly efficient and compact continuous-wave 456nm blue laser for laser projection display. In *2009 LaserS & Electro-Optics & The Pacific RIM Conference on Lasers and Electro-Optics, Vols 1 and 2*, pages 625–626, 2009.

[18] T. Y Fan and R. L Byer. Diode laser-pumped solid-state lasers. *IEEE Journal of Quantum Electronics*, 24(6):895–912, 1988.

[19] S. C Tidwell, J. F Seamans, M. S Bowers, and A. K Cousins. Scaling CW Diode-end-pumped ND-YAG Lasers to high average powers. *IEEE Journal of Quantum Electronics*, 28(4):997–1009, 1992.

[20] P Laporta and M Brussard. Design criteria for mode size optimization in diode-pumped solid-state lasers. *IEEE Journal of Quantum Electronics*, 27(10):2319–2326, 1991.

[21] EC Honea, RJ Beach, SB Sutton, JA Speth, SC Mitchell, JA Skidmore, MA Emanuel, and SA Payne. 115-W Tm:YAG diode-pumped solid-state laser. *IEEE Journal of Quantum Electronics*, 33(9):1592–1600, 1997.

[22] G Volluet, JP Hirtz, G Feugnet, JP Pocholle, E Durand, and JL Ayral. High Brightness stack arrays for DPSSL Laser Applications. In Galarneau, P, editor, *Laser Diodes and Applications III*, volume 3415 of *Proceedings of the society of photo-optical instrumentation engineeers (SPIE)*, pages 38–48, 1998.

[23] C Hanke. High power semiconductor laser diodes. *Informacije Midem-Journal of Microelectronics Electronic Components and Materials*, 31(4):232–236, 2001.

[24] Mathias Ziegler, Jens W. Tomm, Ute Zeimer, and Thomas Elsaesser. Imaging Catastrophic Optical Mirror Damage in High-Power Diode Lasers. *Journal of Electronic Materials*, 39(6):709–714, 2010.

[25] T Y Fan. Laser Beam Combining for High-Power , High-Radiance Sources. *Quantum*, 11(3):567–577, 2005.

[26] A Tünnermann, S Höfer, A Liem, J Limpert, M Reich, F Röser, and T Schreiber. Power Scaling of High-Power Fiber Lasers and Amplifiers. *Laser Physics*, 15(1):107–117, 2005.

[27] Jay W Dawson, Michael J Messerly, Raymond J Beach, Miroslav Y Shverdin, A Stappaerts, Arun K Sridharan, Paul H Pax, John E Heebner, Craig W Siders, and C P J Barty. Analysis of the scalability of diffraction-limited fiber lasers and amplifiers to high average power. *Optics Express*, 16(17), 2008.

[28] S. D. Demars, K. M. Dzurko, R. J. Lang, D.R. Welch, D.R. Scifres, and A. Hardy. Angled-grating distributed feedback laser with 1 W cw single-mode diffraction-limited output at 980nm. In *Lasers and Electro-Optics, 1996. CLEO '96., Summaries of papers presented at the Conference on*, pages 77–78, 1996.

[29] V. V. DWong, S. D. DeMars, A. Schoenfelder, and R. J. Lang. Angled-grating distributed-feedback laser with 1.2 W cw single-mode diffraction-limited output at 10.6μm. In *In Laser and Electro-Optics, 1998. CLEO '98., Summaries of papers presented at the Conference on*, pages 34–35, 1998.

[30] Katrin Paschke, Alexander Bogatov, Frank Bugge, Alexander E Drakin, Jörg Fricke, Reiner Güther, Alexey A Stratonnikov, Hans Wenzel, Götz Erbert, and Günther Tränkle. Properties of ion-implanted high-power angled-grating distributed-feedback lasers. *IEEE J. Sel. Top. Quantum Electron.*, 9(5):1172–1178, 2003.

[31] K. Paschke, R. Guther, J. Fricke, F. Bugge, G. Erbert, and G. Trankle. High power and high spectral brightness in 1060 nm alpha-dfb lasers with long resonators. *Electron. Lett.*, 39(4):369–370, FEB 20 2003.

[32] R. E. Bartolo, W. W. Bewley, I. Vurgaftman, C. L. Felix, J. R. Meyer, and M. J. Yang. Mid-infrared angled-grating distributed feedback laser. *Appl. Phys. Lett.*, 76(22):3164–3166, MAY 29 2000.

[33] T. Salzman, T. Venkatesan, S. Margalit, and A. Yariv. An unstable resonator semiconductor laser. In *Optical Society of America Meeting, San Diego, CA*, page paper ThV3, 1984.

[34] M. L. Tilton, G. C. Dente, A. H. Paxton, J. Cser, R. K. Defreez, C. E. Moeller, and D. Depatie. High power, nearly diffraction-limited output from a semiconductor laser with an unstable resonator. *IEEE J. Quantum Electron.*, 27:2098–2108, 1991.

[35] E. S. Kintzer, J. N. Walpole, S. R. Chinn, C. A. Wang, and L. J. Missaggia. High power strained layer amplifiers and lasers with tapered gain regions. *IEEE Photon. Technol. Lett.*, 5:605–608, 1993.

[36] Z. Bao, R. K. Defreez, P. D. Carleson, C. Largent, C. Moeller, and G. C. Dente. Spatio-spectral characteristics of a high power, high brightness cw ingaas/algaas unstable resonator semiconductor laser. *Electron. Lett.*, 29(18):1597–1599, 1993.

[37] D. Masanotti and F. Causa. Optical guiding properties of high-brightness parabolic bow-tie laser arrays. *IEEE J. Quantum Electron.*, 41:909–916, 2005.

[38] J. P. Donnelly, R. K. Huang, J. N. Walpole, L. J. Missaggia, C. T. Harris, J. Plant, R. J. Bailey, D. E. Mull, W. D. Goodhue, and G. W. Turner. Algaas-ingaas slab-coupled optical waveguide lasers. *IEEE J. Quantum Electron.*, 39:289–298, 2003.

[39] R. K. Huang, J. P. Donnelly, L. J. Missaggia, C. T. Harris, J. Plant, D. E. Mull, and W. D. Goodhue. High-power nearly diffraction-limited algaas-ingaas semiconductor slab-coupled optical waveguide laser. *IEEE Photon. Technol. Lett.*, 15:900–902, 2003.

[40] R. K. Huang, L. J. Missaggia, J. P. Donnelly, C. T. Harris, and G. W. Turner. High-brightness slab-coupled optical waveguide laser arrays. *IEEE Photon. Technol. Lett.*, 17:959–961, 2005.

[41] L. J. Missaggia, R. K. Huang, B. Chann, R. Swint, J. P. Donnelly, A. Sanchez, and G. W. Turner. Packaging and thermal management of high-power, slab-coupled optical waveguide laser arrays for beam combining. In *Electronic Components and Technology Conference*, pages 998–1004, 2008.

[42] Robert J Lang, Ken Dzurko, Amos A Hardy, Scott Demars, Alexander Schoenfelder, and David F Welch. Theory of Grating-Confined Broad-Area Lasers. *Quantum*, 34(11):2196–2210, 1998.

[43] A.M. Sarangan, M.W. Wright, J.R. Marciante, and D.J. Bossert. Spectral properties of angled-grating high-power semiconductor lasers. *IEEE Journal of Quantum Electronics*, 35(8):1220–1230, 1999.

[44] R. Guther. Beam propagation in an active planar waveguide with an angled bragg grating (α laser). *J. Mod. Optic.*, 45(7):1537–1546, July 1998.

[45] Lin Zhu, Axel Scherer, and Amnon Yariv. Modal Gain Analysis of Transverse Bragg Resonance Waveguide Lasers With and Without Transverse Defects. *October*, 43(10):934–940, 2007.

[46] D. Marcuse. Reflection loss of laser mode from tilted end mirror. *J. Lightwave. Technol.*, 7(2):336–339, 1989.

[47] C. Wirth, O. Schmidt, I. Tsybin, T. Schreiber, R. Eberhardt, J. Limpert, A. Tünnermann, K. Ludewigt, M. Gowin, E. Have, and M. Jung. High average power spectral beam combining of four fiber amplifiers to 8.2kW. *Opt. Lett.*, 36:3118–3120, 2011.

[48] O. Andrusyak, V. Smirnov, G. Venus, and L. Glebov. Beam combining of lasers with high spectral density using volume Bragg gratings. *Opt. Commun.*, 282:2560–2563, 2009.

[49] B. Chann, R. K. Huang, L. J. Missaggia, C. T. Harris, Z. L. Liau, A. K. Goyal, J. P. Donnelly, T. Y. Fan, A. Sanchez-Rubio, and G. W. Turner. Near-diffraction-limited diode laser arrays by wavelength beam combining. *Opt. Lett.* , 30:2014–2106, 2005.

[50] D. Vijayakumar, O. B. Jensen, R. Ostendorf, T. Westphalen, and B. Thestrup. Spectral beam combining of a 980nm tapered diode laser bar. *Opt. Express*, 18:893–898, 2010.

[51] D. F. Welch, D Scifres, P Cross, H Kung, W Streifer, R. D Burnham, and J Yaeli. High-power (575 mW) single-lobed emission from a phased-array laser. *Electron. Lett.*, 21(14):603–605, 1985.

[52] E. Kapon, J. Katz, and A. Yariv. Supermode analysis of phase locked arrays of semiconductor lasers. *Opt. Lett.*, 10:125–127, 1984.

[53] David F Welch, P. S. Cross, D. R. Scifres, W. Streifer, and R. D. Burnham. High power (cw) in-phase locked 'Y' coupled laser arrays. *Appl. Phys. Lett.*, 49:1632–1634, 1986.

[54] D. Botez, P. Hayashida, L. J. Mawst, and T. J. Roth. Diffraction-limited-beam, high-power operation from X-junction coupled phase-locked arrays of AlGaAs/GaAs diode lasers. *Appl. Phys. Lett.*, 53:1366–1368, 1988.

[55] B. Hermansson and D. Yevick. Analysis of Y-junction and coupled laser arrays. *Applied Optics*, 28:66–73, 1989.

[56] D. Botez, L. J. Mawst, G. Peterson, and T. J. Roth. Resonant optical transmission and coupling in phase-locked diode laser arrays of antiguides: The resonant optical waveguide array. *Appl. Phys. Lett.*, 54:2183–2185, 1989.

[57] C. Zmudzinski, D. Botez, and L. J. Mawst. Coherent, one watt operation of large aperture resonant arrays of antiguided diode lasers. *Appl. Phys. Lett.*, 62:2914–2916, 1993.

[58] C. Hasnain, D. F. Welch, D. R. Scifres, J. R. Whinnery, A. Dienes, and R. D. Burnham. Diffraction-limited emission from a diode laser array in an apertured graded-index lens external cavity. *Appl. Phys. Lett.*, 49:614–616, 1986.

[59] G. A. Henderson and D. L. Begley. Injection-locked semiconductor laser array using a graded-index rod: a computational model. *Applied Optics*, 28:4548–4551, 1989.

[60] R. Waarts, D. Mehuys, D. Nam, D. Welch, Streifer W., and D. Scifres. High-power, CW, diffraction-limited, GaAlAs laser diode array in an external Talbot cavity. *Appl. Phys. Lett.*, 58:2586–2588, 1991.

[61] David Mehuys, William Streifer, Robert G Waarts, and David F Welch. Modal analysis of linear Talbot-cavity semiconductor lasers. *Optics Letters*, 16(11):823–825, 1991.

[62] B. Liu, Y. Liu, and Y. Braiman. Coherent beam combining of high power broad-area laser diode array with a closed-V-shape external Talbot cavity. *Opt. Express*, 18:7361–7368, 2010.

[63] C. J Corcoran and K. A Pasch. Modal analysis of a self-Fourier laser. *Journal of Optics A:Pure and Applied Optics*, 7(5):L1–L7, 2005.

[64] C. J. Corcoran and F. Durville. Experimental demonstration of a phase-locked laser array using a self-Fourier cavity. *Appl. Phys. Lett.*, 86:201118, 2005.

[65] L. Goldberg, J. F. Weller, D. Mehuys, D. F. Welch, and D. R. Scifres. 12W broad-area semiconductor amplifier with diffraction-limited optical output. *Electron. Lett.*, 27:927–929, 1991.

[66] J. N. Walpole, E. S. Kintzer, S. R. Chinn, C. A. Wang, and Missaggia L. J. High-power strained-layer InGaAs/AlGaAs tapered traveling wave amplifier. *Appl. Phys. Lett.*, 61:740–742, 1992.

[67] Thomas M Shay, Senior Member, Vincent Benham, Jeffrey T Baker, Anthony D Sanchez, D Pilkington, and Chunte A Lu. Self-Synchronous and Self-Referenced Coherent Beam Combination for Large Optical Arrays. *IEEE Journal of Selected Topics in Quantum Electronics*, 13(3):480–486, 2007.

[68] Eric C Cheung, James G Ho, Gregory D Goodno, Robert R Rice, Josh Rothenberg, Peter Thielen, Mark Weber, and Michael Wickham. Diffractive-optics-based beam combination of a phase-locked fiber laser array. *Optics Letters*, 33(4):354–356, 2008.

[69] Gregory D Goodno, Stuart J Mcnaught, Joshua E Rothenberg, Timothy S Mccomb, Peter A Thielen, Michael G Wickham, and Mark E Weber. Active phase and polarization locking of a 1 . 4 kW fiber amplifier. *Optics Letters*, 35(10):1542–1544, 2010.

[70] Radoslaw Uberna, Andrew Bratcher, Thomas G Alley, Anthony D Sanchez, S Flores, and Benjamin Pulford. Coherent combination of high power fiber amplifiers in a two-dimensional re-imaging waveguide. *Optics Express*, 18(13):13547–13553, 2010.

[71] M Wickham. Coherent Beam Combining of Fiber Amplifiers and Solid-State Lasers Including the Use of Diffractive Optical Elements,. In *in Conference on Lasers and Electro-Optics, OSA Technical Digest (CD) (Optical Society of America, 2010), paper CThG2.*

[72] S. J. Augst, J. Montoya, K. Creedon, J. Kansky, T. Y. Fan, and A. Sanchez-Rubio. Intracavity coherent beam combining of 21 semiconductor gain elements using SPGD. In *Lasers and Electro-Optics, 2012. CLEO '12., Summaries of papers presented at the Conference*, page paper CTu1D.1, 2012.

[73] R. K. Huanga, B. Channa, L. J. Missaggiaa, S. J. Augsta, M. K. Connorsa, G. W. Turnera, A. Sanchez, J. P. Donnellya, J. L. Hostetlerb, C. Miesterb, and F. Dorsch. Coherently combined diode laser arrays and stacks. In *IEEE/OSA CLEO*, page CWF1, 2009.

[74] A. F. Glova. Phase locking of optically coupled lasers. *Quantum Electron.*, 33:283–306, 2003.

[75] T. Z. Wu, W. Z. Chang, A. Galvanauskas, and H. G. Winful. Model for passive coherent beam combining in fiber laser arrays. *Opt. Express*, 17:19509–19518, 2009.

[76] Wei-zung Chang, Tsai-wei Wu, Herbert G. Winful, and Almantas Galvanauskas. Array size scalability of passively coherently phased fiber laser arrays. *Optics Express*, 18(9):9634–9642, 2010.

[77] K. L. Chen and S. Wang. Single-lobe symmetric coupled laser arrays. *Electron. Lett.*, 21:347–349, 1985.

[78] K. Chen and S. Wang. Analysis of symmetric y junction laser arrays with uniform near field distribution. *Electron. Lett.*, 22:644–645, 1986.

[79] *Springer Series in Optical Science: High Power Diode Lasers*. Springer, 2006.

[80] A. Yariv and P. Yeh. *Photonics:Optical Electronics in Modern Communications*. Oxford University Press, 2007.

[81] H. Boudinov, H. H. Tan, and C. Jagadis. Electrical isolation of n-type and p-type inp layers by proton bombardment. *J. Appl. Phys.*, 89, 2001.

[82] S. J. Pearton. Ion implantation for isolation of iii-v semiconductors. *Mater. Sci. Rep.*, 4(6):313–363, 1990.

[83] Y. Zhao and L. Zhu. On-chip coherent combining of angled-grating diode laser toward bar-scale single-mode lasers. *Opt. Express*, 20:6375–6384, 2012.

[84] Lin Zhu. *Photonic Crystal Bragg Lasers : Design , Fabrication , and Characterization*. PhD thesis, Caltech, 2008.

[85] Lin Zhu, Philip Chak, Joyce K S Poon, Guy A Derose, Amnon Yariv, and Axel Scherer. Electrically-pumped, broad-area, single-mode photonic crystal lasers. *Optics Express*, 15(10):961–963, 2007.